Library Declaration and Deposit Agreement

1. **STUDENT DETAILS**

   Richard Paul Ashley

   1360981

2. **THESIS DEPOSIT**

   2.1 I understand that under my registration at the University, I am required to deposit my thesis with the University in BOTH hard copy and in digital format. The digital version should normally be saved as a single pdf file.

   2.2 The hard copy will be housed in the University Library. The digital version will be deposited in the University's Institutional Repository (WRAP). Unless otherwise indicated (see 2.3 below) this will be made openly accessible on the Internet and will be supplied to the British Library to be made available online via its Electronic Theses Online Service (EThOS) service. [At present, theses submitted for a Master's degree by Research (MA, MSc, LLM, MS or MMedSci) are not being deposited in WRAP and not being made available via EthOS. This may change in future.]

   2.3 In exceptional circumstances, the Chair of the Board of Graduate Studies may grant permission for an embargo to be placed on public access to the hard copy thesis for a limited period. It is also possible to apply separately for an embargo on the digital version. (Further information is available in the Guide to Examinations for Higher Degrees by Research.)

   2.4 (a) Hard Copy I hereby deposit a hard copy of my thesis in the University Library to be made publicly available to readers immediately.
   I agree that my thesis may be photocopied.

   (b) Digital Copy I hereby deposit a digital copy of my thesis to be held in WRAP and made available via EThOS.
   My thesis can be made publicly available online.

3. **GRANTING OF NON-EXCLUSIVE RIGHTS**
   Whether I deposit my Work personally or through an assistant or other agent, I agree to the following: Rights granted to the University of Warwick and the British Library and the user of the thesis through this agreement are non-exclusive. I retain all rights in the thesis in its present version or future versions. I agree that the institutional repository administrators and the British Library or their agents may, without changing content, digitise and migrate the thesis to any medium or format for the purpose of future preservation and accessibility.

4. **DECLARATIONS**

   (a) I DECLARE THAT:

   - I am the author and owner of the copyright in the thesis and/or I have the authority of the authors and owners of the copyright in the thesis to make this agreement. Reproduction of any part of this thesis for teaching or in academic or other forms of publication is subject to the normal limitations on the use of copyrighted materials and to the proper and full acknowledgement of its source.
   - The digital version of the thesis I am supplying is the same version as the final, hardbound copy submitted in completion of my degree, once any minor corrections have been completed.
   - I have exercised reasonable care to ensure that the thesis is original, and does not to the best of my knowledge break any UK law or other Intellectual Property Right, or contain any confidential material.
   - I understand that, through the medium of the Internet, files will be available to automated agents, and may be searched and copied by, for example, text mining and plagiarism detection software.

   (b) IF I HAVE AGREED (in Section 2 above) TO MAKE MY THESIS PUBLICLY AVAILABLE DIGITALLY, I ALSO DECLARE THAT:

   - I grant the University of Warwick and the British Library a licence to make available on the Internet the thesis in digitised format through the Institutional Repository and through the British Library via the EThOS service.
   - If my thesis does include any substantial subsidiary material owned by third-party copyright holders, I have sought and obtained permission to include it in any version of my thesis available in digital format and that this permission encompasses the rights that I have granted to the University of Warwick and to the British Library.

5. **LEGAL INFRINGEMENTS**

   I understand that neither the University of Warwick nor the British Library have any obligation to take legal action on behalf of myself, or other rights holders, in the event of infringement of intellectual property rights, breach of contract or of any other right, in the thesis.

Please sign this agreement and return it to the Graduate School Office when you submit your thesis.

Student's signature: ....Date: ....
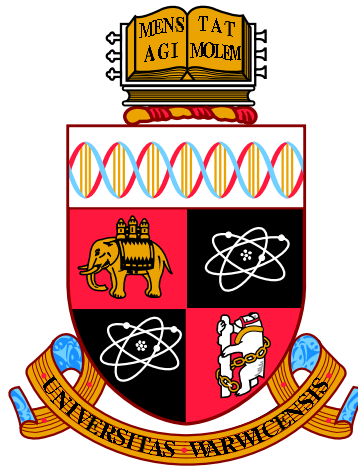
Observations of compact binary systems

by

by

Richard Paul Ashley

Thesis

Submitted to the University of Warwick

for the degree of

Doctor of Philosophy

Department of Physics

February 2020

THE UNIVERSITY OF

WARWICK

Contents

List of Figures

Acknowledgments

Declarations

I submit this thesis to the University of Warwick graduate school for the degree of Doctor of Philosophy. This thesis was written by me and has not been submitted to any other institution. The grammatical style of this thesis follows that usually adopted when writing for refereed journals and is therefore written in the passive voice or the first person plural ('we'). In the majority of cases, this 'we' could be re-written as 'I'.

Parts of the chapter 2 were taken from my Master's thesis, Ashley (2015). This thesis also includes material from published papers written by me, including:

- *"Evidence for bimodal orbital separations of white dwarf-red dwarf binary stars"*, Ashley et al. (2019), MNRAS, 484, 5362A. Material from this paper is used in Chapter 3.

- *"V1460 Her: A fast spinning white dwarf accreting from an evolved donor star"*, Submitted to MNRAS and currently in review.

Other parts of this research are also being prepared for publication in peer-reviewed journals. Chapter 5 on V808 Aur is being prepared for publication with the key result being the masses of the components and apparent period changes. Chapter 6 on CRTS2152 will be a paper to announce a new polar with early estimates of some of the system parameters.

Abstract

In this thesis I study compact binary systems containing white dwarfs, looking at both detached systems and those that are accreting. These systems are representative of a diverse set of white dwarf binaries in the Galaxy, from which thermonuclear supernovae and other varieties of exotic stellar object emerge. Following a description of the observational techniques and data sources used, I begin with a study of a sample of white dwarfs that show evidence for excess infrared emission in their spectral energy distributions. The targets formed a subset of a larger sample after removal of systems resolved from the *Hubble Space Telescope (HST)*. The period distribution ranges from 0.141 to $9.16\,\mathrm{d}$ and peaks near $0.6\,\mathrm{d}$. The original sample therefore contains two sets of binaries, wide orbits ($\approx 100 - 1000\,\mathrm{au}$) and close orbits ($\lesssim 1 - 10\,\mathrm{au}$), with no systems found in the $\approx 10 - 100\,\mathrm{au}$ range. This observational evidence confirms the bimodal distribution predicted by population models and is also similar to results obtained in previous studies. I find no binary periods in the months to years range, supporting the post common envelope evolution scenario. The work on detached systems revealed the remarkable utility of modern wide-field photometric surveys. These are revealing rare and unusual types of white dwarf binary systems previously missed through faintness and inconspicuous photometric behaviour. I look at examples of these in the following three chapters. Chapter 4 presents a study of V1460 Her, a star only identified as an accreting binary following a rare, low amplitude outburst. V1460 Her is revealed as a remarkable system, which hosts a donor star far from thermal equilibrium, the remnant of a phase of rapid mass loss. In addition, its white dwarf shows a strong coherent signal on a period of 39 seconds in *HST* ultraviolet data. It shares these two aspects with the hitherto unique system AE Aqr which also has a rapidly spinning white dwarf, but, unlike V1460 Her, is propelling accreting matter out of the system altogether. Chapters 5 and 6 present new observations on magnetic CVs. V808 Aur is a polar is undergoing changes in its orbital period as is shown through ten years of photometric observations. I also derive masses for both components in the system and determine the spectral type of the donor. CRTS J215256.1+191658 is a newly discovered $3.9\,\mathrm{hr}$ period polar. I present high speed photometry showing the eclipse in both a high and low state and Doppler maps of the emission features revealing the flow of the accretion stream through the system.

Abbreviations

ADU	Analogue Digital Units
AGB	Asymptotic Giant Branch
ASAS-SN	All-Sky Automated Search for SuperNovae
BPS	Binary Population Synthesis
CCD	Charge Coupled Device
CRTS	Catalina Real-time Transient Survey
CSS	Catalina Sky Survey
CV	Cataclysmic Variable
EMCCD	Electron Multiplying Charge Coupled Device
ESO	European Southern Observatory
FWHM	Full Width at Half Maximum
INT	Isaac Newton Telescope
IR	Infrared
LSST	Large Synoptic Survey Telescope
NTT	New Technology Telescope
PCEB	Post Common Envelope Binary

PTF	Palomar Transient Facility
PSF	Point Spread Function
RGB	Red Giant Branch
RV	Radial Velocity
S/N	Signal-to-Noise Ratio
SDSS	Sloan Digital Sky Survey
SN Ia	Type Ia Supernova
TNT	Thai National Telescope
UV	Ultraviolet
WHT	William Herschel Telescope
ZTF	Zwicky Transient Factory

Chapter 1

Introduction

"If you wait long enough, every star is variable."
   — Attributed to several astronomers

1.1 Variability in stars

In medieval Europe, natural philosophers believed that the heavens were eternal
and immutable. Apart from the wandering stars (or planets) and the occasional
comet or meteor, the stars themselves were believed to be unchanging. In China,
records dating back to 1500 BCE, catalogue new objects in the sky which can be
accounted for as comets, meteors, novae and supernovae (Stephenson and Clark,
1976). Ancient Egyptian astronomers were aware of the variability of Algol and had
documented its 2.85 day period (Jetsu et al., 2013). The cause of Algol's variability
was only understood much later to be due to the fact that it is an unresolved system
of two stars with the eclipse of one object by the other causing a drop in overall
brightness (Goodricke, 1783), marking the start of the study of eclipsing binary
stars.

   In 1855, J.R. Hind, who was searching for minor planets, noticed a new 9th
magnitude star, 'shining with a very blue planetary light'. Returning to the field
nine days later he confirmed it was still there. He announced that this was different
in nature to Algol, in that its bright phase lasted for a relatively short portion of
its overall period, noting that he had been examining this area of the sky for five
years (Hind, 1856). This new variable was designated U Geminorum. U Gem faded,

but a few months later was found to be back at maximum light (Warner, 1986). Its magnitude at minimum light was found to be $V \simeq 13 - 14$. The development of a model that explained the nature of this new kind of variable came about incrementally as more observations and newer techniques provided evidence of additional behaviours of variability. Linnell (1949, 1950)'s observations of UX UMa showed evidence of short-term ($\lesssim 1\,\mathrm{minute}$) 0.01-0.2 mag variability or 'flickering'. It was Walker and Herbig (1954) who made the first attempt to explain the structure of a binary system that might account for the observational evidence, being 'a mass of hot material situated well above the surface of the primary'. Through spectroscopic observations, Kraft (1962) demonstrated that this category of variables displayed signs of binary motion. The current model for what we now call a cataclysmic variable (CV) was proposed by Warner and Nather (1971) and independently by Smak (1971). Before we return to the topic of CVs, we will begin with an introduction to stellar formation and evolution and then introduce binary formation and evolution.

1.2 Star formation and evolution

Stars start their lives as gas clouds containing primarily hydrogen, helium and some traces of heavier elements (metals). These gas clouds can start to condense if they are perturbed by collisions with other clouds or by shock waves resulting from nearby astrophysical events, such as supernovae. If the cloud has sufficient mass such that the internal gas pressure cannot balance its own gravity, it passes the so-called Jeans instability criterion (Jeans, 1902) and continues to collapse. During this collapse, the gas heats up in response to adiabatic work done by the compression process. When the core of the cloud becomes opaque to its own thermal radiation, a protostar is born. If its mass is below the lower stellar mass-limit of about $0.08\,\mathrm{M_\odot}$, the core will never be able to reach the critical density and temperature that allow fusion of hydrogen into helium. These low-mass objects will never become stars and simply cool on a timescale that is longer than the age of the universe. Such objects, known as brown dwarfs, have been observed, both directly, in the Pleiades open cluster (Rebolo et al., 1995), and through their influence on brighter companions, where they are seen orbiting white dwarfs (Maxted et al., 2006; Parsons et al., 2017). For larger mass cores, hydrogen fusion commences and this source of energy eventually dominates over that generated by the initial gravitational collapse and we can now say that the star is officially born. The star that emerges at this stage is a so-called zero-age main sequence star (ZAMS). The mass of this star depends on several factors and the distribution of ZAMS masses is described by the initial

mass function (IMF). The IMF is a power law which dictates that low-mass stars far outnumber their high-mass counterparts (Salpeter, 1955). The mass of an individual star, which is the main parameter determining its subsequent evolution, depends on the conditions in the cloud from which it forms, such as the mass of the cloud fragments and the metallicity of the cloud. Fig. 1.1 shows a Hertzsprung-Russell diagram with a distribution of main sequence stars in our local region of the Milky Way.

Depending on the mass of the star, its life on the main sequence will be somewhere from tens of millions of years for stars with masses greater than $8\,\mathrm{M_\odot}$ to hundreds of billions of years for very low mass, $< 0.4\,\mathrm{M_\odot}$, stars. In low and intermediate mass stars $(0.6\,\mathrm{M_\odot} \lesssim M \lesssim 1.5\,\mathrm{M_\odot})$, which have a radiative core, the hydrogen burning is concentrated towards the center and takes place through the proton-proton (or p-p) chain. As hydrogen is depleted here, the burning zone moves outward and takes place in an expanding, narrowing shell around a growing, central inert helium core. The density of this shell decreases as it moves outwards and its temperature rises, allowing the burning to take place more rapidly. The overall density and temperature in the non-burning outer envelope decreases and the star expands to roughly 100 times its former size. At this point the star moves onto the red giant branch (RGB). The helium core contracts and its temperature rises. When its temperature reaches approximately $10^8\,\mathrm{K}$, helium fusion via the triple-α process begins. In low mass stars, this is a particularly rapid transition also known as the 'helium flash'. With the expanded and heated core, the outer envelope contracts and the star moves back towards the main sequence on the HR diagram. Not quite reaching the main sequence, stars at this stage form a feature referred to as the 'red clump'. The position and presence of the red clump feature is strongly dependent on metallicity of the star and does not appear in older populations. At this stage, the star is now burning helium in the core and hydrogen in a shell around the core. As the helium is converted to carbon and oxygen the centre is once again depleted of fuel and the helium burning region also becomes a shell around an inert core. The core contracts, the outer envelope expands and the star once again evolves up the giant branch, although this time it is called the asymptotic giant branch (AGB). Stars with higher masses $(M \gtrsim 1.5\,\mathrm{M_\odot})$ have a slightly different path from the main sequence to the giant branch. They have convective (as opposed to radiative) cores and burn hydrogen via the CNO cycle rather than the p-p chain. The CNO cycle is a catalytic reaction that shuffles the existing abundances of CNO, leaving N as the dominant by-product (Arnould et al., 1999). The convection of the core mixes in fresh hydrogen and fuel exhaustion is delayed. When the fuel is finally depleted, all
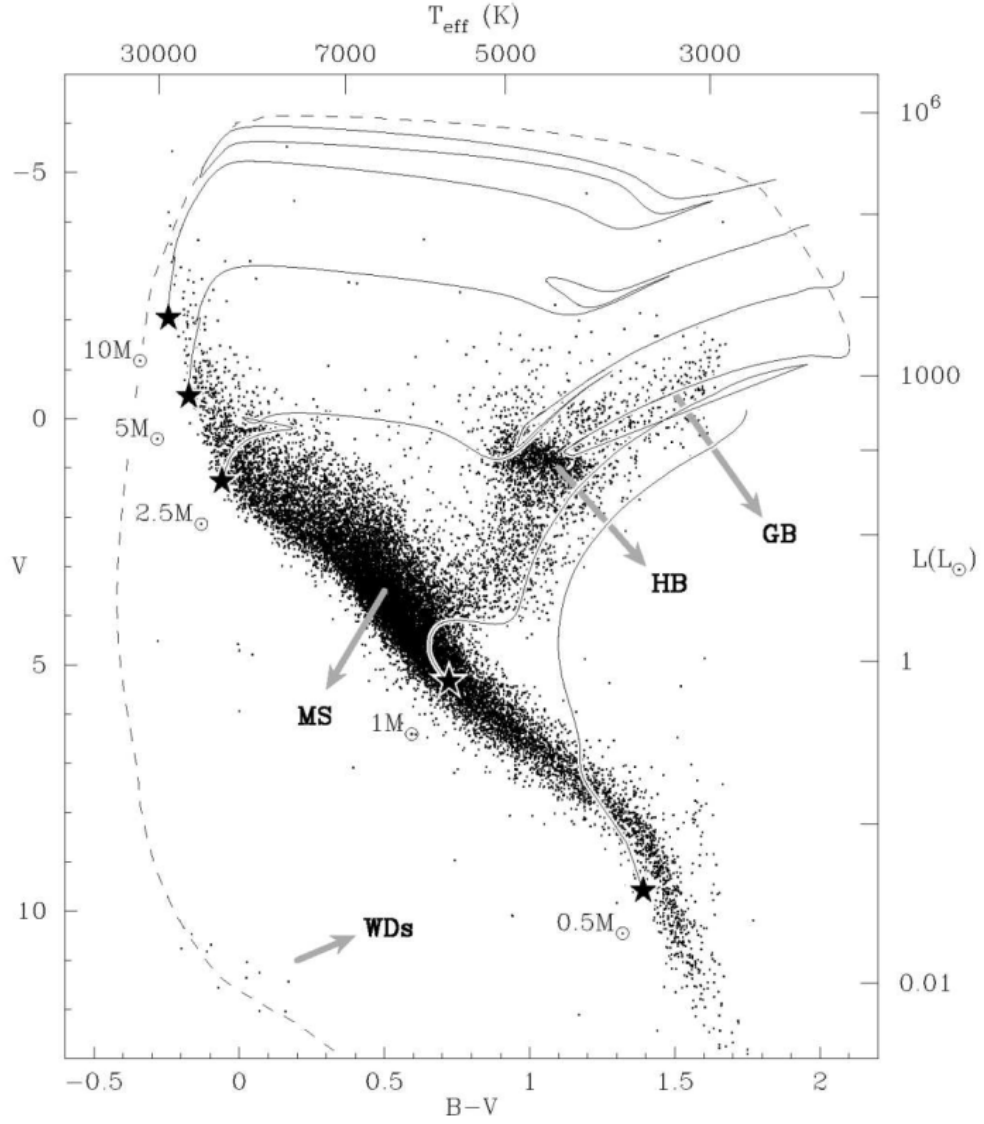
Figure 1.1: Hertzsprung-Russell diagram from Hipparcos data showing the colour (temperature) and absolute luminosity of 20546 nearby stars. This Fig. is taken from Bours (2015). Points indicated by stars show the start of the evolutionary track of stars of 0.5, 1.0, 2.5, 5 and 10 $M_\odot$. GB indicates the giant granch, HB the horizontal branch, MS the main sequence and WDs shows the location of the white dwarfs in the HR diagram.

burning is paused and the core contracts quickly until it reaches a situation where the hydrogen just outside the core is hot enough to resume burning in a shell. As the core contracts, the outer envelope expands and the star moves to the giant branch. Since this process is quick, the transition to the giant branch is rapid and this results in a lack of stars in an area of the HR diagram known as the 'Hertzsprung gap'. Since the reaction rate of the triple-α process is very sensitive to temperature, fluctuations in stellar temperature and radius lead to surges in luminosity known as thermal pulses. These pulses also have the effect of dredging up internal material and bringing it to the surface, changing the external chemical composition of the star. A portion of the star's atmosphere can be ejected during these pulses.

Eventually the outer atmosphere is discarded, pressure drops and fusion halts. The core remains, as a small, hot, blue object surrounded by a nebula of the ejected material. As the core cools and contracts, it becomes a white dwarf. Very high mass stars follow a different evolutionary path and it is only those with a ZAMS mass of $0.8\,\mathrm{M}_\odot \lesssim M \lesssim 5-8\,\mathrm{M}_\odot$ that will result in white dwarfs.

Since white dwarfs are electron degenerate, their size follows an inverse relationship to their mass, in fact, for the non-relativistic limit ($M \lesssim 1.0\,\mathrm{M}_\odot$), $R \propto M^{-1/3}$. The observed mass distribution of white dwarfs is narrowly bound with the mode being at $0.6\,\mathrm{M}_\odot$ and a narrow dispersion around that value (see Fig. 1.2). Liebert et al. (2005) find for 285 white dwarfs from the Palomar-Green survey, the mean mass is $\overline{M} = 0.603 \pm 0.134\,\mathrm{M}_\odot$. This tight distribution of masses is confirmed in broader surveys like the Sloan Digital Sky Survey (SDSS) (Tremblay et al., 2016; Kleinman et al., 2013). However, there is an ultimate mass limit for a white dwarf. In the interior, the electrons form a degenerate gas and, due to Pauli's exclusion principle, they are forced into high momentum states. This provides the internal pressure to keep the object from collapsing. As was famously shown by Chandrasekhar (1939), when the electron energy approaches the relativistic limit, an overall upper bound for the maximum mass of the white dwarf of $M = 1.4\,\mathrm{M}_\odot$ is reached. Beyond that mass, the Fermi energy of the electrons can exceed the mass difference between the nuclei, allowing the capture of an electron into a nucleus transforming a proton into a neutron (so called "inverse β decay").

1.3   Binary stars

1.3.1   Binary formation

It is estimated that the field star population in the solar neighbourhood consists of 50 per cent binary systems (Eggleton and Tokovinin, 2008). It has also been
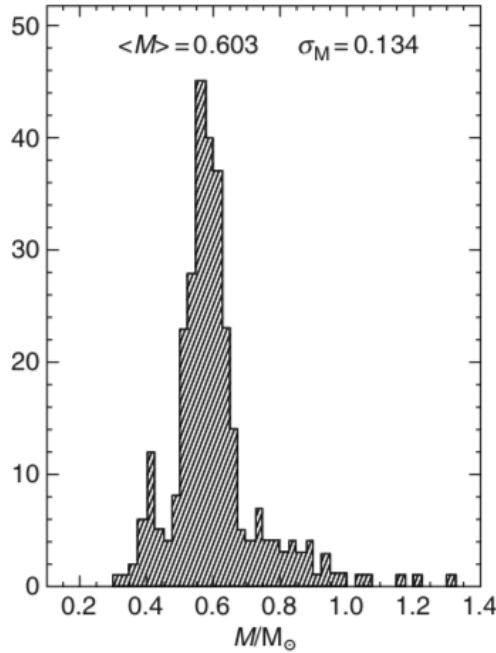
Figure 1.2: White dwarf mass distribution from 298 WDs in the Palomar-Green survey. This is Fig. 12 of Liebert et al. (2005).

shown by Raghavan et al. (2010) that this is dependent on spectral type, with early types much more likely to be found as part of multiple systems, the fraction being ≈ 70 per cent for O and B types, coming down to ≈ 50 per cent for stars of spectral type G and finally ≈ 20 per cent for the very late L and T types. The reasons for the predominance of multiple systems over solitary stars is something that is still an active area of research, but it is generally believed to be the end result of conservation of angular momentum in the condensing gas cloud. Although a potential explanation is also provided by the capture of one star by another, the expected rarity of an event like this given the space density of stars (notwithstanding the fact that most stars form in clusters) and that conservation of energy requires a third object to interact with the system and be ejected means that this scenario is less favoured as a binary formation scenario (Oswalt and Barstow, 2013). More likely are scenarios that have the stars forming together. As the gas cloud condenses, angular momentum is conserved and therefore, if the cloud had any significant initial rotation, it would lead to more rapid rotation as its overall size decreases. This rotation could result in cloud fragmentation and the formation of two separate, but gravitationally bound objects, this is referred to as 'prompt fragmentation'. Another possibility is fragmentation of the accretion disc of the first protostar (Bonnell and

Bate, 1994), which results in two (or more) stars forming in close proximity, also known as 'disc fragmentation'. Simulations of stars forming in a cluster environment performed by Bate et al. (2003) suggest that binary formation is a natural channel of star formation. Since we generally accept that both components in a binary formed at the same time, we can also accept that they have the same overall age. Duquennoy and Mayor (1991) found that the field population of solar type stars have a unimodal period distribution that can be fitted remarkably well by a log-normal function with an average period of approximately 180 years. Using a volume limited sample of 25 pc (Raghavan et al., 2010) also demonstrated a strongly Gaussian unimodal distribution, with a peak at 290 years. Duquennoy and Mayor (1991) noted that the orbits are circular for binaries with periods less than 11 d and those with longer periods have a broad range of eccentricities. It is thought the tidal interactions in close binaries circularise their orbits.

1.3.2 Binary evolution

Apart from contact binaries, the components of most binary systems live out their main sequence lives without interaction. When the more massive component, the primary star, leaves the main sequence, it will evolve up the giant branch. If the separation of the components in the binary is sufficiently small, the primary star's increase in size will be such that it fills the Roche lobe. We can define the form of the Roche potential by considering the centrifugal and gravitational forces on a test particle in the position (x, y, z) in the co-rotating reference frame of the binary orbit as

$$\Phi = -\frac{GM_1}{\sqrt{x^2 + y^2 + z^2}} - \frac{GM_2}{\sqrt{(x-a)^2 + y^2 + z^2}} - \frac{\omega^2}{2} \left[\left(x - \frac{aM_2}{M_1 + M_2} \right)^2 + y^2 \right],$$
(1.1)

where M_1 and M_2 are the masses of the two component stars in the system, a is the separation of the two (or the semi-major axis) and ω is the angular velocity of the binary, $\omega = \frac{2\pi}{P_{\mathrm{orb}}}$ with P_{orb} the binary orbital period.

The Roche lobe, shown schematically in Fig. 1.3, is the equipotential surface at which a test particle will be unbound to the star. The equivalent radius (that is the radius for a sphere of equivalent volume) R_{L} of the Roche lobe of the lighter component in the binary is given by Eggleton (1983)'s formula which is based on an initial approximation given by Paczyński (1971),

$$\frac{R_{\mathrm{L}}}{a} = \frac{0.49q^{2/3}}{0.6q^{2/3} + \ln\left(1 + q^{1/3}\right)}$$
(1.2)
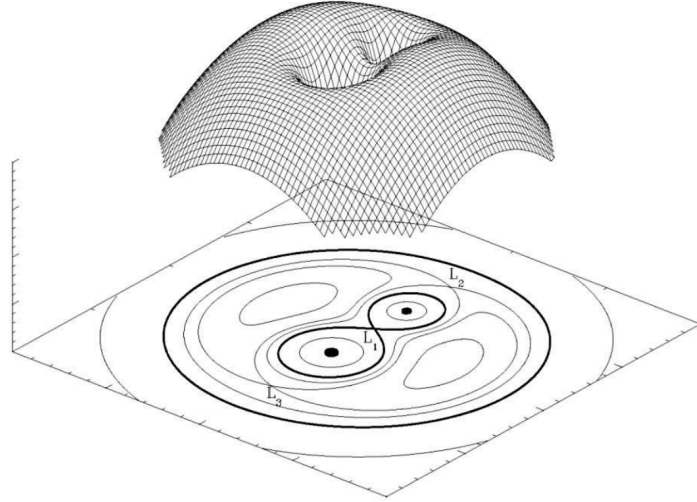
Figure 1.3: Representation of the Roche potential in a binary with a mass ratio, q, of 0.5. The thick solid lines show the Roche lobes of both the primary and secondary. The outer circle is the equipotential line at which a test particle would be unbound from the binary. L_1, L_2 and L_3 are the Lagrangian points at which the gravitational and centrifugal forces of the stars cancel each other out. This figure courtesy of Marc van der Sluys.

where q is the mass ratio of the two component stars, $q = M_2/M_1$.

1.3.3 The common envelope

As the more massive star exceeds its Roche lobe unstable mass transfer is triggered and its atmosphere will extend sufficiently far to engulf both stars and thereby form a *common envelope*. During the common envelope phase, drag forces will drain angular momentum from both bodies and bring them closer together. The exact processes that occur during this phase are poorly understood, and difficult to model computationally, but it is thought that the inspiral occurs quickly (< 100 years, Ivanova et al., 2013). The angular momentum and energy lost is transferred to the gas envelope and helps to expel it from the system. The fraction of the orbital energy that goes into discarding the common envelope is usually given as α_{CE} where $E_{bind} = \alpha_{CE}\Delta E_{orb}$. E_{bind} is the gravitational binding energy of the envelope and ΔE_{orb} is the change in orbital energy of the two stars (Davis et al., 2010; Willems and Kolb, 2004; Zorotovic et al., 2014). Recent observational and theoretical studies indicate a value for the efficiency of transfer of the orbital energy $\alpha_{CE} = 0.2 - 0.3$ (Zorotovic et al., 2010). Eventually, the primary will evolve away from its giant phase, leaving behind a white dwarf. The end result of this process
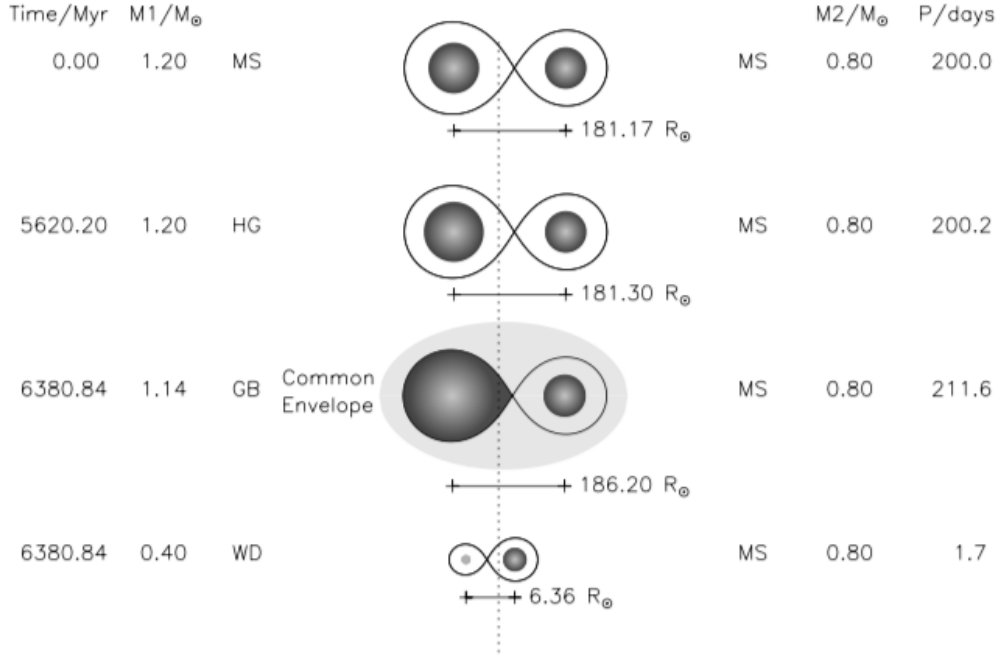
Figure 1.4: An example scenario of the evolution of a binary pair taken from Fig. 6 of Willems and Kolb (2004). HG refers to the Hertzsprung gap, MS means the main sequence and GB means the giant branch.

is a pair consisting of a white dwarf and a main sequence star (WD+MS) with a relatively small separation, known as a post common-envelope binary (PCEB). An example scenario taken from Willems and Kolb (2004) is shown in Fig. 1.4.

However, not all binary systems will follow this path. If the initial separation of the two components is large enough then the red giant star does not fill its Roche lobe and no common envelope is formed. This distance is about $2 - 3 \, \mathrm{au}$ for systems with M-dwarf secondaries (Willems and Kolb, 2004). In fact, when the outer atmosphere of the primary is dissipated, this mass loss will have the effect of widening the orbit. These two distinct evolutionary paths lead to two separate populations of WD+MS binaries, those that have experienced a common envelope and therefore have periods of hours to days, and those that have not experienced a common envelope and have periods of several years or more.

A commonly used method to investigate the outcome of the common envelope phase is binary population synthesis (BPS). This is a theoretical process that involves simulating the evolution of a binary by modeling the development of both components using stellar evolution models and including additional simulations of mass transfer and orbital dynamics (Willems and Kolb, 2004). BPS studies
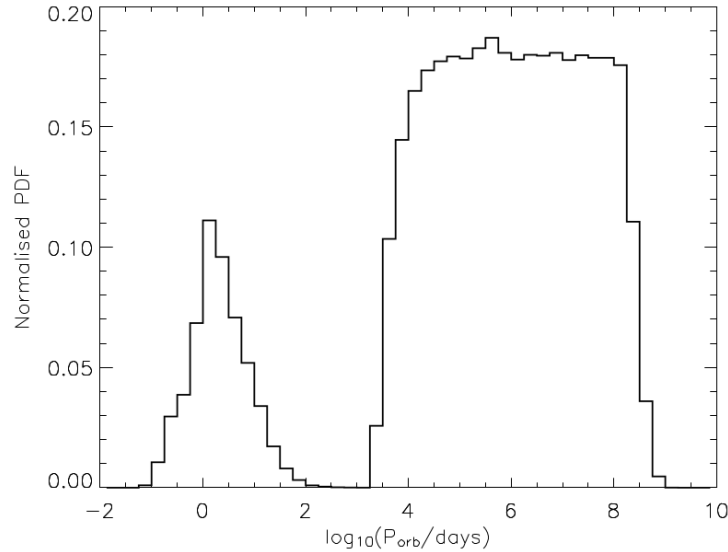
Figure 1.5: The predicted period distribution of white dwarf - main sequence binaries based on a BPS of these systems. After evolution of one of the components, two distinct populations are formed. Compact binaries with short periods and small separation, and long period binaries. This figure is taken from Fig. 9 of Willems and Kolb (2004).

have been performed for Type Ia supernova progenitors (Han and Podsiadlowski, 2004), short γ-ray bursts (Belczynski et al., 2006), and WD+MS systems (Willems and Kolb, 2004; Davis et al., 2010). These studies predict that WD+MS systems will have orbital periods that follow a bimodal distribution, with the short period PCEBs peaking at about $1-2$ d ($\log P_{\mathrm{orb}}$ (d) ≈ 0.2), and continuously detached binaries with periods of years or more, see Fig. 1.5. Specifically, models of orbital expansion due to adiabatic mass loss, combined with models of frictional inspiral within a common envelope, predict a gap between diminished ($a \lesssim 0.1$ au, $P \approx$ hours to days) and augmented ($a \gtrsim 5$ au, $P \sim 10$ to 1000 yr) orbits for low-mass, un-evolved companions to white dwarfs, (Farihi et al., 2006).

An additional energy source that might be a factor in dispersing the common envelope is the recombination energy released when the ionised hydrogen gas in the common envelope returns to the non-ionised state, i.e. electrons recombine with the ions. This energy would contribute to the dispersal of the common envelope and less energy would be needed from the angular momentum loss. Zorotovic et al. (2014) show that increasing the contribution that recombination energy plays in the dispersal of the envelope would lead to large numbers of longer period PCEBs overall and a tail in the period distribution going out to about 1000 days. At the

moment no PCEB systems are known to have periods of this length. The longest known PCEB period is that of IK Peg at 21.72 days (Landsman, 1993). In chapter 3 we perform an analysis of post-common envelope white dwarf and M-dwarf binaries in order to verify the distribution of orbital periods of these systems.

1.4 Cataclysmic Variables

1.4.1 Accretion

In compact binaries like those described above, with a primary component evolved into a white dwarf and the secondary still a main sequence star, loss of angular momentum can lead to the components drawing closer together. This contraction of the orbit leads to a shrinkage of the overall Roche geometry (Fig. 1.3) and eventually the secondary will fill its own Roche lobe. At this point, its atmosphere spills over the Lagrangian point at L_1 and starts to fall towards the white dwarf. Since this matter has its own angular momentum, it cannot fall directly toward the primary, but follows an arc inward. As more matter falls into this location it starts to collide with itself and orbit the white dwarf as shown in the schematic Fig. 1.6. Eventually, it forms a disc around the white dwarf where it accumulates and spreads out. The disc can be thought of as a series of concentric rings, each at their respective Keplerian velocity. Viscosity in the disc is responsible for angular momentum transport and accretion onto the white dwarf. As alluded to in our opening paragraphs, a compact binary with active accretion is known as a cataclysmic variable (CV).

1.4.2 Disc outbursts

Since the stream that feeds the disc lies predominantly in the orbital plane and the inflowing gas is not thought to drive material out of the plane, the disc can be thought of as a two-dimensional object with a scale height much smaller than the disc extent in the radial direction. The viscous shear between the adjacent annuli causes an overall drift of material inwards towards the white dwarf, although at the outer edge, conservation of angular momentum will mean that some material must drift outwards. At a certain radius from the primary star, tidal effects take over and angular momentum is transferred to the secondary. In a steady state disc, the inflow of material from the donor matches the outflow and the disc is stable. Now we consider the behaviour of a disc that is largely composed of hydrogen. Below a few thousand Kelvin, this gas is in a neutral state. The accumulation of matter will increase the temperature in the disc, which will rise steadily until the hydrogen starts
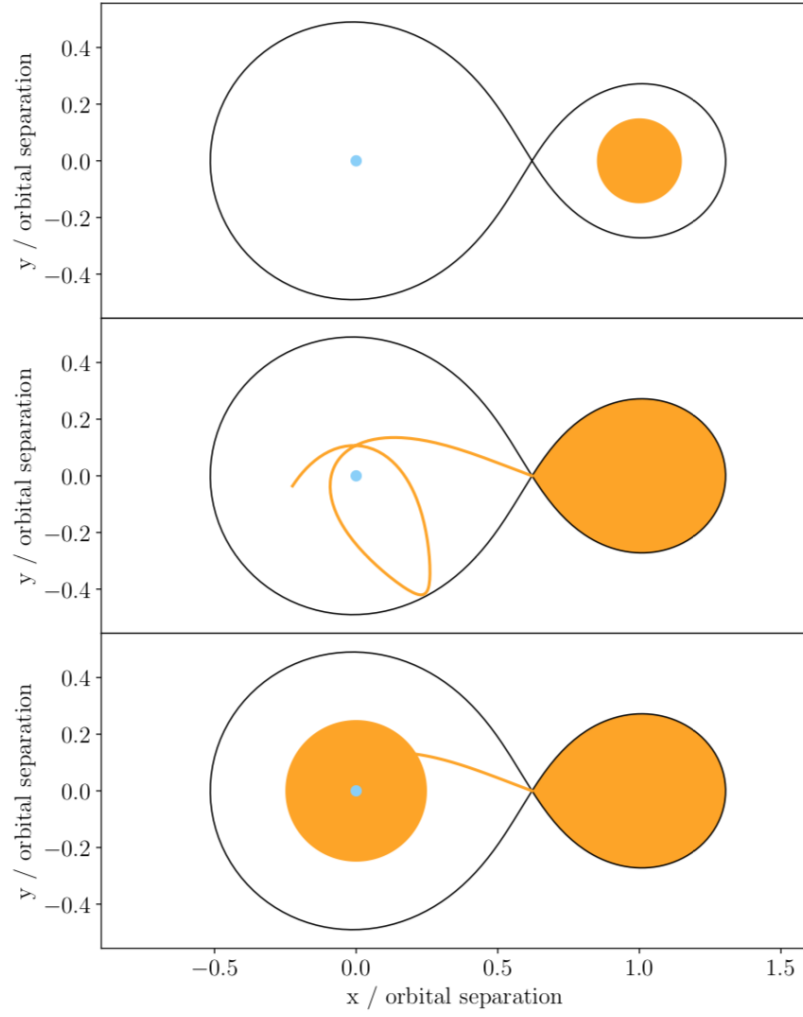
Figure 1.6: Schematic of the formation of an accretion disc in a compact binary. In the upper panel the stars begin as non-interacting bodies. The middle panel shows the onset of accretion as the secondary reaches its Roche lobe. In the lower panel, the accreted material interacts with itself to form the disc. This figure is taken from Fig. 1.2 of Green (2019).

to ionise. Partly ionised regions of the disk will be opaque to radiation and, locally, temperatures will rise rapidly, causing a wave of ionisation to spread over the disc until it is completely ionised. At this point the disc is in a hot viscous state. During this stage, material will be drained from the disc and the ionised state will not be sustained indefinitely. This cyclical change in the disc's state is therefore driven by the transitions between convective and radiative modes of energy transport within the disc (Meyer and Meyer-Hofmeister, 1981). The observed large increase in overall disc luminosity is known as an 'outburst' or 'dwarf nova' (Cannizzo et al., 1982) and was the cause of the surge in brightness that led to the original discovery of U Gem. This is a very simple description of a complicated process and the frequency of disc outbursts depends on many factors, including the size of the orbit and the mass accretion rate. Typical dwarf novae will show outbursts every few months or so, but, within the CV family there is a wide range of outburst behaviour.

1.4.3 Loss of angular momentum

As the donor loses mass, its radius will decrease and it should therefore shrink to a size smaller than the Roche lobe and detach, halting the accretion process. In addition, transfer of mass from the donor to the accretor causes the orbital separation to increase, if the donor is less massive than the accretor as is usually the case. In order for accretion to continue for extended periods there needs to be overall angular momentum loss from the system. This can occur in two ways, namely *magnetic braking* and *gravitational radiation*. In magnetic braking, angular momentum is carried away from the orbit through the stellar wind flowing from the secondary. This flow is magnetically coupled to the secondary and thus, as it flows out beyond the system, it carries angular momentum with it. Since the secondary is tidally locked to the orbital motion, this angular momentum drain is effectively taken from the binary as a whole. For longer period CVs with $P_{\mathrm{orb}} > 4\,\mathrm{hrs}$ this is the main source of angular momentum loss. The second mechanism, gravitational radiation, is a consequence of Einstein's general theory of relativity (Einstein, 1916) and was first suggested as a mechanism for CVs by Kraft et al. (1962) for WZ Sge and was shown to be a driver of CV evolution by Faulkner (1971). Gravitational waves are emitted by all rotating, asymmetric bodies or systems. The gravitational wave observatory, LIGO, made the first direct measurement of these waves a century after Einstein's prediction (Abbott et al., 2016). In binaries, since the rate of angular momentum loss depends on the separation to the inverse fourth power, this process is less important at longer orbital periods but is dominant for shorter periods.

1.4.4 The Period Gap

The general path of CV evolution is from longer periods to shorter ones through the angular momentum loss mechanisms just described. At the longer orbital periods, magnetic braking is the dominant mechanism and if the removal of mass from the donor occurs at a rate that is shorter than the thermal timescale of the donor, $\tau_{\text{th}} = \frac{GM^2}{RL}$, the donor will become over sized for its mass. If mass loss is stopped, then the star will be able to return the equilibrium by shrinking, at which point it will detach from its Roche lobe. Mass transfer might therefore be stopped by a large reduction in the braking process. An explanation that accounts for the interruption in magnetic braking is that, at a mass that is appropriate for the donor in a $\simeq 3\,\text{hr}$ binary, the convective portion of the interior of the donor penetrates throughout the star, preventing a magnetic dynamo in the core (Rappaport et al., 1983). Models of donor star evolution in CVs (Knigge et al., 2011) show that, for non-magnetic CVs at least, the mass transfer rate at this point is about $10^{-9} \text{M}_\odot \, \text{yr}^{-1}$. Since the donor is now detached and there is no accretion to drive the overall luminosity of the system, it becomes effectively invisible to us. At a period of about two hours the secondary fills its Roche lobe again and accretion resumes now at a reduced mass rate of around $10^{-10} \text{M}_\odot \, \text{yr}^{-1}$. From the start of the period gap it is gravitational radiation that becomes the dominant source of braking and occurs on a longer timescale than magnetic braking. Observational evidence for this is seen in paucity of CVs seen with a period between two and three hours as is shown in the uppermost panel of Fig. 1.8. It should be noted, however, that the rate of angular momentum loss for some CVs in this short period regime is higher than can be accounted for by gravitational radiation alone (Knigge et al., 2011). Therefore, it is suspected that magnetic braking is not completely ineffective below periods of $3\,\text{hours}$.

1.5 Magnetic White Dwarfs

Around 10 per cent of white dwarfs in the field show magnetic fields in the 1-100 MG range, yet these magnetic WDs have a significantly higher mean mass of $0.9\,\text{M}_\odot$, compared to $0.6\,\text{M}_\odot$ for non-magnetic WDs (Liebert, 1988), despite the fact that there is not expected to be a dependence of Ohmic decay time on the white dwarf mass (Ferrario et al., 2015). This decay is long, on the order of 10^{10} years, and this suggests that they inherit their fields from their main sequence ancestors. If the progenitor's original field is scaled up as the radius decreases, the main sequence star would need to have had a field in the 0.1–10 kG range (Oswalt and Barstow, 2013). While Ap and Bp stars can account for some of this fraction, there would
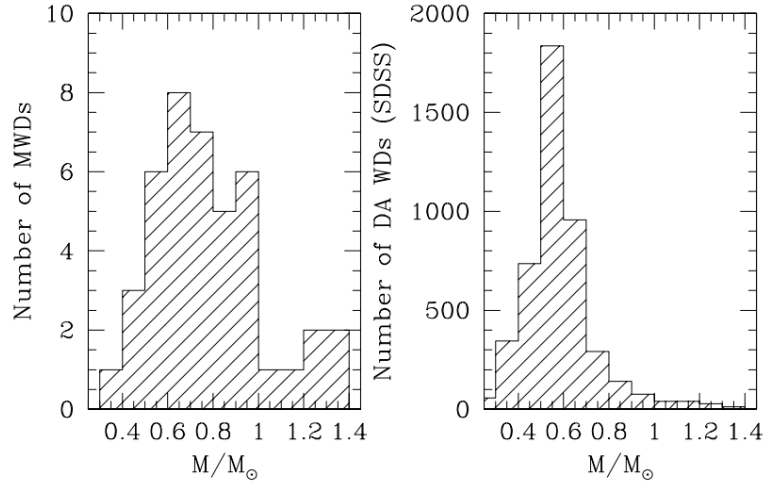
Figure 1.7: The distribution of measured masses for magnetic WDs compared to that of non-magnetic DA white dwarfs. The figure is taken from Ferrario et al. (2015) with data derived from Ferrario and Wickramasinghe (2010) and Kepler et al. (2007).

still need to be more main sequence stars with fields in the stated range that have not been detected so far (Kawka et al., 2007). Another explanation for strong fields in white dwarfs is that they result from a dynamo effect that occurs during the common envelope phase (Tout et al., 2008). The proposition suggests that differential rotation and convection in the envelope creates strong magnetic fields and these are then frozen into the degenerate core. The closer the two bodies get during the common envelope, the stronger the field becomes. Objects that actually merge during this phase become the isolated strongly magnetic WDs and those that do not merge become the magnetic CVs. This explanation accounts for the fact that we find no magnetic white dwarfs in wide binaries ($a \gtrsim 5\,\mathrm{au}$), since they will have skipped the common envelope. It also accounts for the fact that isolated magnetic WDs are statistically more massive than non-magnetic WDs. However, it does not explain the lack of strong magnetic white dwarfs in PCEBs. Belloni and Schreiber (2020) show that this model predicts weaker magnetic fields than observed in the field. More revision of this model is needed if it is to fully explain the origin of magnetic fields in white dwarfs.

1.5.1 Polars

A strong magnetic field in a CV will disrupt the accretion disc. For field strengths in the order of tens of MG, the accretion stream will not form a disc at all, but will, at some point, couple to the magnetic field lines and follow a direct path to the magnetic pole (or poles) of the primary. As the accreted material leaves the L_1 point, it follows the expected free fall path, the so-called 'ballistic stream'. During this phase, the material is largely unaffected by the magnetic field originating in the primary. At some point, as the proximity to the primary increases, the magnetic pressure acting on the stream equals the ram pressure exerted by the infalling stream itself. This is where the stream will divert its course and begin to follow the field lines towards the surface of the white dwarf and become the 'magnetic stream'. Exactly where this occurs depends on the field strength and the density of the accreting material. At this transition point the material decelerates suddenly and most of this kinetic energy is converted into thermal energy. Now following the white dwarf's field lines, it resumes its free fall, but on the path toward the magnetic pole. The material is ionised due to the X-ray radiation emitted by the accretion spot and as it follows the field lines, it spirals in the magnetic field, generating cyclotron radiation. The optical light from the accretion stream is therefore polarised and the mode of polarisation (circular or linear) varies depending on the phase of the orbit and our line of sight into the accretion stream. This strongly polarised modulation is the origin of the name, 'polar'. A review of polars is provided by Cropper (1990).

Intermediate polars (IPs) are similar objects, but differ in that the field strength falls short of completely disrupting the accretion disc. In these systems, a disc forms, but this disc has an inner radius terminated at the point where the accretion follows the field lines. As can be seen in Fig. 1.8, IPs tend to have longer periods than polars and it has been suggested (Cumming, 2002) that there is an evolutionary link between these two objects. At longer periods, the accretion rate is higher, $\dot{M_2} \gtrsim 10^{-9}\,\mathrm{M_\odot\,yr^{-1}}$, exceeding the Ohmic timescale of the outer regions of the white dwarf and effectively burying the magnetic field. As the object evolves to shorter periods and reduced mass transfer rates, the underlying magnetic field re-emerges and the IP becomes a polar.

Since polars are highly magnetic, the field lines of the primary are locked in phase with the donor and hence the white dwarf rotation is synchronous. In fact, the same is true for the secondary, which is usually tidally locked to the orbital period even in non-magnetic CVs. In the case of polars though, this means that the magnetic field lines of both components are mostly connected and field lines radiating out of the orbit are rare. In this situation, magnetic braking is much

reduced and the primary source of angular momentum loss is gravitational radiation (Belloni et al., 2020). This means that, in polars, the deviation of the secondary from thermal equilibrium is negligible as angular momentum loss is much lower at the longer periods. It also means that polars as a population are less likely to exhibit the period gap. Fig. 1.8 shows a comparison of the periods of the non-magnetic versus magnetic CVs and appears to confirm the weakness or absence of the period gap.

At the accretion spot, near the surface of the white dwarf, kinetic energy is converted to thermal energy through two processes. In the first, the incoming material undergoes a shock at the bottom of the accretion column where the temperature reaches $\sim 20\,\mathrm{keV}$. At this temperature the electrons and protons collide with each other and release their energy as brehmsstrahlung resulting in hard X-ray emission. The second process involves more dense clumps of accretion material that penetrate through the accretion shock and dissipate their kinetic energy below the photosphere of the white dwarf, which re-emits this energy as blackbody radiation at $\sim 20\,\mathrm{eV}$ resulting in soft X-ray radiation. These sources of soft and hard X-ray luminosity accounts for the fact that many polars are found as point sources in the Swift (Evans et al., 2014) and ROSAT (Boller et al., 2016) catalogues of X-ray sources.

1.6   Thesis structure

In this thesis I will investigate the evolution and interaction of compact binaries. Before presenting these chapters, Chapter 2 will review the methods and data sources used. Chapter 3 presents a study of the distribution of orbital periods for a sample of PCEBs and, combining this with a second study shows that the common envelope phase results in a bimodal distribution of orbital periods. Chapter 4 presents a study of a recently discovered CV, V1460 Her, that has an unusual evolutionary history in that it has an early donor star that has likely undergone CNO burning. This system also contains a rapidly spinning white dwarf which is second only to AE Aqr in spin rate and hints that there may be more systems like this, providing an alternative evolutionary story for CVs. In chapter 5 I use photometric and spectroscopic observations of a short period polar, V808 Aur and determine new estimates for important parameters of the system (such as masses of the components) as well as detecting changes in the orbital period. Chapter 6 contains the first observations of a newly detected polar. Extensive spectroscopic observations have allowed us to produce Doppler tomography maps showing the ballistic and magnetic accretion
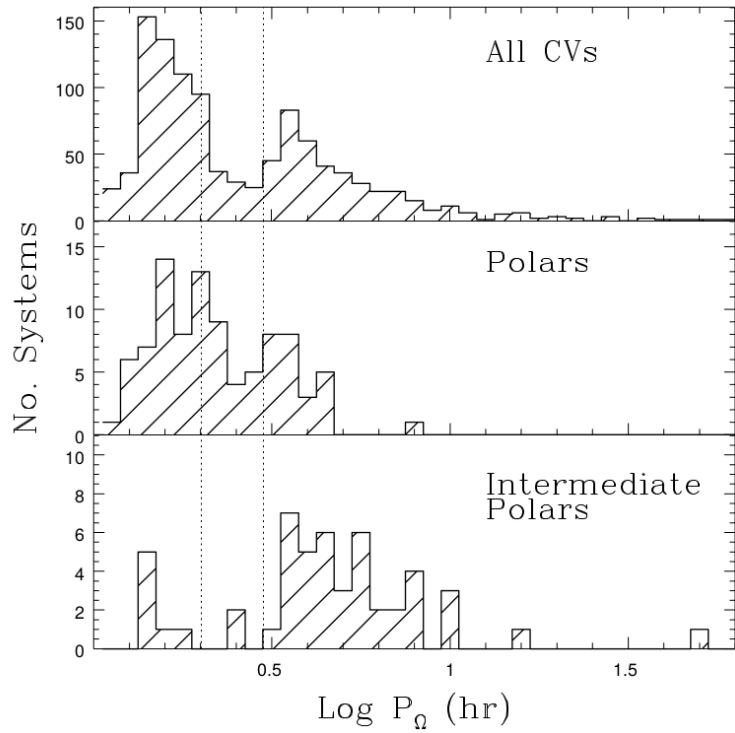
Figure 1.8: The distribution of periods for the CVs as group by their field strength. The upper panel shows the non-magnetic CVs with the period gap in the 2-3 hour range. Middle panel is the polars which tend to have shorter periods than the intermediate polars (IPs), shown in the lower panel. This figure is taken from Ferrario et al. (2015) and derived from data contained in the Ritter and Kolb (2003) CV catalogue.

streams in some detail.

Chapter 2

Methodology

2.1 Introduction

A large portion of the research presented in this thesis is directly derived from observational data, from both photometric and spectroscopic analyses. This chapter will describe these two observational processes and how they provide the data used in subsequent chapters.

2.2 Photometry

Photometry refers to the measurement of the brightness of a star. In order to study a star's behaviour and nature, we make measurements of how intense the star's brightness is as a function of two main parameters. The first of these is time, where we are interested in the star's variability over a period of years or months or even seconds and milliseconds. The second key parameter we measure is the star's relative intensity in different regions of the electromagnetic spectrum which can give clues to its composition, temperature and radial velocity relative to Earth. I now describe the telescopes and instruments used to acquire photometry in this work.

2.2.1 Telescopes and Instruments

Warwick One metre

The Warwick One metre (W1m) is an F/7 equatorially mounted telescope with a one-metre diameter mirror. The instrument is mounted at the Cassegrain focal position and was provided by Liverpool John Moore's University, see Fig. 2.1. It is a dual-channel red-blue photometer with a dichroic filter to split the beam into separate detectors and is capable of taking simultaneous exposures in each band.
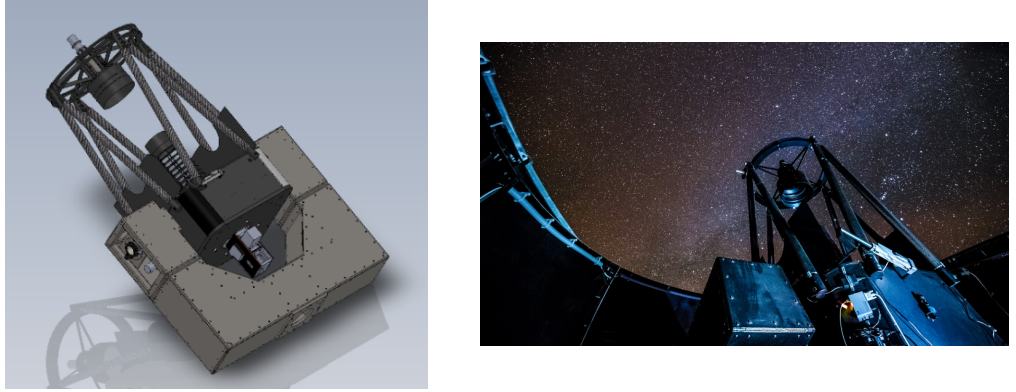
Figure 2.1: The Warwick One metre (W1m) telescope.
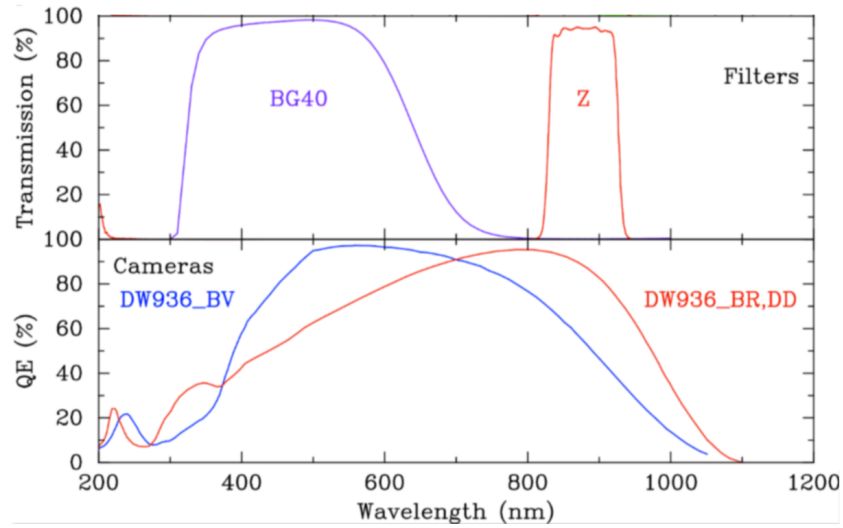
Figure 2.2: The response curves of the filters and cameras on the W1m two channel instrument.

The blue channel contains a BG40 filter which covers wavelengths from 3000 to 6000 Å, and the red channel, a Z-band filter covering 8200 to 9300 Å. The response curves of the filters and the camera sensitivities can be seen in Fig. 2.2.

A large portion of the early work in this PhD thesis was to commission the Warwick One metre (W1m) telescope for operation. This telescope had originally been purchased and installed at the Roque de los Muchachos observatory in 2013/2014 and was funded by a consortium from Queen's University, Belfast and Qatar and was originally named the SuperWASP Qatar followup telescope or SQT. Due to changes in funding arrangements, the telescope was only installed at the site but not commissioned. Ownership of the facility was transferred to the University of Warwick in 2015 and the task of commissioning was given to a post doctoral

researcher at Warwick (Paul Chote) and a PhD student (me).

The three main tasks of commissioning involved a) ensuring the mechanics and optics of the telescope were functioning according to specifications, b) building and installing environmental monitoring and protection for the telescope and supporting systems (such as electronics) and c) augmenting the original control software to enable automated operation of the telescope and building of the reduction pipeline.

After several tests and commissioning runs, it became clear that there were significant flaws with the construction and the optics of the telescope. The most notable of these was a previously undetected crack in the primary mirror, which was attributed as the main cause of a significant astigmatism in the focused images. Since then, the mirror has been refashioned by the provider (Optical Mechanics, Inc). The truss rods that support the secondary ring were also found to be defective in that they slipped and altered their lengths as the telescope slewed. These have been rebuilt and are ready to be installed on site. At time of writing, the telescope is still out of commission, but we anticipate that we will have it operational in 2020.

During the commission and test runs, we were able to make observations of sufficient quality for publication and an example of these are the light curves of V1460 Her in chapter 4.

All of the other time resolution light curves presented in the thesis were taken from one of a family of three high-speed photometers: ULTRASPEC, ULTRACAM and HiPERCAM. All of these instruments use frame transfer CCDs in order to speed up the rate at which individual frames are captured.

ULTRACAM

The first of these instruments to be commissioned was ULTRACAM (Dhillon et al., 2007), which had first light in 2002 on the William Herschel Telescope (WHT) (see Fig. 2.3). It has since been relocated to the New Technology Telescope (NTT) in La Silla, Chile. ULTRACAM was designed to capture optical light from the target in three channels simultaneously. To enable this, the camera has three CCD detectors and two dichroic beamsplitters that divide the light from the collimator into three beams. The three CCD detectors are mounted at right angles to each other and therefore each detector is at the end of a slightly different optical path as is depicted in Fig. 2.4. The images produced on each of the three CCDs chips are of the same field of view but with very slightly different orientations, distortions and offsets. The exposures are synchronised across all three detectors, meaning that all three CCDs start their exposure, stop their exposure and read-out at the same
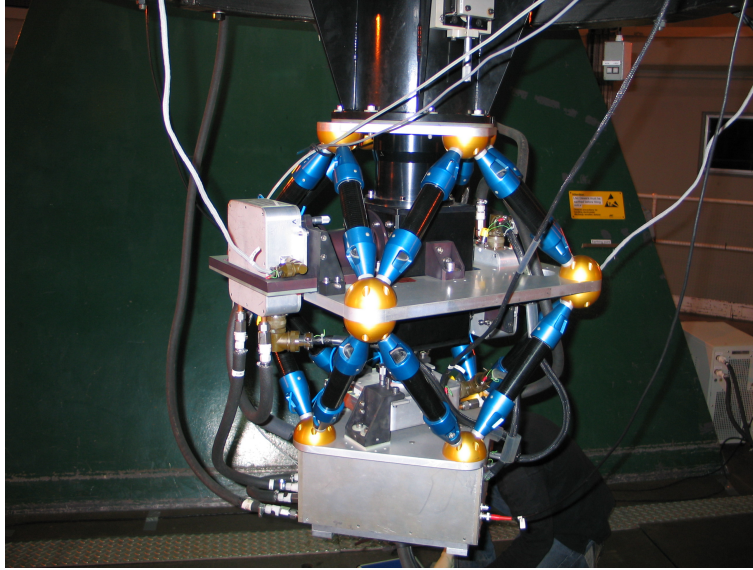
Figure 2.3: ULTRACAM first light on the William Herschel telescope in May 2002. This figure courtesy of Vik Dhillon.

time. It is, however, possible to have the detector in the blue-most channel remain exposed and not read-out while the other two are going through multiple exposures and read-outs. This is to allow for longer exposures where there might be reduced flux in the blue CCD. This reduced flux in the blue channel is caused by several factors, including lower transmission of the optics and atmosphere for blue light, the reduced sensitivity of the CCD detector to blue light and the low intrinsic flux of most astronomical objects in this region of the spectrum.

The filters for each channel can be altered by the observer. Most usually the SDSS filters (u, g, r, i, z) are used, but there are a selection of narrow-band filters that can be substituted. Since the dichroic beamsplitters have fixed wavelengths, it is only really sensible to keep the u filter in the blue-most channel and the g filter in the subsequent arm. Fig. 2.5 shows the response curves of the ULTRACAM camera combined with the SDSS filter set and the atmosphere.

ULTRASPEC

ULTRASPEC (Dhillon et al., 2014) is a single channel version of ULTRACAM and, since 2011, has been permanently mounted on the Thai National Telescope (TNT) on Doi Inthanon, Thailand since November 2013. The camera was originally designed to be a spectroscopic version of ULTRACAM. As a complementary instrument, the intention was to learn more about the kinematics of many of the targets that

23
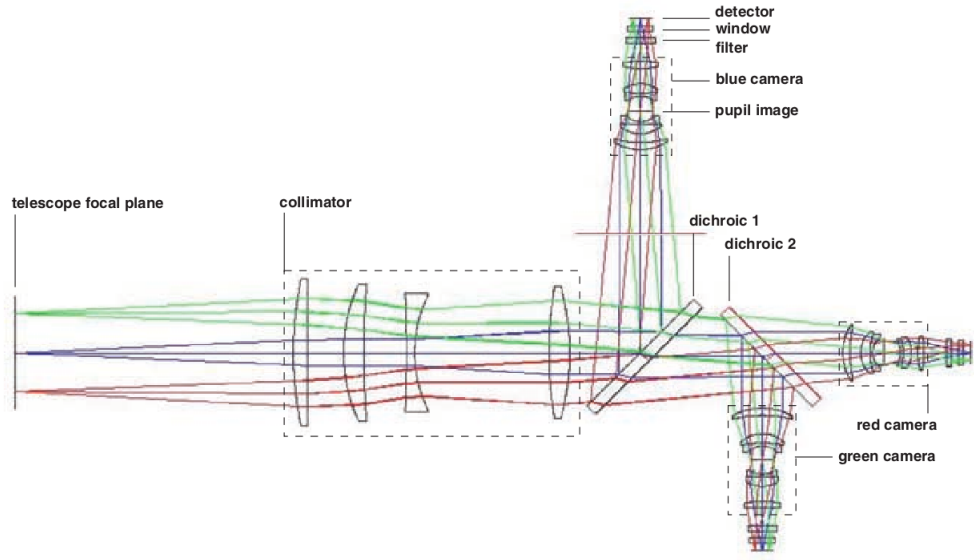
Figure 2.4: A ray-trace through the ULTRACAM optics, showing the major optical components: the collimator, dichroics, cameras, filters and detector windows. The diagram is to scale with the largest lens in the the collimator with a diameter of 120 mm. The diagram is taken from Dhillon et al. (2007).

were typically observed by ULTRACAM. Since there were many compatible existing spectrographs available, ULTRASPEC was initially built as a *bare* instrument, with no optics. It was used as a high speed spectrograph on the ESO 3.6 m telescope and the NTT in La Silla in 2006 and 2008. The CCD is an electron-multiplying (EMCCD) that offers the potential for lower readout noise but at a cost in terms of charge transfer characteristics when used in avalanche gain mode. Since then, the need to find a permanent home for ULTRASPEC has led it to being converted into a high speed photometer and placed on the TNT.

As in ULTRACAM, ULTRASPEC can make use of a variety of different filters. Most usually, the SDSS filter set is used, but these can be substituted for narrow-band and other bandpass filters. A commonly chosen alternative filter is the KG5 filter which is a broad 'white-light' filter approximately spanning the bandpasses of SDSS u, g, and r. Since ULTRASPEC is a single channel instrument, only one bandpass is recorded at any particular time. It hosts a remotely operated filter wheel, containing six slots allowing the observer to change the filters before continuing with observations. Like ULTRACAM and HiPERCAM, ULTRASPEC uses a technique called frame-transfer to speed up the frame rate of observations. In most other scientific CCD cameras, the full surface area of the CCD is exposed. When the
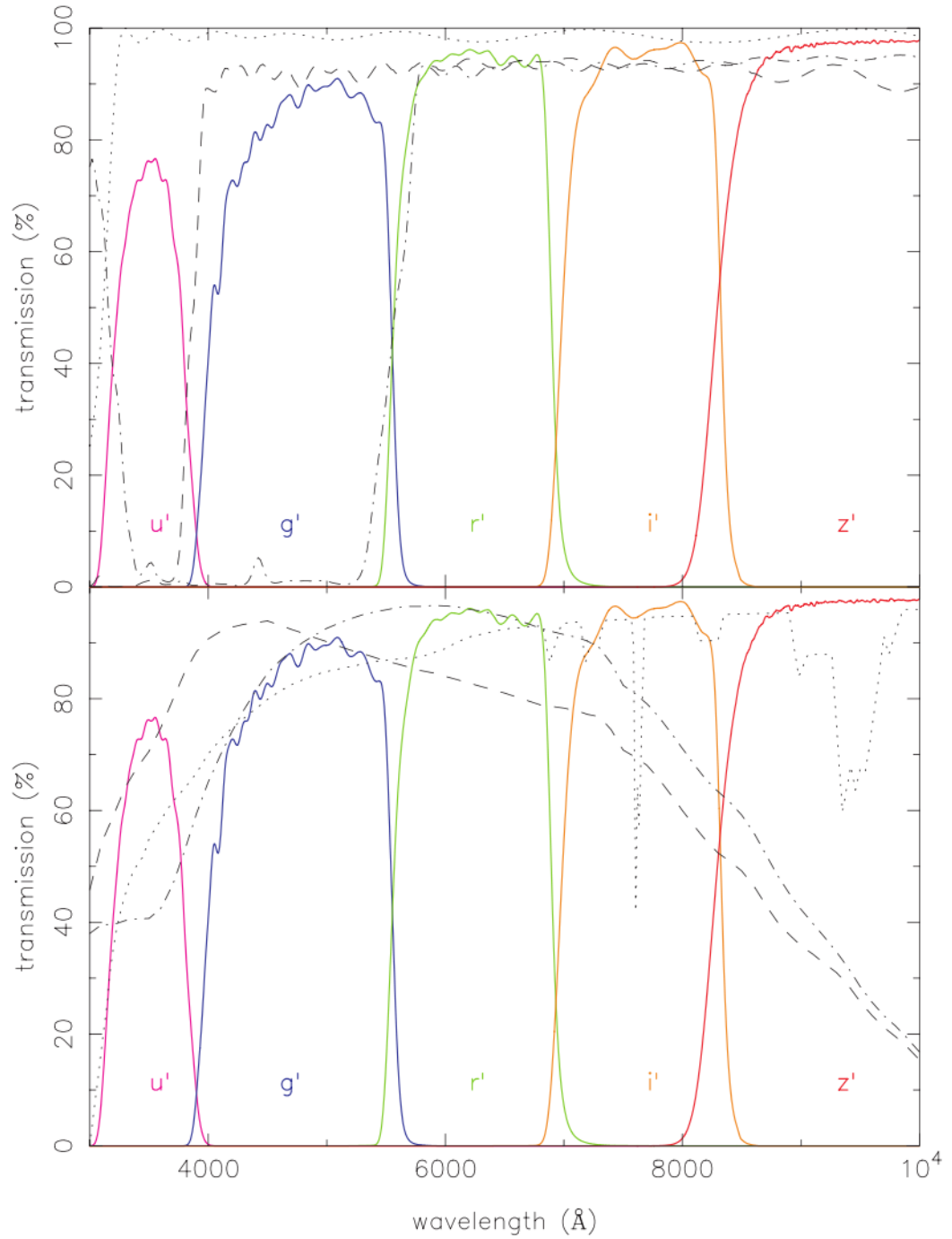
Figure 2.5: The response curves of ULTRACAM with the SDSS filter set. The upper plot shows the SDSS filter set, the response of the anti-reflection coating used on the lenses (dotted line) and the two dichroics (dashed line and dash-dotted line). The lower plot shows response of the SDSS filter set and the atmosphere (per unit air mass). The figure is taken from Dhillon et al. (2007).
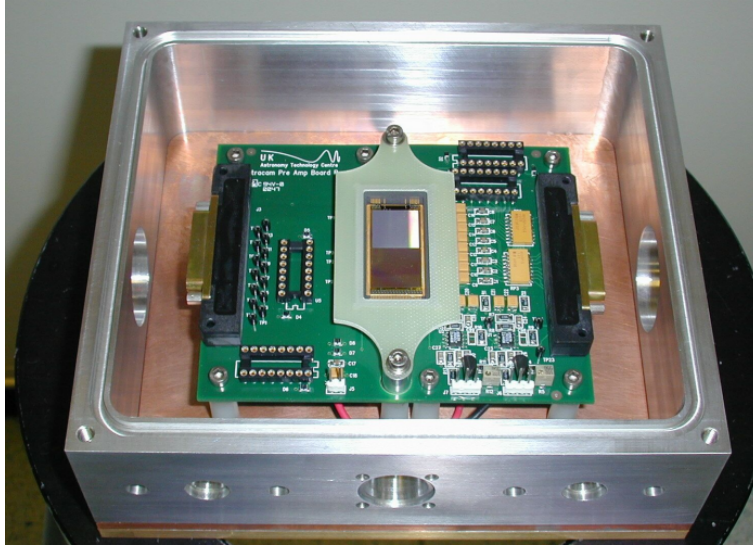
Figure 2.6: A photograph of one of the CCDs used in the ULTRACAM camera. Note that half of the chip area is masked off and not exposed to light. At the end of each exposure, the image is transferred from the unmasked area to the masked area. This transfer is a quick operation allowing the next exposure to start and the slower read-out to take place from the masked area. This image courtesy of Vik Dhillon.

exposure is over a shutter is closed to prevent more light from accumulating and the CCD is slowly read out, pixel-by-pixel. Since this process can take several seconds, there is a reduction in the overall *duty cycle* of the instrument (the percentage of time that the camera is exposed to light from the source). Frame transfer CCDs reduce this problem, by masking 50 per cent of the surface on the chip (see Fig. 2.6), never exposing it to light. Once an exposure is completed, the chip transfers the exposed half over to the masked half, which is a quick operation (on the order of milliseconds) and then the exposed half can start the subsequent exposure while the masked half is read-out, pixel-by-pixel. This means that the duty-cycle of frame transfer CCDs can be very close to 100 per cent. Another method for speeding up read-out times (and hence allowing faster frame rates) is to reduce the amount of the CCD that is read out by defining windows containing only the sources of interest. By having windows defined, the total number of pixels to be read out is greatly reduced, meaning that exposure times can be shortened down to the order of a few seconds. A schematic diagram of the chip setup and read-out process for ULTRASPEC is shown in Fig. 2.7. The overall architecture is similar for the CCDs in HiPERCAM and ULTRACAM.

These three cameras can also make use of a technique called *drift mode* which
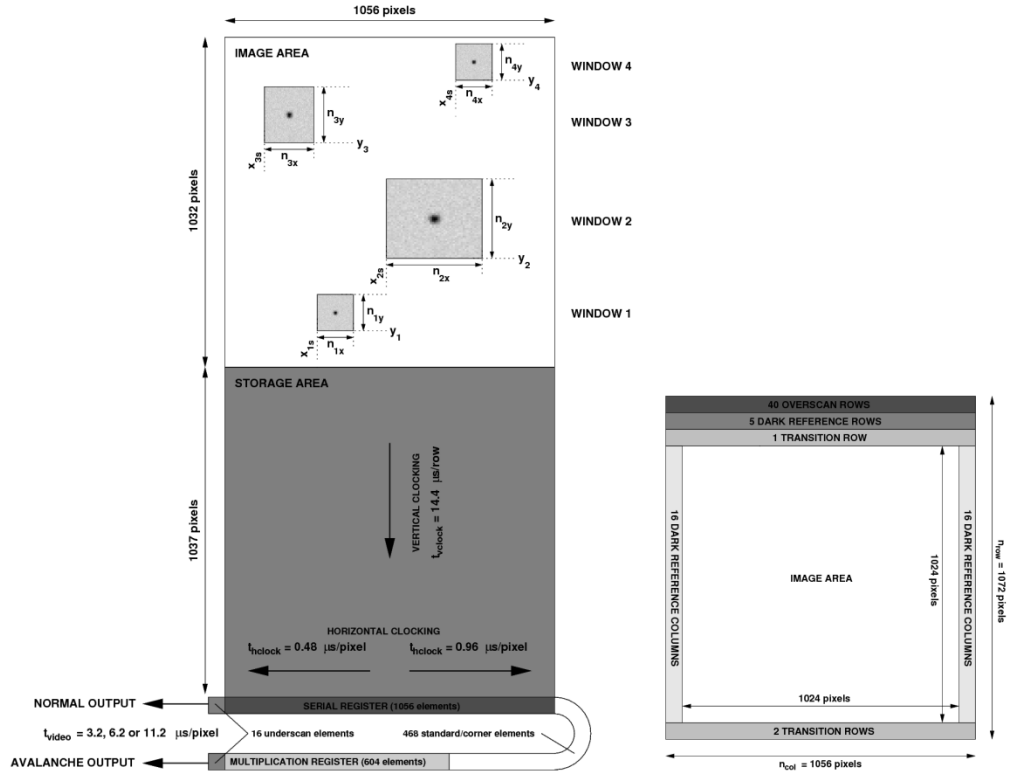
Figure 2.7: Schematic representation of the ULTRASPEC CCD. Up to 4 windows can be defined, or the chip can be read out in full-frame mode, in which case the entire image area is selected. The right panel shows the format of an ULTRASPEC data frame. Only the central 1024×1024 pixels marked on the diagram are sensitive to light. This diagram is taken from Dhillon et al. (2014), Fig. 5.

27

allows the operation of even faster frame rates. This method uses small windows located near the boundary of the exposed and the masked areas of the CCD and, when an exposure is completed, only a portion (enough to cover the window) of the exposed area is transferred onto the masked area. These windows are gradually transferred into the masked area one-by-one forming a series of exposures until they reach the readout area of the masked portion of the chip. This allows frame rates on the order of hundreds per second for ULTRACAM and ULTRASPEC and thousands per second for HiPERCAM. This very high speed mode is only useful for certain science objectives such as lunar occulations of bright stars, where the knife-edge effect leads to a diffraction pattern that can be used to measure the apparent diameter of stars (Richichi et al., 2016) or, in the case of polars where the accretion stream shock above the white dwarf surface can lead to quasi-periodic oscillations on the timescale of 1-2 seconds, as an example this is covered for the polar VV Puppis in Bonnet-Bidaud et al. (2019). Since *drift-mode* was not used in this thesis, it is only summarised at a high level here; for more detail see the appendix of Dhillon et al. (2007).

HiPERCAM

HiPERCAM (Dhillon et al., 2016) is the latest addition to this series of high speed photometers. It had its first light on the William Herschel Telescope in October 2017 and subsequent installation on the Gran Telescopio Canarias in February 2018. It improves upon the ULTRACAM design in a number of areas, most notably, it is able to record data in five channels simultaneously. A set of bandpass filters, specifically designed for HiPERCAM, match the SDSS wavelengths but have significantly greater throughput than those used in ULTRACAM. These filters do not use the typical coloured glass, but have multi-layer coatings to define the filter bandpasses. The percentage improvements in throughput of the HiPERCAM Super SDSS filters, which are named u_s, g_s, r_s, i_s, z_s , over the original SDSS filters, u, g, r, i, z, are 41/9/6/9/5 per cent, respectively, see Fig. 2.8. All of the five CCDs are manufactured from deep depleted silicon which maximises quantum efficiency. The i and z channel CCDs also incorporate a back surface that contains irregularities which has the effect of reducing fringing. For a side-by-side comparison of the technical specifications of ULTRACAM and HiPERCAM, see Table 1 of (Dhillon et al., 2018).
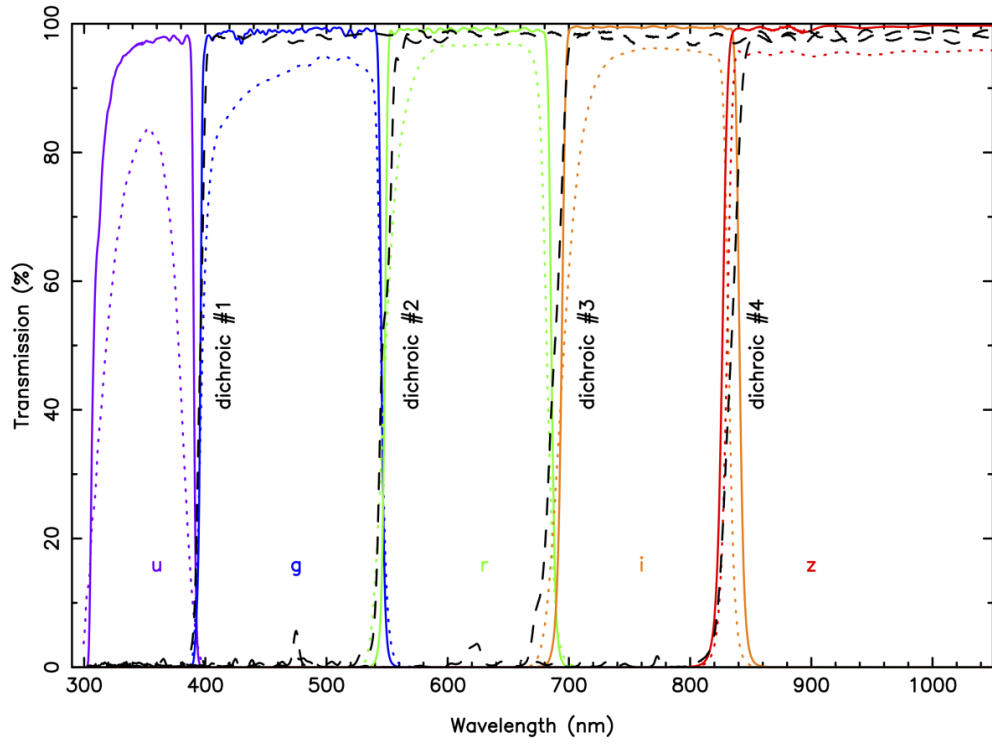
Figure 2.8: The response curves of HiPERCAM with the new Super SDSS filter set. The dotted lines show the response curves of the original SDSS filters and the dashed lines show the response of the four dichroic beamsplitters. The figure is taken from Dhillon et al. (2018).

2.2.2 Photometric reduction

Reduction refers to the process of taking the raw data recorded by the cameras and producing a time series of photometric flux in the bandpass of the filter as a function of time. The ULTRACAM, ULTRASPEC and HiPERCAM data in this thesis were reduced using the HiPERCAM reduction pipeline. For the W1m observations we used the software package TSREDUCE which was developed originally for the Puoko-nui (Chote et al., 2014) photometer and has now been optimised to reduce W1m observations. In both pipelines the overall steps are the same and will be described below.

CCD image capture

All of the cameras we used are imaging devices, meaning that an image of the sky is captured by the light sensitive charge-coupled device (CCD) at the focal plane of the camera. The CCD consists of a matrix of light sensitive semi-conductor elements in a two dimensional array. Most modern CCDs have dimensions of thousands of pixels. Incident photons are counted by the semi-conductor in the pixel as they cause electrons to cross the valence gap. Once an exposure is over, these electrons are 'read-out' and converted into counts or analogue digital units (ADU). The inverse of the number of counts per electron is known as the gain of the CCD. This seems counter-intuitive but it is defined this way by convention. The process of reading out occurs serially as individual pixels are shifted one by one for conversion into ADUs by the analogue to digital convertor and this process can be quite time consuming, on the order of tens of seconds for some cameras. The speed at which the counting and shifting of the pixels is performed is usually adjustable and can be increased at the cost of some additional noise. Most cameras have a 'slow' and 'fast' read-out mode.

In order to mitigate the serial approach to read-out, some cameras like ULTRACAM, HiPERCAM and ULTRASPEC use the frame transfer (see section 2.2.1) approach to allow the exposure to restart during a read-out phase and thereby increase the overall duty-cycle of the camera.

Bias and Dark frames

CCDs have a voltage bias applied to them which results in a non-zero number of counts in each pixel even if it is not exposed to any light. We measure this bias level by taking a number of *bias* frames and then computing the median level for each pixel in the array. These bias levels are subtracted on a pixel-by-pixel basis

from every frame in our other exposures. Since the bias level can vary due to environmental factors such as shifts in voltage levels of the CCD circuitry, we take these bias frames on at least a nightly basis. Bias levels also vary depending on the CCD read-out arrangement, so if, for example, we alter the read-out regions of the chip or adjust the pixel binning, new bias levels need to be determined for this particular configuration. This is also true for fast and slow read-out speeds. Examination of the bias frames allows an estimate of the read-out noise to be made. Read-out noise is an inevitable product of the read-out process and is also affected by external electrical interference, for instance if there is poor shielding from nearby equipment. It can be approximated by the standard deviation of counts for each pixel of a series of bias frames. Another simple way of estimating the read-out noise is to calculate the standard deviation of a group of nearby pixels on a single bias frame, assuming that we expect nearby pixels to have a similar overall bias. Read-out noise is independent of the number of counts in the pixel and usually this source of noise is well below that expected from other sources. However, if we are examining faint objects where we do not expect the level of counts to be high, the contribution from read-out noise can be significant and then it can be helpful to bin pixels to reduce this effect.

Dark frames are taken to characterise the additional counts that may be generated by thermal excitation of electron in the CCD. All of the cameras used in this research were cooled in order to offset this effect. The cameras in HiPERCAM and ULTRACAM are cooled with several stages of Peltier coolers to take the chips down to 230 and 180 K respectively. The Andor cameras in the W1m also use Peltier coolers to achieve a temperature on the chip of 210 K. ULTRASPEC and the cameras used in the IDS and ISIS spectrographs make use of liquid nitrogen to achieve temperatures of around 150 K. Nevertheless, some dark current is always present in camera and to measure this we take a series of exposures in darkness with no light reaching the CCDs. Based on the ADU counts for each pixel and the duration of the exposure we can scale this to match the length of our science exposure and deduct this dark current.

Flat fields

The counts measured in response to a given light intensity will vary according to the position it falls on the CCD. This is due to a combination of factors that affect the light as it follows the optical path through the telescope. Vignetting, filter throughput and pixel sensitivity all play a role. To correct for this, we start and end each observation night with a series of flat fields taken while exposing to the twilight

lit sky. The assumption is that the light from the sky begins its journey through the telescope as a uniformly illuminated image and this is then attenuated along the path so any spatial variations in the recorded image are due to instrumental effects. Since each filter will introduce its own characteristic response in combination with the rest of the telescope, we take separate flats for all filters. A number of flats are binned together with the median value applied on a pixel-by-pixel basis and normalised to produce a spatial response frame (or 'balance' frame). These frames are then used as a multiplier to account for spatial variation across the field.

Synthetic Aperture Photometry

For each frame in a science run, the data is bias subtracted, dark subtracted, and flat field corrected. The frame is then ready to be analysed to extract the number of counts for the targets of interest. Although all stars as seen from Earth are effectively point sources since their apparent diameter is well below the resolving power of any optical telescope, their light spreads out across a finite spatial area. Each star in the image has a point spread function (PSF), which defines the distribution of its light across the CCD. The profile of the PSF is independent of the overall intensity of the star's flux and can be approximated by a Moffat function (Moffat, 1969),

$$I(x,y) = I_0 \left(1 + \left(\frac{x^2 + y^2}{\alpha^2} \right) \right)^{-\beta}, \tag{2.1}$$

where x and y are the coordinates in the plane of the detector, measured from the centre of the image of the star. Both α and β are seeing-dependent parameters and can be used to derive a seeing estimate, as shown in equation 2.2. It is possible to fit a numerical function to the profile of the star and then derive the values of α and β to determine a value for the full width half maximum (FWHM) calculated using the equation,

$$\text{FWHM} = 2\alpha\sqrt{2^{1/\beta} - 1}. \tag{2.2}$$

In order to measure the overall brightness of each star in a particular CCD frame, we can imagine placing apertures over each star in the field of view. Before CCDs were were available, photomultipliers used and, since these were single channel detectors, in order to isolate the flux of the target of interest, a physical aperture (metal disc with a circular hole cut out of it) was placed in the light path to block light from the rest of the field while recording data. Now, with CCD images virtual apertures are used. By defining regions of the CCD that contain our targets of interest, reduction software is then used to model and calculate the flux within
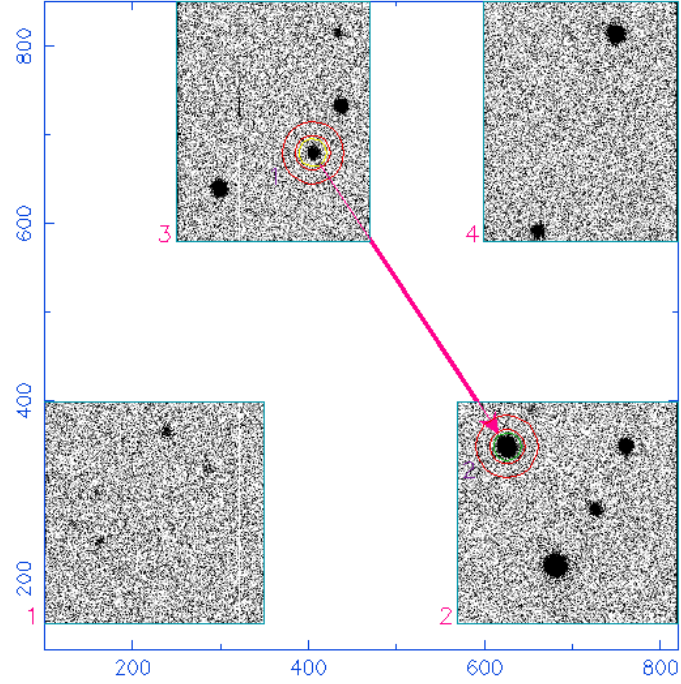
Figure 2.9: An image showing a reduction of an ULTRACAM observing run. In this case, only two objects are being analysed. The first (upper left) is the target and the second a comparison star. Note the circular apertures and the concentric rings for sky measurement as discussed in the text.

those regions. Typically apertures are defined as circles around each star and the counts of all the pixels in the region are summed. Nearby the region, usually in a concentric ring, we can also measure the amount of the counts that are coming from the non-zero contribution of the sky.

The HiPERCAM reduction pipeline that was used to reduce all of the high-speed photometric data and the TSREDUCE software for the W1m both allow definition of multiple apertures and a dynamic approach to aperture sizing depending on the changing conditions (for example variable seeing) during the run. Both pipelines also take into account the subtraction of the bias frames and the scaling of the flat fields.

In addition to the data collected with the W1m and the high-speed cameras, significant use was made of wide-field survey data. I introduce these resources in the next section.

2.2.3 Survey photometry

In this thesis we make use of publicly available data that has been gathered from surveys which have their own core scientific goal. These surveys offer data archives that are useful to other fields of research since they contain a large set of targets and a long timeline of observations. It is thanks to the open access of these surveys that we are able to either discover targets of interest, or follow up on known targets for supplemental data.

Catalina Real Time Transient Survey

The Catalina Real-time Transient Survey (CRTS) (Drake et al., 2014b), was a survey that was derived from using the data taken by the Catalina Sky Survey, which had the primary goal of detecting and tracking near-Earth objects. The reason for this mission was to try to catalogue as many potentially hazardous asteroids as possible. Potentially hazardous asteroids are defined as those that are at least 140 m in size and in near-Earth orbit. The observations were made by three autonomous telescopes, a 1.5 m mounted on Mount Lemmon, in Arizona, USA, the 0.7 m Catalina Sky Survey telescope on Mount Bigelow, also in Arizona, USA and a 0.5 m telescope at Siding Spring in New South Wales, Australia. Using this core data, CRTS monitored all known stellar objects in its catalogue looking for changes in flux. When a significant variation was detected, an alert was triggered and shared publicly via an Astronomer's telegram to allow others to follow up. It was through one of these alerts that we picked up and followed the outburst of the CV V1460 Her which is covered in chapter 4. CRTS also maintains an online catalogue of all photometric observations which begins in 2005 and extends to mid-2013 (some newer data remains unreleased). This archive was used for supplemental data in chapters 5 and 6.

SuperWASP

The Wide Angle Search for Planets (WASP) (Pollacco et al., 2006) was founded in 2000 by a group of primarily UK-based astronomers with common goal of detecting exoplanets through photometry of a wide area of the sky covering many bright stars. WASP consists of two telescopes of specific design, located in Roque de los Muchachos, Canary Islands and the South African Astronomical Observatory at Sutherland, South Africa. The cameras are known as the *SuperWASP* cameras. As shown in the photograph Fig. 2.10, the mount houses six independent camera assemblies. This allows for a large area of sky coverage and overlapping regions.
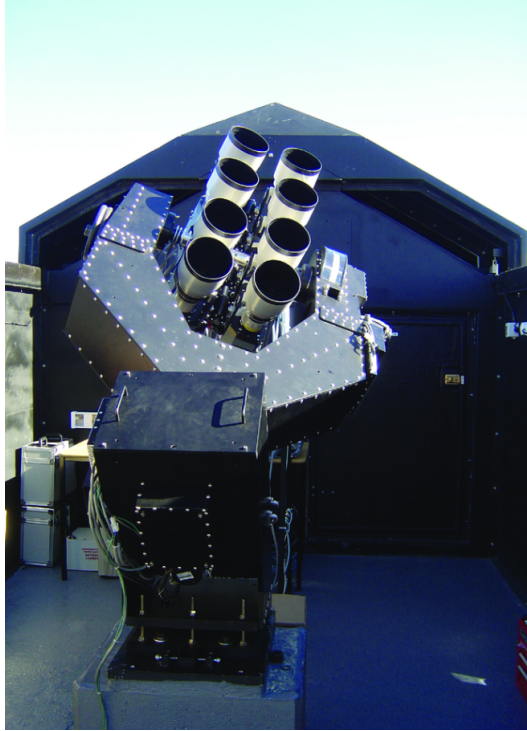
Figure 2.10: SuperWASP at the Roque de los Muchachos observatory.

SuperWASP was operational from 2003 until 2017 although the publicly available archive only extends until 2013. This archive has been valuable in providing useful data on V1460 Her allowing us to investigate its average light curve and the frequency of outbursts as discussed in chapter 4.

ASAS-SN

The All-Sky Automated Survey for Supernovae (ASAS-SN) survey (Shappee et al., 2014; Kochanek et al., 2017) is an all-sky survey is primarily focused on looking for bright transients, particularly aimed at obtaining a complete inventory of nearby supernovae to characterise the local supernova rate and its correlation with galaxy type and properties. ASAS-SN currently consists of four stations, located at the Haleakala Observatory (Hawaii) and the Cerro Tololo International Observatory (CTIO), Chile, McDonald Observatory, Texas, and the South African Astrophysical Observatory (SAAO) in Sutherland, South Africa. Each station consists of four 14 cm aperture Nikon telephoto lenses and a ProLine CCD camera. The original choice of filter was Johnson V, but as new stations came online, the Sloan g band filter replaced this. Although the ASAS-SN survey sensitivity does not match that of

CRTS, since its cameras have a much smaller aperture (it is similar to SuperWASP in this regard), this shortcoming is made up for by its all-sky coverage which includes all galactic latitudes. In this thesis we have used the ASAS-SN archive to supplement the CRTS data on objects, since coverage of ASAS-SN picks up soon after the current release of CRTS ends (mid-2013).

Palomar Transient Factory

The Palomar Transient Factory (Law et al., 2009), was an automated survey that launched in March 2009 with the objectives to detect supernovae, rapid transients, eclipsing binaries and a map of extended Hα sources. After its initial period of five years, it was upgraded and has now been revised into the Zwicky Transient Factory (ZTF). It uses the 48″ Samuel Oschin telescope at Palomar observatory for detection of transient events and the 60″ Palomar telescope for follow-up photometry. It is able to detect sources down to a limiting magnitude of around 20. With the upgrade to ZTF, the survey is now able to sample all of its visible sky each night. Like the other surveys it publishes an online catalogue of transient photometry which is available for download. This source was used for supplemental data in our analysis of the light curves of the WD-dM binaries WD 1458+171 and WD 1504+546 in chapter 3.

AAVSO

As mentioned in the introduction, the study of variable stars was pioneered and has continued to be supported by observations made by non-professional astronomers. Since our main objects of interest in this thesis are CVs and polars, which are known to outburst, erupt as nova or to change from high-state to low-state, these are objects that are well suited to citizen astronomers with modest telescopes and equipment. The American Association of Variable Star Observers (AAVSO) serves as a global, centralised source for collecting and sharing the observations made by a diverse set of members. Its public archive is a very useful resource for historical data particularly when looking for long term events or trends. As a community for interested parties, the AAVSO is also a useful resource for recruiting additional observers to support the work of professionals as described for the *HST* observations in chapter 4.

2.3 Spectroscopy

While photometry, described in the previous section, measures the behaviour of the flux of the star over a period of time in a defined passband, spectroscopy is the

process of taking measurements of the star's spectrum in order to observe additional information about its dynamics and chemical composition. Like photometry, spectroscopy can take a series of measurements over a period of time that reveals how these components evolve. In this study we have used time-series spectroscopy to reveal the dynamics of orbiting close binaries.

2.3.1 Telescopes and Instruments

IDS

The Intermediate Dispersion Spectrograph (IDS) is a long-slit spectrograph which sits at the Cassegrain focus of the 2.5m Isaac Newton Telescope on the island of La Palma in the Canary Islands, Spain. It had first light in March 1984. IDS has two 4096×2048 pixels CCD detectors, a red sensitive detector (RED+2) and a blue sensitive detector (EEV10). There are 16 gratings available, but for all of the observations discussed in this thesis we used the R831R grating. More information on this grating is provided in chapter 3.

ISIS

The Intermediate-dispersion Spectrograph and Imaging System (ISIS) is mounted at the f/11 Cassegrain focus of the 4.2 m William Herschel Telescope also on La Palma, see Fig. 2.11. The first light of ISIS was in autumn 1989. It uses dichroic filters to split the light beam and permit simultaneous observing in blue and red arms, Each arm is optimised for its respective wavelength range, and specific wavelength ranges are set by rotating the grating cells. For the study of the CV and polars in chapters 4, 5 and 6 we used a selection of gratings to select features and wavelength scales to suit our science goals.

2.3.2 Spectroscopic reduction

Both ISIS and IDS are long slit spectrographs. This means that light from the star is placed on a slit that lies in the focal plane of the telescope which then forms a one dimensional slice of the field of view with the star somewhere within that projection. This light is then sent to a collimator that projects it onto the diffraction grating where the 1-D image is dispersed. This dispersed light is then refocused onto the focal plane of the instrument where the CCD records it. The methods of CCD read-out are the same as for the imaging CCDs described in the photometry section. An example of the image recorded by the CCD is shown in Fig. 2.12.

Figure 2.11: ISIS: A two channel intermediate dispersion spectrograph. Shown mounted at the Cassegrain focus of the William Herschel Telescope.
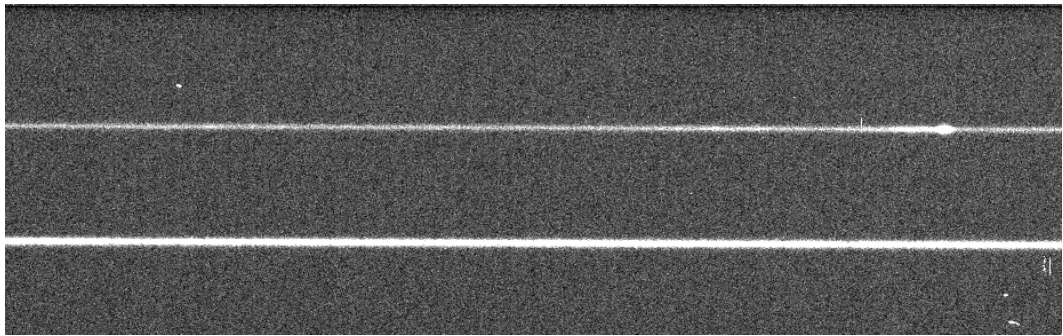
Figure 2.12: An example of a raw CCD image taken in the blue arm of ISIS. This image has been rotated by 90° from the default view as seen during observations at the telescope. The horizontal direction in this image is the dispersion direction and the spatial direction is represented vertically. This example was taken from our observations of CRTS2152 on 2017 July 04 as covered in chapter 6. In order to take into account slit losses, we placed a second target on the slit. CRTS2152 is a polar and is characterised by bright emission and a low continuum as can be seen in the upper spectrum. The comparison (lower spectrum) is a main sequence star.

Biases and Flats

As we did in photometric observations, for spectroscopy we also need to take bias frames in order to characterise the bias levels of the CCD for the particular setup that we are using. For this purpose we take dozens of bias frames for each CCD configuration that is used on a particular observing night. The overall optical arrangement leads to a variable response spatially across the CCD and this is due to vignetting, filters and the response of the grating spatially. We measure this overall response by taking flat fields for each optical configuration that we use during the science observations. Although we can use the twilight sky to make flat fields, we often use an internal lamp and perform this calibration during the day. Both IDS and ISIS use a tungsten lamp as the illumination source for the flat fields. In order to produce a flat that contains the pixel-to-pixel responses (as well as the response variation due to vignetting, etc) we need to remove the instrumental response as a function of wavelength as well as the spectrum of the lamp itself. We do this by fitting a low order polynomial to a collapsed (in the spatial direction) 1-D array and dividing the 2-D map by this fit. This then is our response map or 'balance' frame.

Spectrum extraction

As seen in Fig. 2.12 the spectrum forms a linear trace on the CCD image. This trace is close to, but does not form a completely straight line on the detector. This is due to several effects such as misalignment of the CCD with the slit and atmospheric dispersion. Atmospheric dispersion leads to the position of the star's image on the detector being dependent on wavelength. One can imagine that (particularly at high airmasses) the star's light, dispersed by Earth's atmosphere is a superposition of the range of colours with red higher up and blue closer to the horizon. We try to minimise this problem by aligning the slit of the spectrograph in a vertical direction (from horizon toward zenith) by rotating the instrument. The correct angle for vertical alignment is called the parallactic angle and is covered in Filippenko (1982). For our observations we attempted to do this whenever possible, but we unable to do so in certain situations, such as for observations of CRTS2152 where we felt it was more important to have an additional comparison star on the slit. Since this effect is dependent on wavelength, it is less severe when we are examining a relatively narrow range of wavelengths such as in the case of CRTS2152.

As can be seen in Fig. 2.13, the sky contribution to the spectrum is not only a continuous background source as in photometry, but can be highly wavelength dependent. In order to take the sky into account, we define linear regions alongside
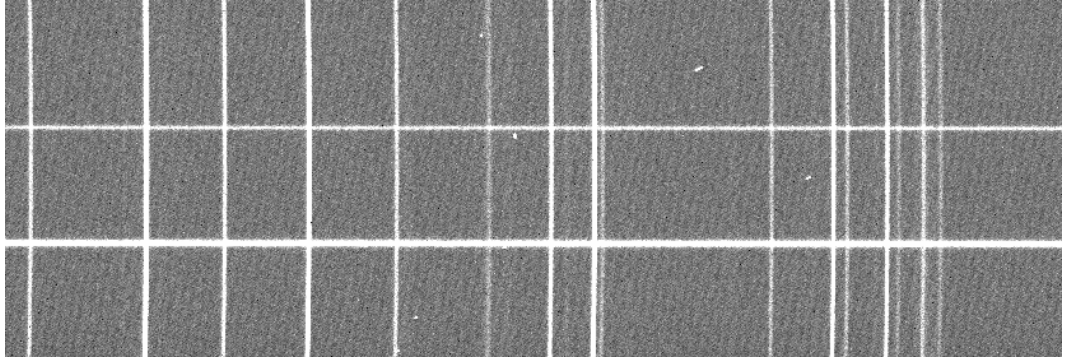
Figure 2.13: A raw ISIS image taken from the red arm. As in Fig. 2.12 both the target and comparison are seen as horizontal traces. In this wavelength range ($\simeq 8100$ to $\simeq 8300$ Å) there are prominent emission lines from the sky and these can be seen as vertical features in this image.

the trace of the spectrum, on either side. These are the spectroscopic analogues of the concentric rings used for the photometric reduction. These sky regions are then used to model a polynomial that we interpolate through the spectrum to enable us to estimate the sky contribution on a per pixel basis.

Now that we have the bias-subtracted, flat-field corrected and sky-subtracted data in the two dimensional array, we need to sum the contribution from all pixels that contribute to the spectrum. The most simple method is to follow the trace of the spectrum, summing pixels within a certain distance of the trace, taking into account the width of the PSF. This is known as 'normal' extraction. Horne (1986) showed that the extraction S/N can be improved by weighting the sum by an estimate of the amount that each pixel contributes to the overall spectrum. Marsh (1989a) improved this method by adapting the approach to follow the curved path of the spectrum on the detector. Their equation 4 is quoted here,

$$W_i = \frac{P_i/V_i}{\sum_j P_j^2/V_j} \qquad (2.3)$$

where P_i is the fraction of the total flux of the row that is contained in pixel i, and V_i is the variance on pixel i. Extraction using these weights is known as 'optimal extraction'. The pixel contribution P_i is determined by fitting a polynomial along a curved path following the trace of the spectrum.

Flux and wavelength calibration

During the night of the observations, spectra of arc lamps are taken with the same configuration as the science spectra. This means ensuring that the instrument has the same slit size, central wavelength and grating as when taking the target observations. Since the instrument may be re-configured during the night and does not accurately return to the same configuration, arc spectra are required after every configuration change (if accurate wavelength calibration is important). In both IDS and ISIS, copper-argon (Cu+Ar) and copper-neon (Cu+Ne) arc lamps are used. During the reduction process these arc lines are analysed by fitting Gaussian profiles to strong emission features of the lamps with known laboratory wavelengths, matching pixel position to wavelength. These pixel-wavelength pairs are then fitted with a polynomial to produce a function that returns a wavelength per pixel position for the length of the grating. Since the instrument is prone to flexure during the course of the night, it is important to take several arcs as the telescope moves across the sky. In most of our observations, we remain on the same target for several hours and, in order to account for this, we take arc lamps every 40 minutes or so. During reduction we use these series of calibration exposures to interpolate the mapping of pixel to wavelength over time and telescope position.

Two other steps were used to further improve our wavelength calibration. The first of these steps was to use the measured wavelengths of the sky lines seen in the spectra. Since these are terrestrial in origin, or 'telluric', we can assume they are constant in the rest frame of the telescope and therefore any changes in their measured wavelength is due to calibration errors and/or flexure in the instrument. The second of these was to place, where possible, a second target on the slit and use this as a calibration point. Our assumption is that the comparison has a constant systemic velocity that does not alter during the course of our observations. By cross correlating each spectrum of the comparison with a single sample of the same spectrum we can detect changes in the overall calibration of the instrument.

We perform flux calibration by taking the spectrum of a known calibration (or standard) star during the same night as the observations. By comparing this observed spectrum to an existing, published known spectrum we can calculate the flux corrections required to bring the observed spectrum in line with the known spectrum. These corrections are then applied to our target spectra to produce a flux calibrated version.

These sources of photometric and spectroscopic data provide the information used in the subsequent chapters, allowing the study of spectral energy distribution, transient behaviour and the orbital dynamics in our chosen binary systems.

Chapter 3

Post Common Envelope Binaries

3.1 Introduction

As discussed in the introduction chapter, the common envelope phase is an important step in the evolution of compact binaries. Generally, a common envelope is required in order to bring about a reduced separation of the individual stars. During this phase the two stars can be brought close enough for direct interaction and therefore provide new a mechanism for common evolution leading to exotic objects that could not have evolved in an isolated context. Compact binaries also lead to more catastrophic outcomes, such as supernovae, so understanding this phase is critically important to explaining the origin of these phenomena. One class of objects that is worthy of study in this area is that of binaries containing a white dwarf and a main sequence star. In these systems we can be certain that one (and only one) of the two stars has undergone evolution from the main sequence and through the giant branch to become a white dwarf. Willems and Kolb (2004) show that, for these systems, we expect a bi-modal distribution of the orbital periods.

      In order to test the underlying period distribution of WD+MS binaries an observationally-derived period distribution of an unbiased sample is required. In recent years, large scale surveys such as SDSS (Alam et al., 2015) have enabled the study of the orbital period distribution of a sample of WD+MS binaries and measurement of the fraction of those that have undergone a common envelope phase (Rebassa-Mansergas et al., 2012; Nebot Gómez-Morán et al., 2011; Schreiber et al., 2008, 2010). These studies have shown broad agreement with predictions of the fraction of PCEBs versus widely separated binaries and the shape of the period

distribution for the PCEBs themselves. Nebot Gómez-Morán et al. (2011) concluded that about a third of the WD+MS binaries identified by SDSS were short period PCEBs and the rest were candidate wide binaries. These were systems that, at the SDSS imaging resolution, $\approx 1 - 2''$, would still be unresolved, but since they are at distances of a few 100 pc, they would have separations of 100 au or more.

In this chapter, we use spectroscopy to search for radial velocity variations in 20 WD+MS binaries to ascertain if they are PCEB systems. We start with a sample created by Farihi et al. (2006) that were selected by searching for white dwarfs with near-infrared excess. Our targets were chosen from those that were shown to be unresolved in images taken by the *Hubble Space Telescope* (*HST*). In the context of post-common envelope evolution, theory predicts these systems should all be close binaries.

3.2 Observations

3.2.1 Target selection

Farihi et al. (2010) obtained *HST* high-resolution imaging of WD+MS binaries to test the bimodal period distribution with an unbiased sample. The targets selected were chosen from the McCook and Sion (1999) catalogue of white dwarfs which were found to exhibit a near-infrared excess in 2MASS photometry by Wachter et al. (2003). A complete list of the original targets can be found in Table 1 of Farihi et al. (2006).

The Advanced Camera for Surveys (ACS) High-Resolution Camera (HRC) was used to image these targets with the F814W filter to try to resolve each suspected binary. The results of this exercise can be seen in Table 7 of Farihi et al. (2010), where it was found that 72 of the 90 candidates were highly probable binaries and, of these, 43 systems were spatially resolved with the ACS HRC. Combining the angular separation with distance estimates to each target allowed Farihi et al. (2010) to compute the minimum value for the semi-major axis (at zero inclination) for each binary pair.

The remaining 29 systems were unresolved at the resolution of the *HST* imaging. Taking the spatially resolved limit of one pixel on the ACS HRC camera (0.025 arcsec) as the resolving power of the imaging study, it was possible to place upper limits on the apparent separation on these unresolved targets. At the distances to these targets, the limits are about 10 au, corresponding to orbital periods of tens of years. We have attempted to obtain radial velocity measurements of these systems.

We obtained spectroscopy of 20 of the 29 WD+MS binaries that were acces-

Table 3.1: Spectroscopic configurations used in this study. The instrument used was the Intermediate Dispersion Spectrograph (IDS) mounted on the 2.5m Isaac Newton Telescope at the Roque de los Muchachos observatory on the island of La Palma, Spain. All of the observations were taken with the R831R grating. For each night we list the standards used for flux calibration and telluric removal.

Date	HJD	Central wavelength	Standards used
2015/02/10	2457064	8300 Å	Feige 34, BD+26 2606
2015/02/11	2457065	8300 Å	Feige 34, BD+26 2606
2015/02/12	2457066	8300 Å	HD 19445, HR1342
2015/02/13	2457067	8300 Å	BD+26 260, HR6110, HR1342
2015/02/14	2457068	8300 Å	HR6110, HD 93521, HZ 15
2015/02/15	2457069	8300 Å	HD 84937, HR3958, HD 93521
2015/02/16	2457070	8300 Å	HR6110, HD 93521
2015/02/17	2457071	8300 Å	HD 19445, HR6110, HD 93521
2015/09/03	2457269	8200 Å	Wolf 1346, G191-B2B
2015/09/04	2457270	8200 & 6562 Å	Wolf 1346, G191-B2B
2015/09/05	2457271	8200 & 6562 Å	Wolf 1346, G191-B2B
2015/09/06	2457272	8200 & 6562 Å	Wolf 1346, G191-B2B
2015/09/07	2457273	8200 & 6562 Å	Wolf 1346, G191-B2B
2015/09/08	2457274	8200 & 6562 Å	Wolf 1346, G191-B2B
2016/02/12	2457431	8022 & 6565 Å	G191-B2B, Grw+70 5824
2016/02/13	2457432	8022 & 6565 Å	G191-B2B, Grw+70 5824
2016/02/14	2457433	8022 & 6565 Å	G191-B2B, Grw+70 5824
2016/02/29	2457448	8022 & 6565 Å	G191-B2B, Grw+70 5824
2016/03/01	2457449	8022 & 6565 Å	G191-B2B
2016/03/02	2457450	8022 & 6565 Å	G191-B2B, Grw+70 5824
2018/06/18	2458298	8190 Å	Feige 98, Grw+70 5824, L1512-34

sible from the Isaac Newton Telescope at the Roque de los Muchachos Observatory, Canary Islands, Spain using the IDS spectrograph. A log of these observations is shown in Table 3.1. To constrain and potentially determine the orbital periods, the observations were taken in the I-band $(6500-9000\,\text{Å})$ region to measure features in the atmosphere of the secondary, and monitor them for radial velocity variations. The Na I doublet at 8183.3 and 8194.8 Å and the Hα line at 6562.8 Å were used.

As a followup to our spectroscopy, we examined the CRTS and PTF online archives to look for photometric observations for all of our targets. We discovered that of our 20 systems, 16 had CRTS photometry and 10 had PTF photometry. In the cases of WD 0303−007, WD 1458+171, and WD 1504+546, these data provided additional insight and this is discussed in section 3.4.

3.2.2 Reduction

The spectra were obtained using the Intermediate Dispersion Spectrograph (IDS) with the R831R grating. This is a medium dispersion grating with a dispersion of $0.75\,\text{Å}$ per pixel and a resolving power of $R = 4667$ at $7000\,\text{Å}$. The central wavelengths were chosen to ensure that features of interest were placed near the centre of the detector, $8200\,\text{Å}$ for the Na I doublet and $6560\,\text{Å}$ for Hα. A summary of our observations is shown in Table 3.2.

Each observing night included at least two standard stars in order to enable flux calibration and the removal of telluric features. These standard stars are listed in Table 3.1. All of the spectra were optimally extracted and reduced using the PAMELA and MOLLY reduction software, (Marsh, 1989b). Our comparison stars were chosen from early-type main sequence stars and white dwarfs since their spectra have few features in the $7500 - 8700\,\text{Å}$ region. We fitted splines to the continua of our comparison stars, avoiding regions of atmospheric absorption from 7560 to $7690\,\text{Å}$ and 8100 to $8400\,\text{Å}$. The ratio of the fit to the original spectrum was then used to correct for the absorption in the target spectra (see e.g. Marsh, 1990). The calibration star with the nearest air-mass was used and the correction was scaled by the ratio of the airmasses to the power 0.55 to account for the saturated absorption bands. The removal of these significant telluric features was not always adequate and this meant that some spectra could not be used for radial velocity fits as the Na I features were not visible after this correction.

For wavelength calibration, Cu+Ne and Cu+Ar arcs were observed several times over the course of the observations. This was then further improved by examining sky emission features in each of the science and calibration spectra and calculating the final wavelength shift required to assign these features to their known wavelengths. The sky emission lines used were the oxygen emission features at 7913.7 and $8344.6\,\text{Å}$.

3.3 Analysis

Radial velocities for all spectra were calculated by least-squares fits of a double-Gaussian function to the data near the Na I doublet at $8190\,\text{Å}$. The separation of the doublet was kept fixed at the laboratory value of $11.5\,\text{Å}$; the depth of the lines were free to vary but kept equal to each other, and the width of the lines was fixed to a FWHM of $2.4\,\text{Å}$. One of the targets, WD 1001+203, showed consistently broad lines on all of the spectra, so for this object, a larger width of $4.7\,\text{Å}$ was used. The uncertainties of the fit parameters were taken from the co-variance matrix produced

Table 3.2: The targets observed during the campaign. The coordinates are in epoch J2000. Spectra were deemed unusable if we were unable to fit a profile to the Na I or Hα feature. For all targets the Na I doublet at 8190 Å was observed, with the exception of WD 2257+162, where we observed the Hα emission from the secondary.

| WD | RA | Dec | # Spectra | # Usable |
	(h m s)	(° ′ ″)	taken	spectra
0023+388	00 26 33.2	+39 09 03	21	15
0303−007	03 06 07.1	−00 31 14	31	31
0354+463	03 58 17.1	+46 28 41	57	46
0430+136	04 33 10.3	+13 45 17	30	29
0752−146	07 55 08.9	−14 45 53	30	20
0812+478	08 15 48.9	+47 40 39	16	16
0908+226	09 11 43.1	+22 27 49	26	23
1001+203	10 04 04.2	+20 09 23	22	22
1037+512	10 40 16.8	+50 56 47	22	22
1051+516	10 54 21.9	+51 22 54	22	22
1133+358	11 35 42.7	+35 34 24	19	19
1333+487	13 36 01.7	+48 28 45	17	8
1339+606	13 41 00.0	+60 26 10	20	12
1433+538	14 34 43.1	+53 35 25	26	22
1436−216	14 39 12.8	−21 50 12	32	32
1458+171	15 00 19.4	+16 59 16	18	10
1504+546	15 06 05.3	+54 28 19	39	39
1517+502	15 19 05.9	+50 07 03	22	0
2257+162	22 59 46.9	+16 29 17	16	14
2317+268	23 20 04.1	+25 52 21	12	11

in the Levenberg-Marquardt procedure. The fitted wavelengths were then converted to radial velocities by calculating the shift to the rest wavelength for the blue-ward line of the doublet, 8183.3 Å.

For the target WD 2257+162, it was noted that previous observations had been unable to detect the Na I doublet, (Liebert et al., 2005; Tremblay and Bergeron, 2007), and therefore spectra centred on the Hα line were taken. Two overlapping Gaussian functions, one representing the emission profile and a second for the absorption profile were fitted. Radial velocities were derived by comparing the wavelength to the rest wavelength of Hα. While the fit to the emission gave errors of about 10 km s^{-1}, similar to measurements of the Na I doublet for the other targets, the absorption feature was too broad to allow the determination of the radial velocity of the white dwarf. A sample of the measured radial velocities for all of the targets is listed in Table 3.3, but, since the full table contains 416 rows, the full version is available in VizieR as catalogue J/MNRAS/484/5362.

3.3.1 Binary periods

In order to identify which of the targets exhibited radial velocity variability we used a test described in Maxted et al. (2008), where we calculate the probability, p of obtaining the computed χ^2 value compared to that computed from a sample of measurements distributed normally around the mean radial velocity. We set the criterion for radial velocity detection to $\log(p) < -4$. The three targets that did not meet this criterion were WD 0430+221, WD 0812+478, and WD 1001+203. We were unable to detect any Na I absorption lines in our spectra of WD 1517+302 and therefore could not deduce any radial velocity variability for this system.

Periods were derived by fitting a sine wave plus a constant to the data, and choosing the frequency that corresponded to the lowest χ^2. Our algorithm used the floating mean periodogram approach (Cumming et al., 1999). The key point in this method is that the constant systemic velocity is fitted at the same time as semi-amplitude and phase. This corrects a failing of the well-known Lomb-Scargle (Lomb, 1976; Scargle, 1982) periodogram which starts by subtracting the mean of the data and then fits a plain sinusoid and this is incorrect for small numbers of points.

The data sampling that occurred as a result of our observing strategy, i.e. taking a spectrum once or twice per night during a week long run, means that we were susceptible to aliasing, especially at multiples of 1 d^{-1}. We also had long gaps of several months between observing runs, which caused a fine-splitting of the 1 d aliases. Although it is certain that the radial velocities measured are due to orbital

Table 3.3: The measured radial velocities of our targets from a fit of a double-Gaussian to the Na I doublet at 8190Å. This table is abridged. The full version, containing the data for all of the 20 targets, is available in VizieR as catalogue J/MNRAS/484/5362.

WD	HJD	Radial velocity $(\mathrm{km\,s^{-1}})$	Error $(\mathrm{km\,s^{-1}})$
0023+388	2457066.347907	−28.5	0.8
0023+388	2457066.358477	−27.2	0.9
0023+388	2457269.503428	87.3	5.1
0023+388	2457269.510507	85.0	6.2
0023+388	2457270.542192	−166.8	3.9
0023+388	2457270.549273	−168.9	3.5
0023+388	2457271.597316	76.7	3.9
0023+388	2457271.604397	71.1	4.0
0023+388	2457272.511428	−154.5	3.9
0023+388	2457272.518510	−171.0	4.9
0023+388	2457273.500880	82.6	4.8
0023+388	2457273.507961	99.8	4.8
0023+388	2457274.493951	−115.5	8.4
0023+388	2457274.501032	−114.2	5.7
0023+388	2457432.344926	−69.2	10.4
0023+388	2457432.352005	−80.5	11.1
0023+388	2458298.655991	120.5	7.6
0023+388	2458298.663180	140.3	6.6
0023+388	2458298.677734	128.8	7.4
0303−007	2457066.373914	137.3	3.4
0303−007	2457066.384616	136.0	2.8
0303−007	2457067.339107	39.7	2.0
0303−007	2457067.349969	52.1	2.1
0303−007	2457068.350021	−73.0	2.2
0303−007	2457070.350993	−47.9	3.5
0303−007	2457070.361546	−65.9	3.2
0303−007	2457071.350476	50.6	3.5
0303−007	2457071.361029	26.1	4.7
0303−007	2457269.608182	−113.8	5.0
0303−007	2457269.615262	−121.9	4.5
0303−007	2457270.602259	−105.6	2.6
0303−007	2457270.609340	−112.5	2.5
0303−007	2457271.634996	−61.6	2.8
0303−007	2457271.642077	−73.7	3.0
0303−007	2457272.580913	124.4	2.4
0303−007	2457272.587994	123.9	2.2
0303−007	2457272.710581	−13.5	2.4
0303−007	2457272.717661	−23.9	2.1
0303−007	2457273.586402	118.5	2.9
0303−007	2457273.593485	133.0	2.7

Table 3.4: Fitted periods and aliases shown with the corresponding reduced χ^2 value. For each target, the number of valid radial velocity measurements N used in the analysis is also shown. We show the next best competing alias along with the associated increase in χ^2. Objects marked with an asterisk (*) showed no significant radial velocity variation.

WD	N	$P_{\rm orb}$ (d)	$\chi^2_{\rm red}$	2nd best alias (d)	$\Delta\chi^2$
0023+388	19	0.64159(1)	1.2	0.68339(1)	12
0303−007	31	0.54113(1)	1.0	1.19096(4)	135
0354+463	46	0.165203(1)	1.0	0.246896(2)	154
0430+136*	30	0.135480(7)	0.2	0.119120(6)	0
0752−146	21	1.05241(3)	1.0	0.522410(5)	15
0812+478*	16	0.055373(1)	0.2	0.7141(2)	0
0908+226	22	9.1614(8)	0.5	9.393(8)	2
1001+203*	22	0.26579(2)	0.2	0.20913(2)	0
1037+512	26	0.141460(1)	0.5	0.165146(2)	1
1051+516	22	2.770208(3)	0.5	0.73322(2)	16
1133+358	18	5.956(2)	0.0	6.055(2)	0
1333+487	11	1.75584(2)	0.0	2.27544(7)	1
1339+606	17	0.49367(1)	0.4	0.247534(4)	0
1433+538	22	4.479(3)	0.4	4.357(2)	0
1436−216	32	2.01774(2)	0.4	0.66988(4)	5
1458+171	10	0.0793902(3)	1.5	0.164702(1)	5
1504+546	36	0.93072(2)	1.0	0.479524(5)	128
2257+162	15	0.3223(1)	0.7	0.4736(5)	21
2317+268	10	0.7944(9)	1.0	3.85(5)	0

motion and also that the periods are relatively short (on the order of days), in some cases there are several competing aliases. Table 3.4 lists the best period and the most significant competing alias. Fig. 3.1 shows the fitted radial velocity plots and periodograms for all 19 of the objects that had fitted radial velocity data. This figure also includes the three targets, WD 0430+136, WD 0812+478, and WD 1001+203 that failed the radial velocity variability test but are shown here for completeness.

Once the best frequency had been identified, it was used as a starting point for a least-squares fit of a sine wave to the data of the following form,

$$v_{\rm r} = \gamma_2 + K_2 \sin\left[\frac{2\pi(t - t_0)}{P_{\rm orb}}\right], \tag{3.1}$$

where the initial guess for $P_{\rm orb}$ was $1/f$ and f is the frequency at the lowest χ^2 on the periodogram and allowed to vary in the fit, γ_2 is the systemic velocity of the secondary star, t_0 is the zero point defined by the inferior conjunction of the
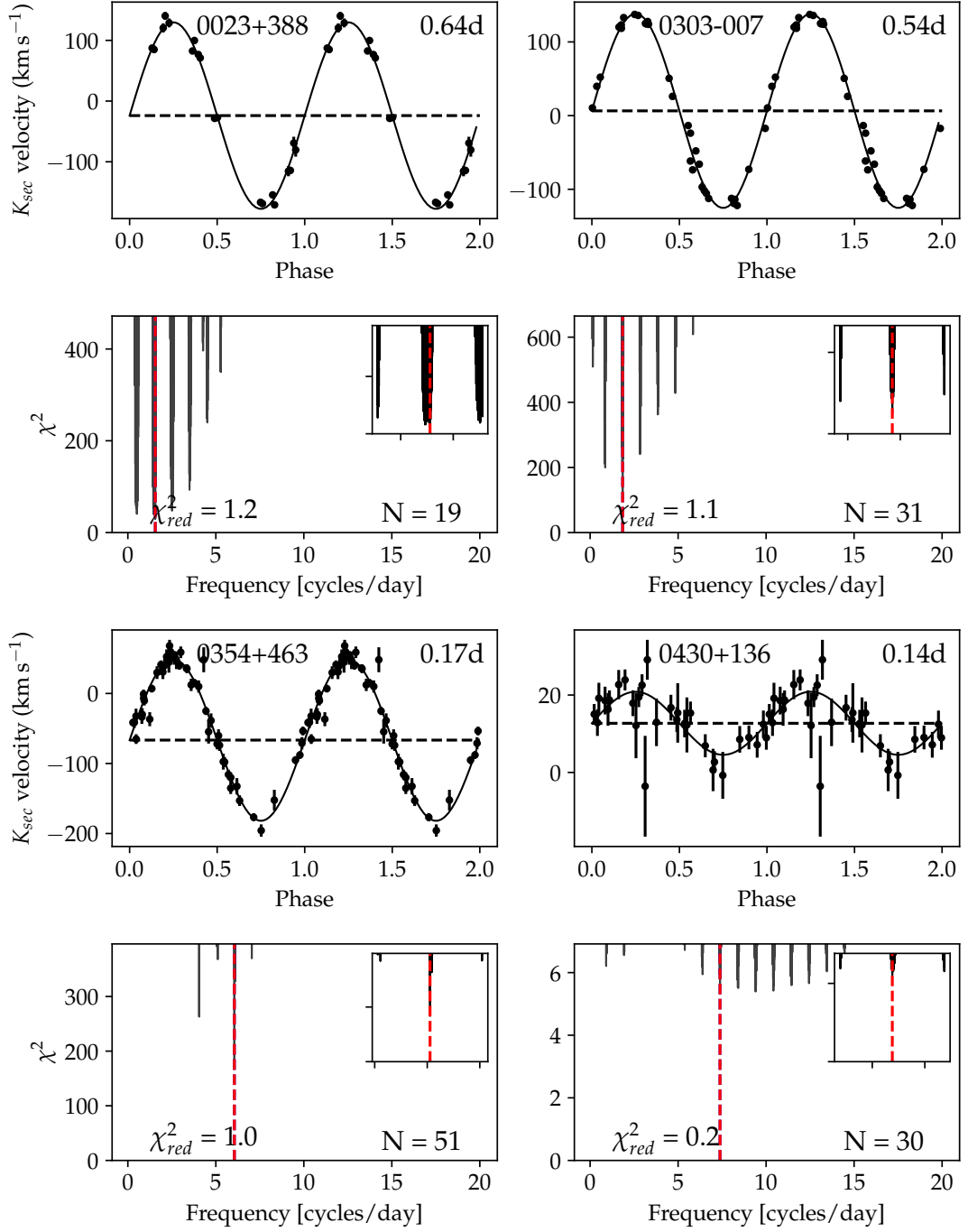
Figure 3.1: Plot of the 19 radial velocity fits. For each object depicted, the upper plot shows the radial velocity in $\mathrm{km\,s^{-1}}$ as a function of phase and the lower plot shows the χ^2 (after fitting a sinusoid plus a constant to the data) as a function of frequency. The vertical red line on the periodograms is the frequency chosen as the best fit and the period used for the folded radial velocity curve is derived from this. The insets to the periodograms show a zoomed in region near the best fit period, spanning a region of $\pm 10\%$ around the chosen frequency.
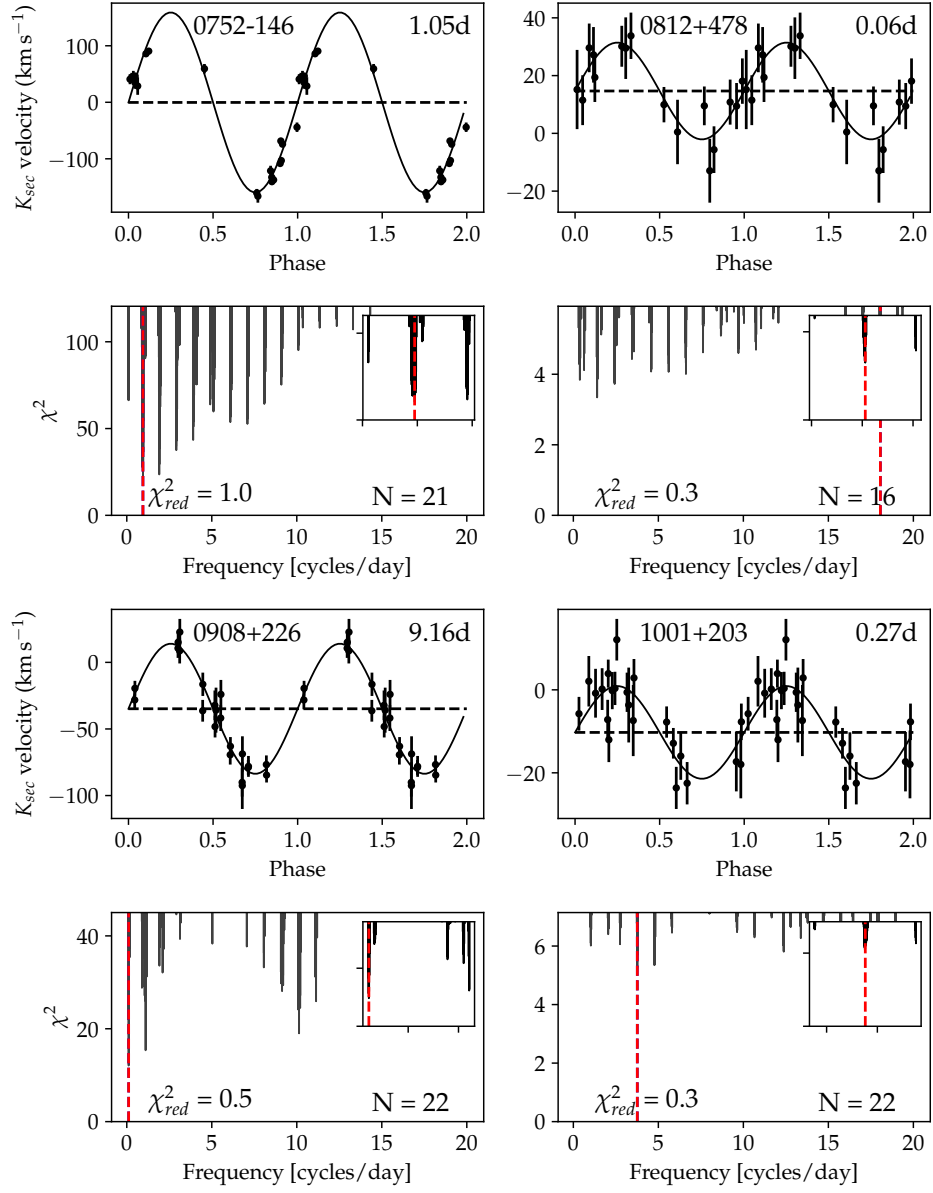
Figure 3.1: continued.
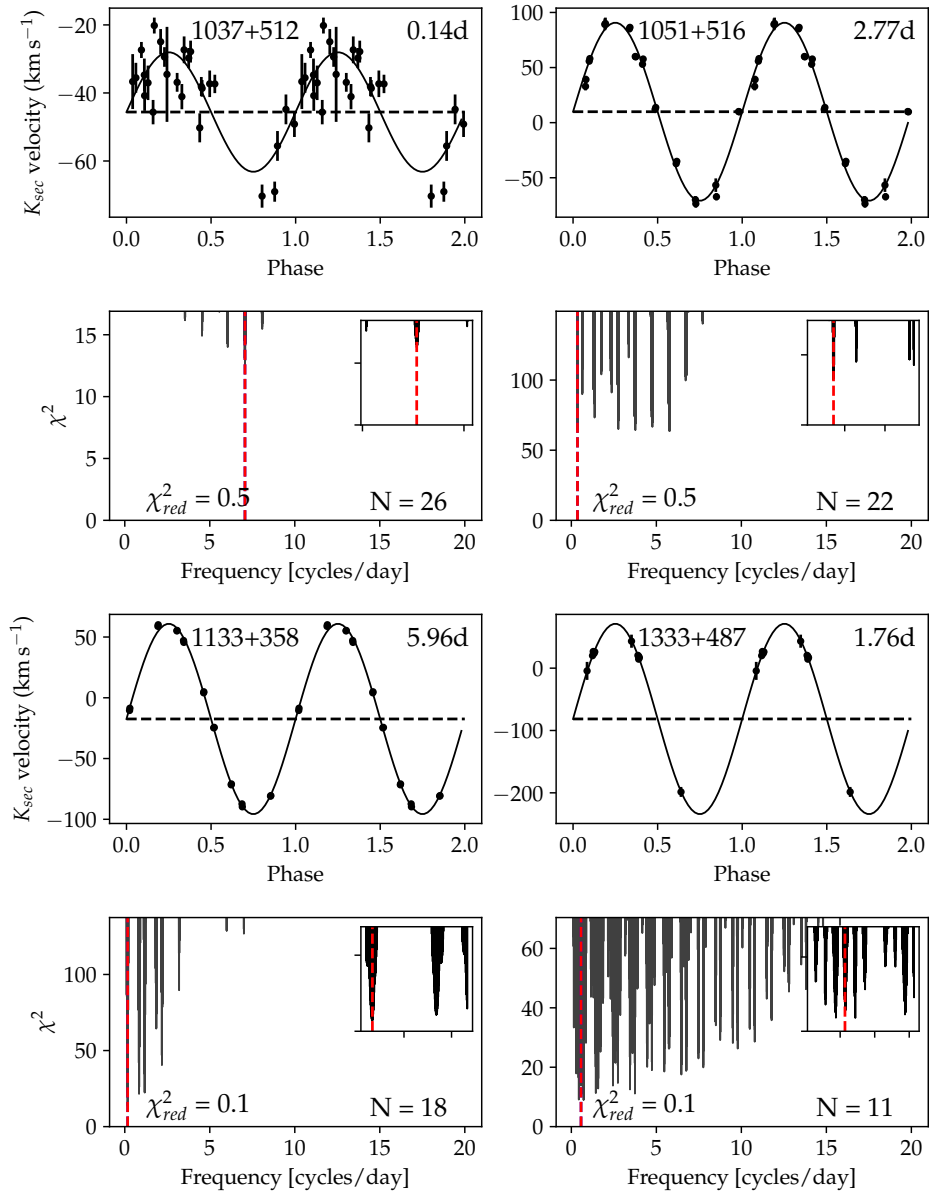
Figure 3.1: continued.
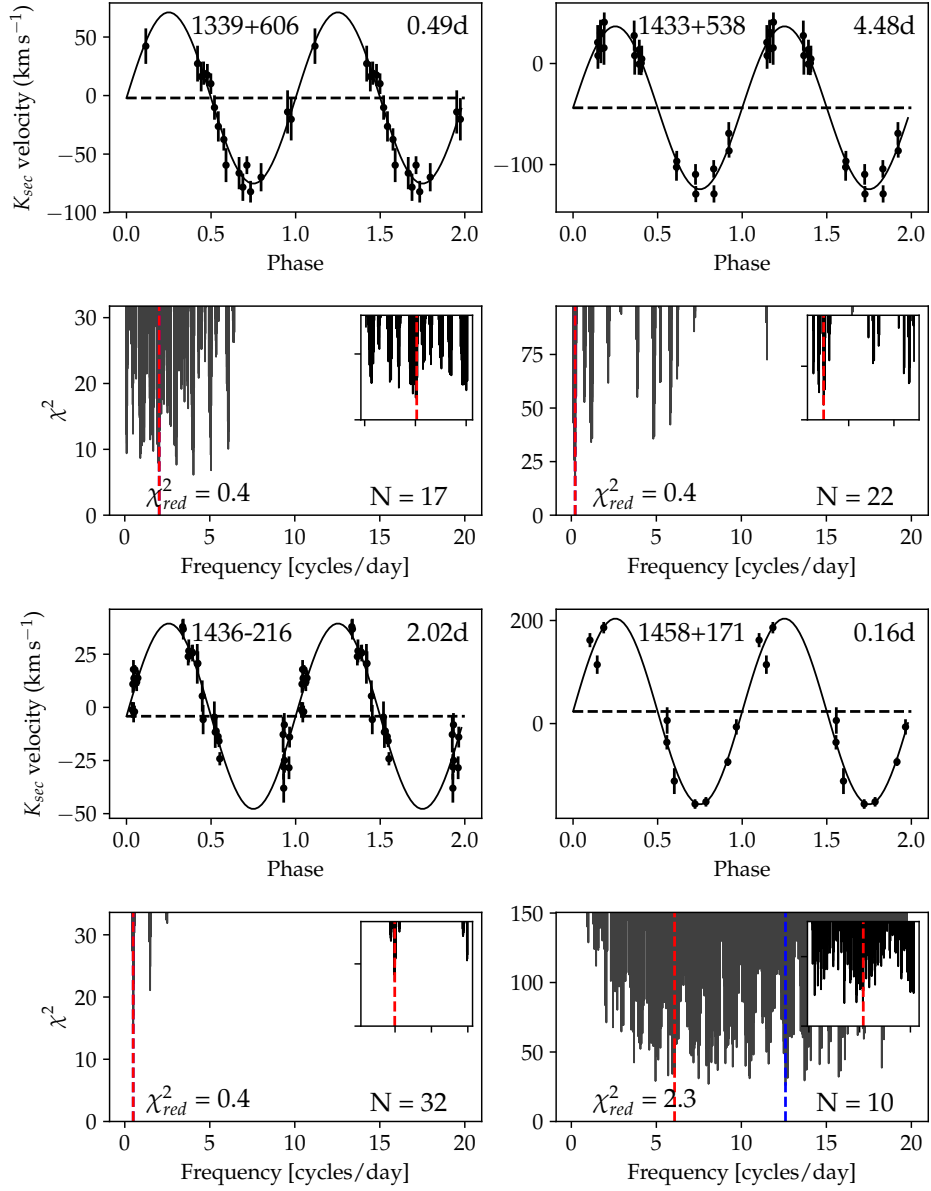
Figure 3.1: continued. A blue vertical line is shown where we found a second competing alias has a good chance of being the true period. See notes on individual objects for a discussion.
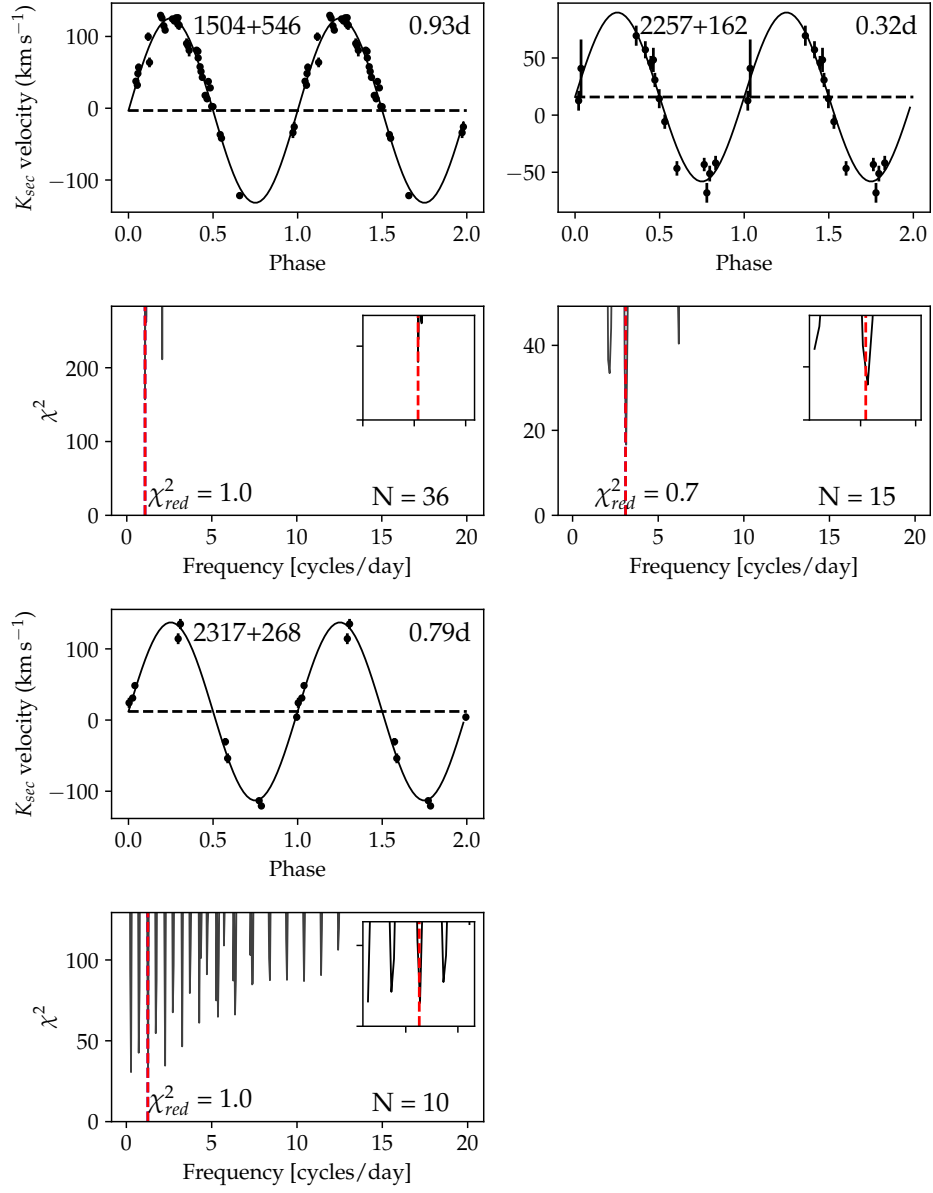
Figure 3.1: continued.

secondary star, and K_2 is the radial velocity semi-amplitude of the secondary star.

Fig. 3.1 shows the reduced χ^2 value for each of the fitted radial velocity curves. Several systems showed clear signs of extra noise, with minimum χ^2 values much larger than the number of degrees of freedom. Spectra that did not result in an adequate fit of the Gaussian (no solution found, or one with errors larger than the fit parameters themselves) were examined for signs of problems, and the conclusion drawn was that the most likely cause was residual and/or poorly corrected telluric absorption. Non-uniform filling of the spectrograph slit could have also been a contributing factor. In order to account for this extra source of noise, a fixed value was added, in quadrature, to all uncertainties to make the reduced χ^2 equal to unity for each fit. The typical value added to the uncertainties was 7–10 $\mathrm{km\,s^{-1}}$. This corresponds to about one third of a pixel in the spectrograph dispersion. Experience shows that this is a little larger than typical fluctuations caused by non-uniform slit illumination, hence we suspect that telluric correction is the more significant issue. Although this noise reduces the precision of our data, the radial velocity signal in most of our targets leaves no doubt as to the reality of the variations. In some cases, most notably, WD 1133+358 and WD 1333+487, it is clear that adding this systematic error over-compensated and resulted in a reduced χ^2 close to zero. For these targets, a systematic error closer to 2 $\mathrm{km\,s^{-1}}$ would have been more appropriate.

For all targets, the χ^2 value for the second best alias was also calculated. These values are listed in Table 3.4. It can be shown that the probability of a given period being the correct one in a Bayesian sense scales as $e^{-\chi^2/2}$ (Marsh et al., 1995a; Morales-Rueda et al., 2003). This means that for large values of $\Delta\chi^2$ we can be sure of our period, but for values of $\Delta\chi^2 < 5$ there is a significant chance of the correct period being one of the other aliases. Examination of Table 3.4 indicates that, while we can be sure that WD 0908+226, WD 1037+512, WD 1133+358, WD 1333+487, WD 1339+606, WD 1433+53, and WD 2317+268 exhibit radial velocity variability, we have not determined the true period with a high level of confidence.

Table 3.5 lists the derived periods for all of the objects. The measured periods have a range from 3.4 h to 9.2 d. Since there are only 16 periods in our sample, it was difficult to fit a Gaussian to the period distribution but we estimate a median value of $\log P_{\mathrm{orb}}\,(\mathrm{d}) = -0.2$ or $P = 0.6$ d, see Fig. 3.2.

In a similar study of systems selected from the Sloan Digital Sky Survey (SDSS) undertaken by Nebot Gómez-Morán et al. (2011), it was found that the periods range from 1.97 h to 4.35 d, and approximately follow a normal distribution in $\log P_{\mathrm{orb}}$ with a peak centred on $P_{\mathrm{orb}} = 8.1$ h or $P_{\mathrm{orb}} = 0.34$ d, Fig. 3.2 and 3.3

Table 3.5: Parameters for the binaries determined from the radial velocity study. The period, K_2 and γ_2 velocities are from this paper, the secondary estimated spectral type is taken from Farihi et al. (2010), and the T_{eff} has been retrieved from the Montreal White Dwarf Database (Dufour et al., 2017).

WD	P_{orb} (d)	K_2 $(\mathrm{km\,s^{-1}})$	γ_2 $(\mathrm{km\,s^{-1}})$	SpType	T_{eff} (K)
0023+388	0.64159(1)	153(4)	−24(3)	DA+dM5.5	10 980
0303−007	0.54113(1)	132(3)	6(2)	DA+dM4	20 310
0354+463	0.165203(1)	115(3)	−67(2)	DA+dM7	8 230
0430+136				DA+dM5.5	34 210
0752−146	1.05241(3)	159(10)	0(13)	DA+dM6	19 440
0812+478				DA+dM4	62 000
0908+226	9.1614(8)	48(4)	−35(4)	DA+dM3	10 548
1001+203				DA+dM2.5	21 010
1037+512	0.141460(1)	18(4)	−46(3)	DA+dM4	19 780
1051+516	2.770208(3)	81(3)	10(2)	DA+dM3	23 863
1133+358	5.956(2)	78(3)	−17(3)	DC+dM4.5	6 500
1333+487	1.75584(2)	153(9)	−81(9)	DB+dM6.5	14 676
1339+606	0.49367(1)	73(9)	−2(6)	DA+dM3.5	44 770
1433+538	4.479(3)	81(4)	−44(3)	DA+dM4.5	23 260
1436−216	2.01774(2)	44(10)	−4(2)	DA+dM2.5	23 690
1458+171	0.164702(1)	180(8)	23(6)	DA+dM4.5	22 600
1504+546	0.93072(2)	129(4)	−3(3)	DA+dM3	23 120
1517+502				DA+dC	31 270
2257+162	0.3223(1)	74(7)	16(5)	DA+dM4.5	25 450
2317+268	0.7941(2)	125(6)	12(4)	DA+dM3.5	31 890
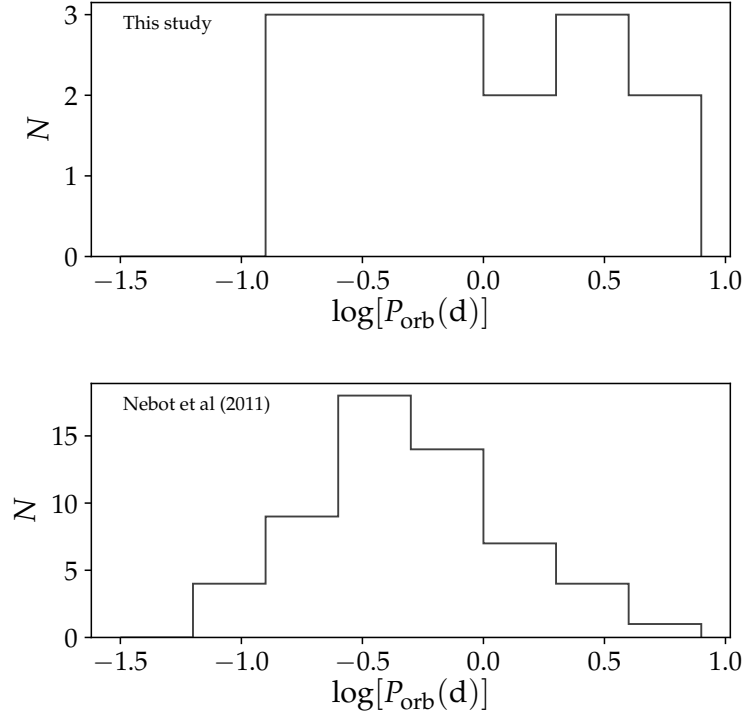
Figure 3.2: The orbital period distribution of the 16 PCEBs contained in this study compared to that of the 79 PCEBs characterised by Nebot Gómez-Morán et al. (2011).

show a comparison between that sample and this one. Their study had 79 targets, while this only contains 16 with determined periods. We performed an Anderson-Darling test (Scholz and Stephens, 1987) on the two samples to check if they can be considered as being derived from the same underlying population distribution. This test is favoured over the The results of this test suggest that we cannot reject the null hypothesis i.e. that the two populations are not selected from the same underlying distribution at a 10 per cent level. The Anderson-Darling test was chosen over the more conventional choice of the Kolmogorov–Smirnov (or KS) test as it is more sensitive to the deviations from the underlying distribution at the edges of this distribution (Stephens, 1974).

We also performed an Anderson-Darling test on our sample against the predicted population distribution in Willems and Kolb (2004). The cumulative distribution function is shown in Fig. 3.4. In this case the result suggests we can reject the null hypothesis at a 1 per cent level. From this we can conclude that our population does not match the distribution proposed in their BPS and has a peak in period distribution at a shorter duration as can be seen in Fig. 3.4. It should be noted
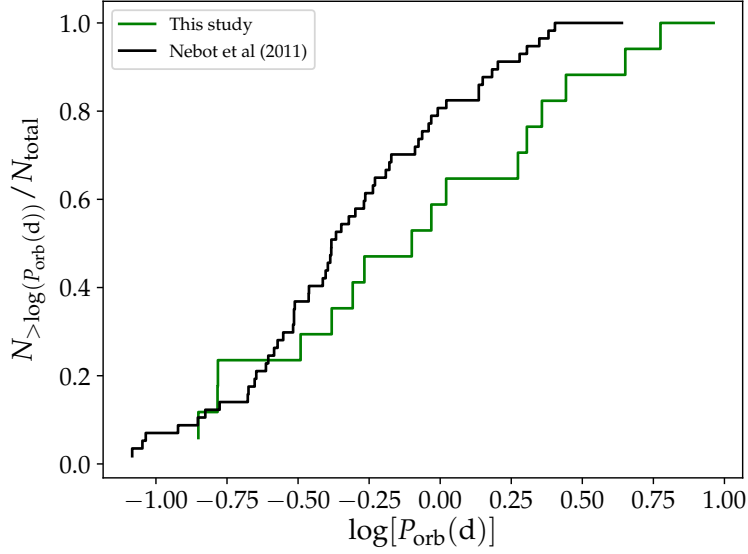
Figure 3.3: Comparison of the cumulative period distribution of this study and the period distribution of 79 PCEBs selected from SDSS by Nebot Gómez-Morán et al. (2011).

that the Willems-Kolb study, adopted a value of $\alpha_{CE} = 1$. In a more recent study, Davis et al. (2010) produced population distributions for two additional values of $\alpha_{CE} = 0.1$ and 0.6. They find that for low mass secondaries (as per our sample) the theoretical period distribution peaks at $\log P_{orb}$ (d) ≈ -0.5 which is near to our peak at $\log P_{orb}$ (d) ≈ -0.2. They also show that increasing the value of α_{CE} has the effect of moving the overall period distribution to longer periods (see their Table 2). Davis et al. (2010) conclude that a value of $\alpha_{CE} = 0.1$ will predict the observed peak in period distribution, but the distribution will also include a long tail at longer periods going out to hundreds of days. Binaries with such a long period have not yet been observed among PCEB systems and this includes those in the present study.

Camacho et al. (2014) show that for the PCEBs selected from SDSS, small values for the common envelope efficiency ($\alpha_{CE} < 0.3$) in simulated populations predict the observed period distribution. Our study, though limited in sample size, agrees with these modelled values of α_{CE}.

In the *HST* imaging survey of Farihi et al. (2010), 72 of the 90 targets were confirmed to be WD+MS binaries with the remaining stars deemed to be non-binary. Of the binaries, 43 were resolved with ACS HRC imaging, implying separations wider than at least a few au. The remaining 29 were unresolved with *HST*. We obtained spectroscopy for 20 of the unresolved pairs, of which 16 were
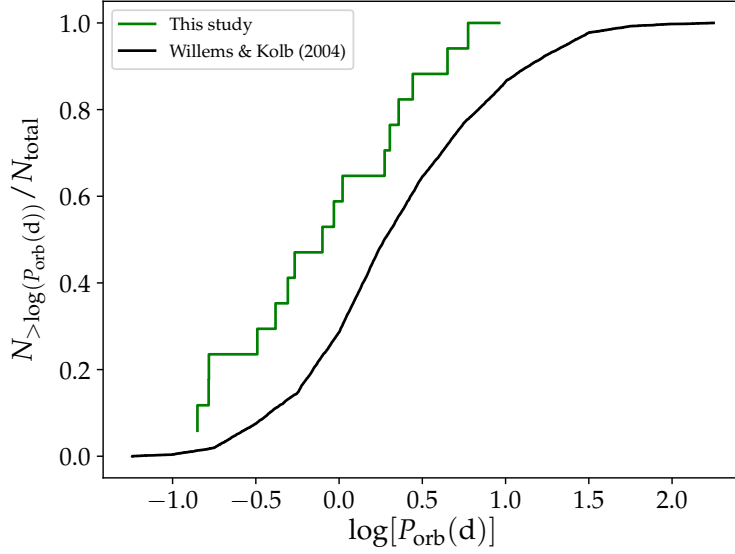
Figure 3.4: Comparison of the cumulative period distribution with a synthetic sample generated from the probability distribution for PCEB periods described in Willems and Kolb (2004). The Anderson-Darling test suggests the null hypothesis cannot be rejected at a 99 per cent confidence level.

confirmed as short-period ($\sim$ hours to days) systems that underwent a common envelope phase. Thus overall, about 60 per cent of the binaries have wide orbits and 34 per cent are in close orbits with the remaining 6 per cent not determined.

Nebot Gómez-Morán et al. (2011) calculated a 23 ± 2 per cent PCEB fraction for WD+MS systems found in SDSS, with an upper limit, after taking selection effects into account, of 27 per cent. In our smaller sample, we obtain a PCEB fraction of 34 per cent, but our sample is biased as it excluded targets that were spatially resolved in ground-based images. Accounting for the fact that spatially-resolved binaries are 63% of the population when viewed from the ground (Farihi et al., 2006), the PCEB fraction of this study reduces to 22 per cent, and is similar to the 23 per cent of Nebot Gómez-Morán et al. (2011).

While the difference between the results from this study and that of Nebot Gómez-Morán et al. (2011) are not statistically significant, it is noted that there is a tendency for slightly longer periods here. Zorotovic et al. (2011b) find evidence of a trend towards longer periods for PCEBs with an earlier secondary. Comparison of the secondary spectral types between the Nebot study and this one indicate that there is no discernible difference with both distributions having a median value of approximately M4. Therefore, although this study hints at confirmation of this relationship between secondary spectral type and period, we cannot confirm it con-

Table 3.6: Resulting separation statistics for the sub-samples of the 90 WD+MS binary candidates from Farihi et al. (2006), classified by separation.

Type	Number	Fraction
Candidates	90	
Confirmed as binary	72	100%
Resolved with *HST* (3 – 1000 au)	43	60%
Unresolved ($\lesssim 10$ au)	29	40%
Included in this study	20	100%
Confirmed as short period ($\lesssim 10$ au)	17	85%
Number with confirmed periods	16	
Short period suspected, but no solution	1	
Undetected radial velocity variability	3	15%

clusively.

3.3.2 Observational constraints

In order to understand the effects of our experimental approach in terms of instrument sensitivity and measurement cadence, we performed a Monte-Carlo simulation on a synthetic sample of input period distributions. For each period in our input sample we assumed a random orientation for the inclination of the system with a distribution that is flat in $\cos(i)$. We then calculated a K_2 amplitude using the mass function,

$$\frac{(M_1 \sin(i))^3}{(M_1 + M_2)^2} = \frac{P_{\mathrm{orb}} K_2^3}{2\pi G}, \tag{3.2}$$

where G is the gravitational constant. For the masses of the binaries we assumed values of $M_1 = 0.6 \mathrm{M_\odot}$ and $M_2 = 0.2 \mathrm{M_\odot}$ for all of the objects in the simulation. We randomly selected an HJD based on the actual observing dates and times and computed the simulated observed K_2 velocity. We used 15 $\mathrm{km\,s^{-1}}$ as the limit on the standard deviation of the simulated velocities to distinguish a detection of radial velocity variation. We repeated this test for 1000 input periods to deduce the detection probability as a function of orbital period. The input periods were selected from a random distribution of uniform probability for periods in the range $-2.0 \leq \log P_{\mathrm{orb}}(\mathrm{d}) \leq 2.0$. The results are shown in Fig. 3.5. We can be confident that our observing strategy will detect systems with periods ranging from 0.01 d to ≈ 10 d but the detection rate drops of markedly for periods greater than 30 d. In additional simulations we tweaked two factors; a) the observation baseline, by creating an artificially extended set of observation times and b) an improved observation error, by artificially reducing our measurement error on the wavelength of the spectral
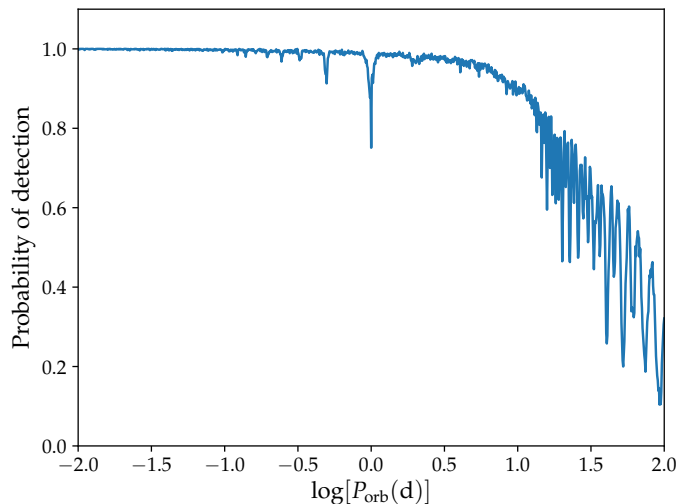
Figure 3.5: The detection probability of radial velocity variations for a simulated input population with periods following a flat distribution in $-2 \leq \log P_{\mathrm{orb}} \leq 2$. The detection is modelled on our actual observation times and instrument setup, as described in the text.

features. The former simulation did not lead to improvement in the detect-ability of longer period systems, but the latter significantly improved the chances of finding radial velocities for systems with periods longer than 10 d. From this we can conclude that our observational setup is limited by the grating resolution and the signal to noise (S/N) of our targets at the telescope and not the time baseline of our observations.

The three objects that showed no detectable radial velocity variations could have periods that fall into the weeks to several years range and have escaped our detection regime at the INT. Our simulations suggest that improving our radial velocity sensitivity through higher S/N spectra and higher resolution gratings may allow us to detect periods in such systems.

3.3.3 Position on the HR diagram

With one exception (WD 0430+136), all of our targets have *Gaia* measured parallaxes in DR2 (Gaia Collaboration et al., 2018). Using these data, we are able to place the binaries on the HR diagram. All points lie between the white dwarf and main sequence as shown in Fig. 3.6. Some of the objects are at the extreme edges of this range and we discuss those in the following section.

In Fig. 3.6, the data used for indicating the overall population of the solar

neighbourhood were drawn from a random sample of 327,000 entries in DR2 that matched the quality criterion that the error on the measured parallax was at least 20 times smaller than the parallax value. To increase the visibility of the white dwarf sequence we supplemented the sample with a selected set of 14,000 white dwarfs drawn from DR2 by colour selection.

3.4   Notes on individual objects

0303-007. Phase folding the CRTS data to our radial velocity derived period, reveals a tentative increase in brightness by about 0.05 magnitude at phase 0.5 as shown in Fig. 3.7. This could be due to a small reflection effect on the secondary.

0354+463. Zuckerman et al. (2003) identify this target as containing a DAZ and report that the velocity of the Ca II K absorption in the white dwarf and the Hβ emission line in the M-dwarf agree reasonably well at -69.7 km s^{-1} and -67.7 km s^{-1} respectively. We measured a γ_2 velocity of -67 km s^{-1} using the Na I absorption in the secondary. The metal pollution of the white dwarf atmosphere is likely due to accretion from a stellar wind emanating from the secondary.

0430+136. This is a suspected triple, with one component resolved by *HST* and a second identified on the basis of I-band photometric excess at the location of the white dwarf (Farihi et al., 2010). We took 30 spectra of this target over a 1.2 year period and can see no obvious variability above our measurement errors. However, the two components resolved by HST are separated by $0''.26$ which is several times smaller than typical seeing at Roque de Los Muchachos. Thus, it is suspected that the Na I line detected in the INT spectra originates in the brighter, widely separated, red dwarf component. If this target is followed up, then it would be more prudent to search for radial velocity variations in the Hα emission expected from the illuminated surface of the fainter red dwarf that is closer to the white dwarf.

1133+358. This is a rare DC+dM binary (Farihi et al., 2010). The fact that the pair was unresolved with ACS implies a projected separation of less than 1.3 au. Assuming canonical mass values for both of the components an estimate for their separation is 0.06 au. The white dwarf in this system is likely to be accreting metals from the wind of the M-dwarf and this therefore makes it a good target for follow-up investigations looking for metal pollution.

1333+487. This was identified as a potential triple system by Farihi et al. (2010) and has a resolved red dwarf companion at a separation of 3 arcsec with the other component being an unresolved WD+MS binary. We have successfully deter-
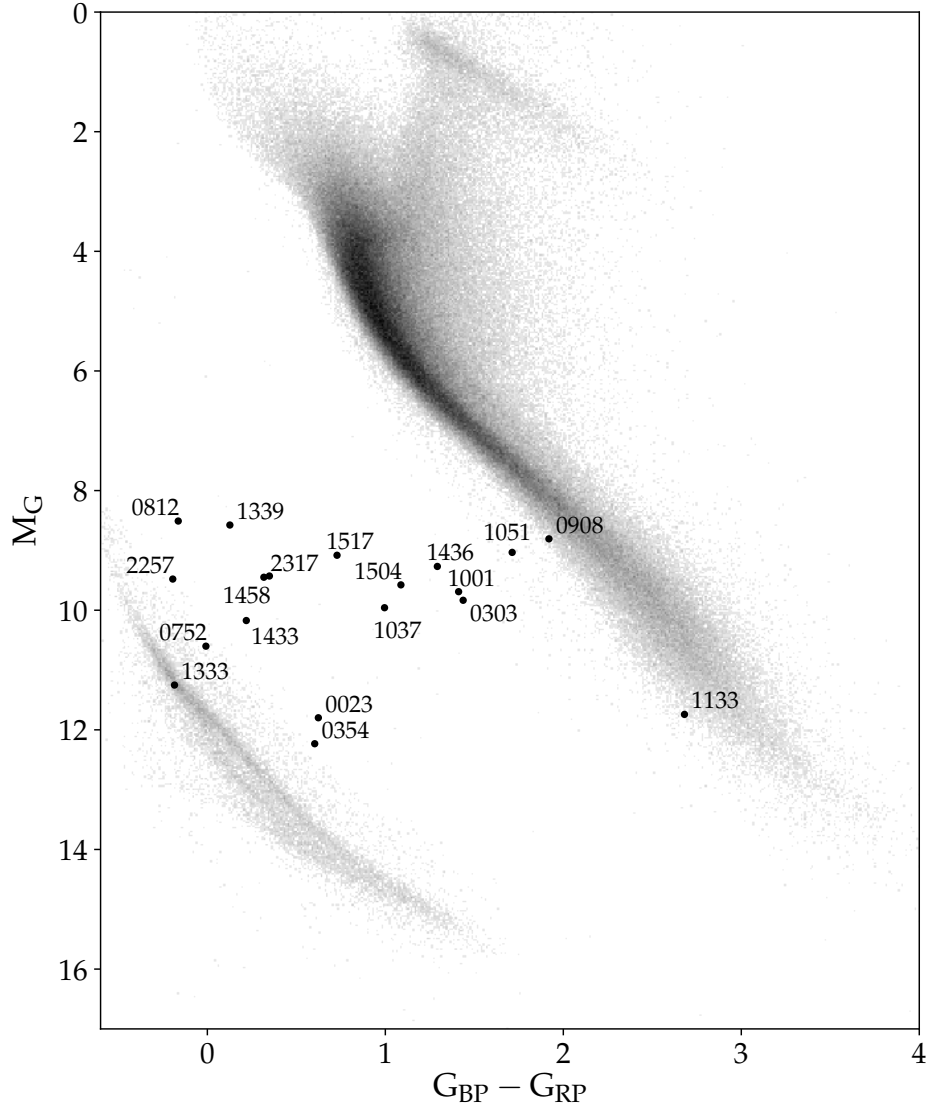
Figure 3.6: Colour-magnitude diagram showing the position of our objects relative to the white dwarf and main sequence. The only member of our sample that is not present in this diagram is WD 0430+136, which does not have a published parallax in *Gaia* DR2.
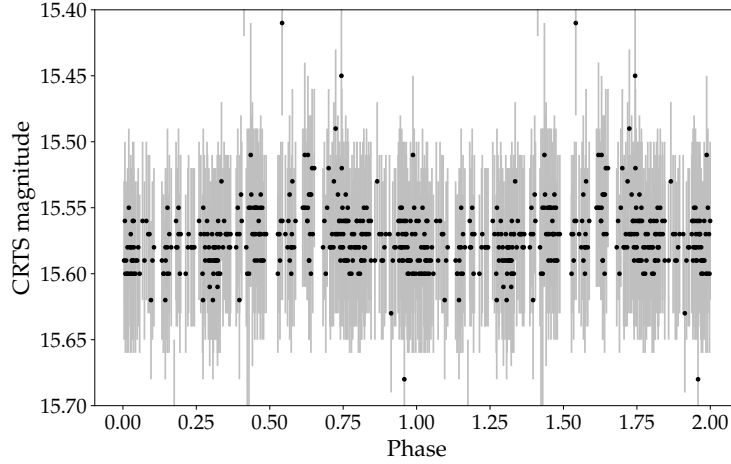
Figure 3.7: The phase-folded CRTS light-curve of WD 0303-007. At phase 0.5 there is a tentative detection of a reflection effect on the secondary.

mined the period of this binary in this study. During our observations, we also took three spectra of the resolved red dwarf. Two spectra were taken within 15 minutes of each other and have radial velocities of 16 ± 1 and $20\pm2\,\mathrm{km\,s^{-1}}$ respectively. The third spectrum was taken 4 days later and has a radial velocity of $0\pm1\,\mathrm{km\,s^{-1}}$. There is a possibility that this resolved component is also a binary. Follow-up observations of this object should include spectra of the resolved red dwarf component. The *Gaia* DR2 published proper motions and parallaxes for both components agree to the extent that they are a common proper motion pair, with the small differences explicable in terms of mutual orbital motion. Their parallaxes lead to a minimum separation of $\approx 110\,\mathrm{au}$.

1433+538. Although Schultz et al. (1996) noted that the Hα region was featureless during their observations, Farihi et al. (2010) remarked that close inspection of the SDSS spectrum showed some tentative evidence of Hα and Na I 8190 Å emission that may be due to noise. In this study, we did not find any evidence of emission.

1458+171. Nebot Gómez-Morán et al. (2011) identify this as a wide binary, based on two spectra taken on the same night approximately 15 min apart. Our Lomb-Scargle analysis has several competing aliases and the frequency for the minimum chi-squared value leads to a period of 0.079 d. The photometric data from the CRTS and the PTF surveys reveal a clear reflection effect on the secondary and a Lomb-Scargle analysis of these data leads to a best period of 0.164 d which is double the period of our minimum chi-squared analysis. We have used this longer
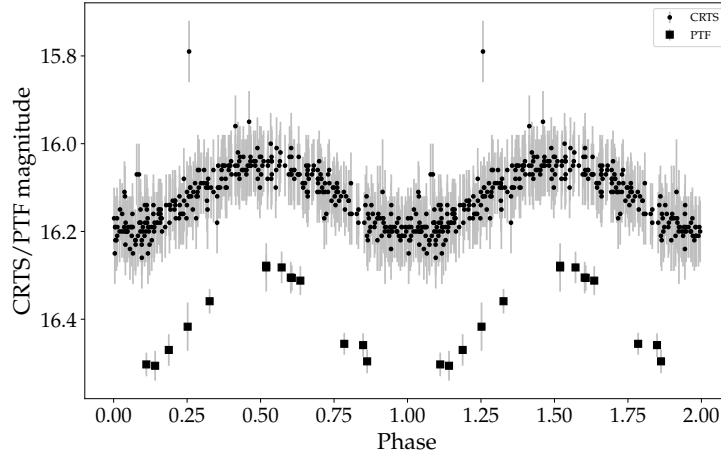
Figure 3.8: The phased-folded light-curve of WD 1458+171 with photometry taken from CRTS and PTF data. The modulation is attributed to a reflection effect on the secondary. PTF data points are shown with a square symbol and have not been offset from the CRTS data points. It should be noted that CRTS and PTF do not have the same pass band for their photometry.

period as our result. The white dwarf has a temperature of 22 000 K and with such a short period, a reflection effect is expected. Fig. 3.8 shows a phase folded plot of the CRTS and PTF data.

1504+546. The CRTS and PTF photometric data for this target is shown in Fig. 3.9. It is an eclipsing binary with a primary eclipse lasting 35 min. Although no secondary eclipse is visible there is a reflection effect caused by irradiation of the primary onto the inward facing hemisphere of the secondary.

Photometry of the primary eclipse for WD 1504+546 was obtained on the Liverpool telescope using the RISE camera with the RISE filter and is shown in Fig. 3.10. This displays a sharp ingress and egress of the white dwarf behind the secondary with a total eclipse time of 35.205 min. Approximate apparent magnitudes were calculated by comparing the flux counts with the published SDSS r band magnitude of a comparison star, SDSS J150618.53+542801.5 located 114 arcseconds to the east of the target. The RISE filter is a broad band $V + R$ filter (covering 5000 to 8000 Å) and so the apparent magnitude is approximate only.

1517+502. This system was discovered by Liebert et al. (1994) and is a DA white dwarf paired with a dwarf carbon (dC) star. Farihi et al. (2010) failed to resolve the components with the *HST* ACS imaging and set a minimum separation of about 20 au. Although Liebert et al. (1994) noted a weak Na I D feature at
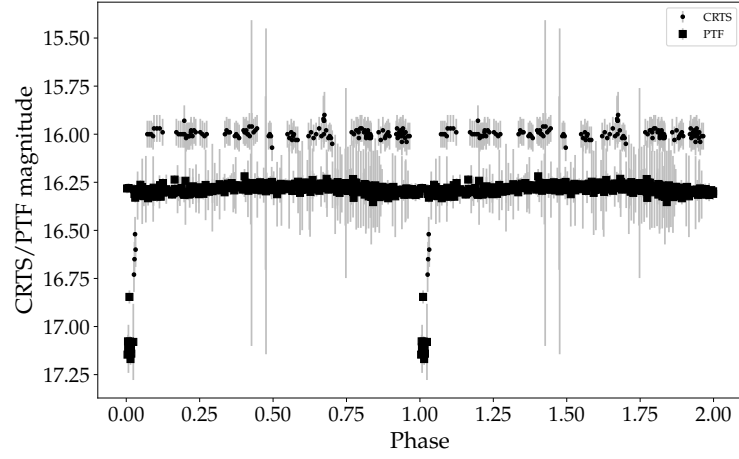
Figure 3.9: The phased-folded light-curve of WD 1504+546 with photometry taken from the PTF and CRTS surveys.
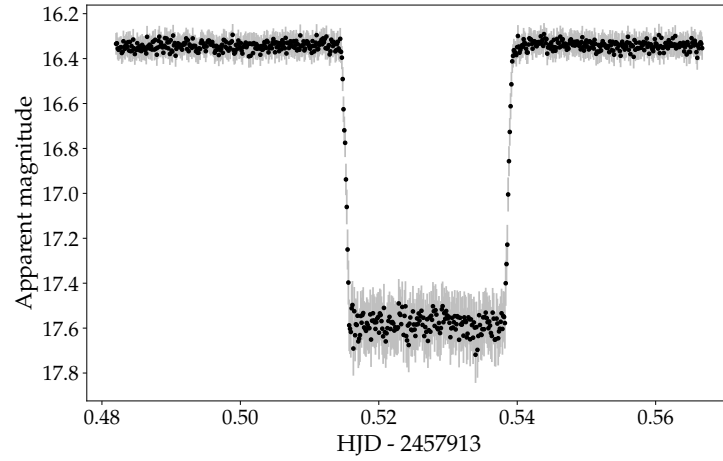
Figure 3.10: The Liverpool RISE camera light curve for the primary eclipse of WD 1504+546. Integration times were 2 s and the points plotted here were binned by a factor of 5.

5890 Å, and this is confirmed in the SDSS spectrum, our spectra did not show any Na I doublet at 8190 Å and we were unable to use our fitting method to determine radial velocities. The SDSS spectrum shows clear Hα emission and this feature might be used in future observations.

3.5 Conclusions

We have measured the orbital periods and their distribution for 16 WD+MS binaries identified as likely to be PCEB binaries in Farihi et al. (2010). The periods range from 0.14 to 9.16 d and the overall distribution is similar to that encountered in previous studies of such populations, such as Nebot Gómez-Morán et al. (2011). Our sample does not contain any system with a period longer than 9 d. The longest period in the Nebot Gómez-Morán et al. (2011) survey is 4.3 d while the longest known period in a PCEB is that of IK Peg at 21.72 d (Landsman, 1993). Three of our targets did not show significant radial velocity shifts. It is possible that these targets have periods of around 10 days and longer and therefore the radial velocity amplitudes that are too low to be detected by our particular instrument set up.

Combining the results of Farihi et al. (2010) and this study, we can confirm the bimodal nature of the period distribution of WD+MS binaries. Recent BPS models (Davis et al., 2010) predict a tail of PCEB periods longer than tens of days. Although we see a sharp reduction in the number of systems with these sorts of periods, we are not able to completely rule out the possibility of a small number of systems with periods in this regime.

When comparing our results to another observational study, Nebot Gómez-Morán et al. (2011), we find no statistical difference between our distributions. Our selection was made by selecting candidates from infrared excess in the 2MASS colours and the SDSS study selected candidates by examining spectra.

Overall, there is a discrepancy between the predicted and the observed period distributions of WD+MS binaries. The predicted distributions predict a longer tail of the group of WD+MS pairs that have been through the common envelope phase and this has not yet been observed in population surveys so far. One reason for this could be that BPS models take a simplified approach to the dynamics of the common envelope and, in particular, cannot model the full turbulent dynamics of this phase. Parameterised approaches to modelling the efficiency of the common envelope ejection, α_{CE} may not be adequate to predict the sharp cut-off in periods longer than 10°. Another explanation could lie with the observational approach. Our selection process was based on the detection of infra-red excess from sources already

identified as white dwarfs and although this approach does not lead to explicit biases related to the orbital period of such systems, there might be an implicit bias that poorly selected WD+MS systems that have intermediate periods. Analysis of our particular observing setup has also shown that we lack the sensitivity to ensure that we will positively detect all those systems with intermediate periods.

Chapter 4

V1460 Her

4.1 Introduction

As CVs evolve, their secondary stars continually lose mass and therefore need to adjust their structures to maintain thermal equilibrium. Whether they manage to do so depends upon the thermal timescale of the secondary star compared to the mass loss timescale, $M_2/(-\dot{M}_2)$. Both timescales tend to lengthen as orbital periods and secondary star masses decline, but at very low masses ($< 0.1\,\mathrm{M_\odot}$) and correspondingly short periods ($\simeq 80\,\mathrm{min}$), the battle to maintain thermal equilibrium is well and truly lost, resulting in a minimum orbital period for systems with hydrogen-rich donors (Paczynski and Sienkiewicz, 1981; Gänsicke et al., 2009). Until this point however, we expect the secondary stars to be fairly close to thermal equilibrium (although departure from thermal equilibrium is thought to be partly responsible for the paucity of systems in the period gap). The maintenance of near thermal equilibrium while losing mass, and the one-to-one relationship between orbital period and the mean density of Roche-lobe filling stars (Faulkner et al., 1972) results in a strong correlation between orbital period, mass and spectral type amongst CV donor stars (Knigge, 2006).

The discovery of K-type donor stars in the short-period CVs EI PSc and QZ Ser (Thorstensen et al., 2002a,b) forcefully demonstrated that alternative evolution channels also contribute to the population of CVs. Thorstensen et al. (2002a,b) argued that the over-luminous donors in EI PSc and QZ Ser were the stripped cores of companions that were initially more massive, $\gtrsim 1\,\mathrm{M_\odot}$, bearing the signatures of CNO burning in the form of enhanced sodium abundances. Anomalous carbon and nitrogen abundances were confirmed in EI PSc and QZ Ser both in the ultraviolet (Gänsicke et al., 2003) and infrared (Harrison, 2016). Sufficiently high initial donor

star masses, i.e. $M_2/M_1 \gtrsim 1$, lead to thermal-timescale mass transfer, with mass transfer rates that may result in stable shell burning on the white dwarf (Fujimoto, 1982; Iben, 1982; Wolf et al., 2013). During this shell-burning phase the systems will be luminous supersoft X-ray sources (van den Heuvel et al., 1992) and the white dwarf may grow in mass, making this evolutionary channel a potential single-degenerate pathway to type Ia supernovae (SN Ia) (Di Stefano, 2010). In many cases however, the rapid mass loss of the donor star results in such a decrease of the mass ratio that, failing to reach the ignition conditions for a thermonuclear supernova, the systems will blend into the population of normal CVs once $M_2/M_1 \lesssim 1$.

Whereas the physical properties of both stellar components of these "failed SN Ia" can, in the right circumstances, be accurately measured, providing a powerful diagnostic of this evolutionary pathway, only a relatively small number of such systems have so far been identified (e.g. Rodríguez-Gil et al., 2009; Thorstensen, 2015; Thorstensen et al., 2015; Yu et al., 2019). Here we report that the system V1460 Her is the newest member of this exclusive list of CVs.

On 2016 June 4, Drake (2016) reported that the Catalina Real-Time Transient Survey (CRTS) (Drake et al., 2014b) had detected an outburst of CRTS J162117.3+441254, an object that had previously been classified as a contact binary in the SuperWASP survey with a period of 0.207852 d (Lohr et al., 2013). Thorstensen (2016) obtained a full orbit of time-resolved spectroscopy, which showed strong Balmer emission lines, and measured the radial velocities of absorption features in anti-phase with the emission, confirming the binary nature of the target. It was clear that this was a cataclysmic variable undergoing a dwarf nova outburst. Kjurkchieva et al. (2017) took photometric data two weeks after the outburst and supplemented this with AAVSO observations to make a qualitative model of the system. This further confirmed that the system is a cataclysmic variable with an early-type donor. Kazarovets et al. (2019) designated this target with the General Catalogue of Variable Stars name of V1460 Her and classified it as an eclipsing dwarf nova.

In this chapter we present the results of extensive optical and ultraviolet spectroscopic and photometric follow-up of V1460 Her which we use to determine system parameters and the nature of its donor star. Serendipitously, our data also reveal rapid spin of its white dwarf. We begin with a description of our observations.

Table 4.1: Log of observations taken by the Warwick One Metre telescope (W1m). Data was taken immediately after the report of the 2016 June outburst of V1460 Her. For all nights, the same filter arrangement was used, BG40 + Z. One additional night was added during quiescence, 44 days later. The number N denotes the approximate number of orbits since the reported outburst.

Date	JD (start)	N (orbits)	T_{exp} (s)	Duration (hr)
2016/06/05	2457545.386138	21	30	5.68
2016/06/07	2457547.385385	30	30	4.33
2016/06/08	2457548.528484	36	30	4.63
2016/06/09	2457549.529722	40	30	4.52
2016/07/23	2457593.373344	251	30	5.39

4.2 Observations

Following the Astronomer's Telegram 9141 (Thorstensen, 2016) on 2016 June 5, we decided to take follow-up observations using the Warwick 1 metre (W1m) telescope on the island of La Palma. We maintained observations for several nights as the target evolved from outburst to quiescence. In addition, we submitted proposals for spectroscopic follow-up. The details of these two campaigns are summarised in the following sections. To supplement our own observations we looked at various other sources of photometry, including AAVSO, SuperWASP, ASAS-SN and CRTS.

4.2.1 Warwick One metre (W1m) photometry

We used the W1m telescope to perform follow-up observations of the 2016 June outburst. For four nights from the 2016 June 5 to the 2016 June 9, photometry of V1460 Her was taken with the intention of covering as much of a full orbit as possible. A log of observations is shown in Table 4.1. The W1m was undergoing a commissioning phase at the time and we used V1460 Her as a serendipitous test target for the development of the observation pipeline.

4.2.2 Published survey photometry

V1460 Her is present in the SuperWASP catalogue as 1SWASP J162117.36+441254.2. The full dataset from this archive covers the period from JD 2453827.587407 to 2454681.536435 (2006 April to 2008 August) and contains 36242 data points. Lohr et al. (2013) present a light curve and a period of 0.207852(1) d, classifying it as a contact binary of type W UMa. The SuperWASP data displayed in Fig. 4.1 show that V1460 Her had an outburst in 2006 August (JD 2453952).
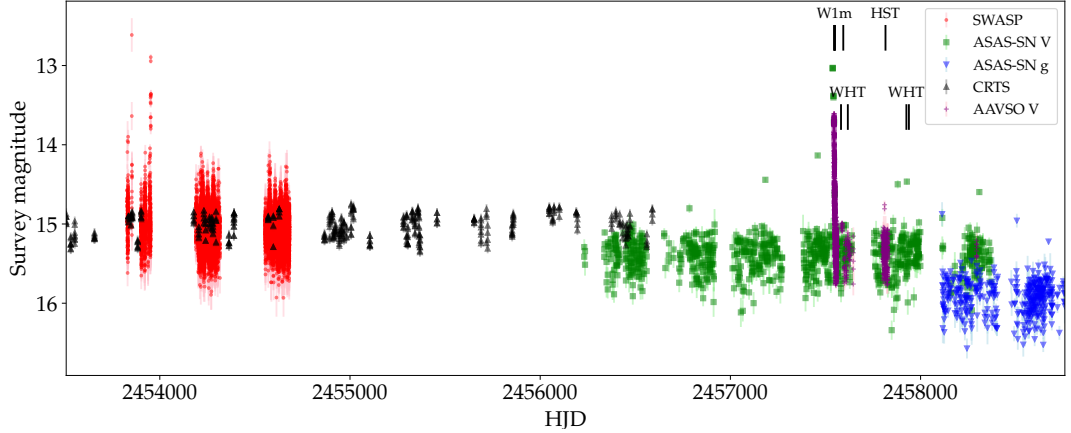
Figure 4.1: SuperWASP, CRTS, ASAS-SN and AAVSO photometry for V1460 Her from 2005 December 5 to 2019 October 2. Evidence for outbursts appear at JD 2453952 (SuperWASP) and JD 2457538 (ASAS-SN). The second outburst was also covered extensively by AAVSO observers and we show their V-band photometry here. The surveys have different bandpasses and therefore their magnitude zero-points differ. The total time span is 5250 d. Vertical marks indicate the dates of the W1m high-speed photometry (see Fig. 4.3, 4.4), the *HST* ultraviolet spectroscopy (see Fig. 4.11, 4.12, 4.14) and the WHT ISIS spectroscopy (see Fig. 4.5, 4.6, 4.9, 4.10).

This is a system where the secondary star dominates the flux in the visible and near infrared part of the spectrum. The phase-folded light curve (Fig. 4.2) of the SuperWASP data therefore shows modulation caused by the tidal distortion of the secondary star and gravity darkening on its near side. The non-sinusoidal nature of this light curve is likely to be due to starspots on the surface. This modulation was fitted as a function of orbital phase to account for the relative contribution of the secondary during the analysis of the time resolved spectroscopy in section 4.2.3.

The ASAS-SN survey (Shappee et al., 2014; Kochanek et al., 2017) has 1595 data points for V1460 Her covering the period from JD 2456231.6923 (2012 October 31) to 2458758.60393 (2019 October 2). As viewed in this dataset (Fig. 4.1), a suspected dwarf nova outburst runs from approximately JD 2457535 (26 May 2016) to JD 2457550 (2016 June 10), or about 15 days. This is approximately 10 years after the outburst detected by SuperWASP. Our W1m data also cover a portion of this outburst.

The American Association of Variable Star Observers (AAVSO) followed V1460 Her during its 2016 outburst and also contributed to the *HST* observations by monitoring the target immediately before and during the observation period to ensure that an outburst did not saturate and potentially damage the *HST* instru-
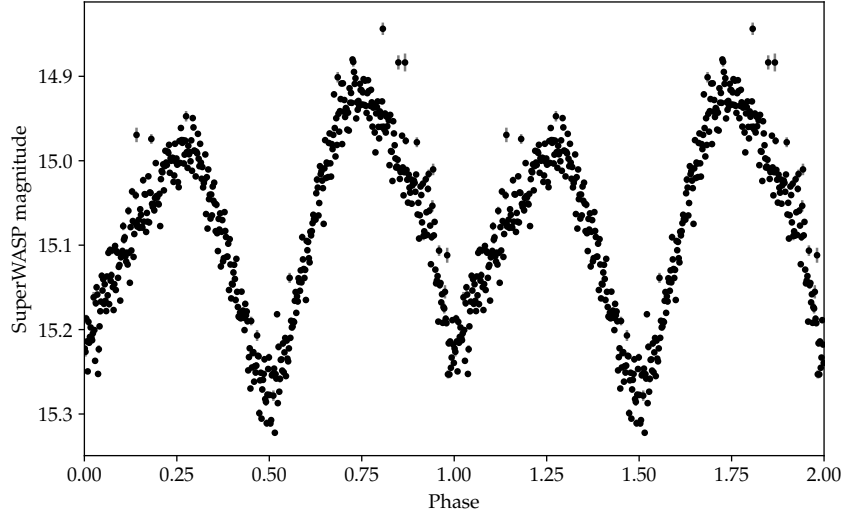
Figure 4.2: Phase folded SuperWASP photometry for V1460 Her. To create this figure, all of the SuperWASP data shown in Fig. 4.1 has been phase-folded and then binned (with weighted average) into 500 phase bins.

ment.

4.2.3 WHT+ISIS spectroscopy

We obtained spectroscopy for six nights, spanning an overall time period from 2016 July to 2017 July. All of the observations were taken with the ISIS spectrograph mounted on the William Herschel Telescope (WHT). The gratings we used were R1200B (centred on 4600 Å) with a resolution of 0.23 Å pixel^{-1} and R1200R (centred on 6400 Å) with a resolution of 0.25 Å pixel^{-1}. In total 618 science spectra were obtained, of which three were discarded due to poor signal to noise. On most nights, flux standards and radial velocity standards were taken at the start and end of the observations and, on the last night, we also took spectra of three K-type (K0V, K5V and K7V) stars to help to characterise the secondary. For the observations on the last two nights, a nearby star was placed further along the slit to allow us to compensate for slit losses and variability in atmospheric transparency for each individual spectrum. The comparison star is about 40 arcsec north of the target and is slightly fainter (*Gaia* magnitude $G = 16.39$). Based on a visual inspection of the spectrum, it is likely to be a K-type star. Its 2MASS catalogue designation is 2MASS J16211745+4413386.

All of the spectra were optimally extracted and reduced using the PAMELA and MOLLY reduction software, (Marsh, 1989b). We fitted splines to the continua of our comparison stars. The ratio of the fit to the original spectrum was then used

73

Table 4.2: Spectroscopy used in this study. The instrument used was ISIS mounted on the William Herschel Telescope.

Date	Gratings	T_{exp} (s)	Total time (min)
2016/07/11	R1200B(4601) R1200R(6400)	54x150 s	135
2016/08/16	R1200B(4601) R1200R(6400)	84x150 s	210
2017/06/20	R1200B(4601) R1200R(6400)	153x150 s	382
2017/06/21	R1200B(4601) R1200R(6400)	143x150 s	357
2017/07/03	R1200B(4601) R1200R(6400)	107x150 s	267
2017/07/04	R1200B(4601) R1200R(6400)	77x150 s	192

to correct for slit losses (see e.g. Marsh, 1990).

For wavelength calibration, Cu+Ne and Cu+Ar arcs were observed several times over the course of the observations. For the red arm, we were then able to further improve the wavelength calibration by examining sky emission features in each of the science and calibration spectra and calculating the final wavelength shift required to assign these features to their known wavelengths. As a final step in wavelength calibration, we observed at least one radial velocity standard each night and used this observation as a calibration for converting wavelengths to radial velocities.

4.2.4 HST+COS spectroscopy

On 2017 March 02 (JD 2457815) we obtained *Hubble Space Telescope (HST)* far-ultraviolet spectroscopy using the Cosmic Origin Spectrograph (COS, Green et al., 2012). The data were collected over three consecutive primary spacecraft orbits (programme ID 14893), for 8306 s of on-source exposure. We observed the target using the Primary Science Aperture, the TIME-TAG mode and the far-ultraviolet grating G140L, centred at 1105Å. The observations were dithered along the spectral direction on the detector using all four FP-POS settings, mitigating fixed pattern noise and detector artefacts. This delivered a spectrum covering the wavelength range 1026–2278 Å at a resolution of $R \simeq 3000$.

The *HST* spectra were also used to derive ultraviolet band photometry. The TIME-TAG observing mode offered by the *HST* UV spectrographs allows the recording of the time of arrival, the position on the detector and the pulse height of each detected event every 32 ms. It is therefore possible to reconstruct a 2D time-resolved image of the detector, where the dispersion direction runs along one axis and the spatial direction along the other, from which a lightcurve of the system can be extracted. Following the method described in Pala et al. (2019), we identified three rectangular

regions on this image: a central one enclosing the object spectrum and two regions to measure the background, one above and one below the spectrum. We considered the wavelength range $1175 < \lambda < 1880\,\text{\AA}$ and masked the geocoronal emission lines from Lyα ($1200 < \lambda < 1224\,\text{\AA}$) and O I ($1290 < \lambda < 1311\,\text{\AA}$) and all the most prominent emission features from the accretion disc: N V ($1231 < \lambda < 1250\,\text{\AA}$), Si IV ($1380 < \lambda < 1415\,\text{\AA}$), N I ($1481 < \lambda < 1494\,\text{\AA}$), He II ($1635 < \lambda < 1646\,\text{\AA}$), which are not representative of the white dwarf. We binned the data into five second bins and counted the number of events in each of those corresponding to the stellar spectrum. Once corrected for the number of counts from the background, these data provide the lightcurve of the target in counts per second. We discuss the spectrum and the derived photometry in sections 4.3.8 and 4.3.9.

4.3 Results

4.3.1 Photometric behaviour in outburst

The W1m photometry in Figs. 4.3 and 4.4 shows the gradual progression of the target from outburst to quiescence. For all of the observations, the same comparison was used for calibration. This means that the relative magnitude is calibrated against the same baseline. Since no offset has been applied to any of the light curves shown, the evolution of overall brightness of the system from outburst to quiescence is directly represented in the figures. In order to better represent the contribution of the disc, the quiescent light curve was fitted with a sinusoid (and harmonics) and this was subtracted from each night's data.

Our outburst data confirm behaviour reported by Zola et al. (2017) and show dominance by an accretion disc during outburst, transitioning to the quiescent light curve which is dominated by the tidally-distorted secondary star.

4.3.2 Ephemeris

Since there is a long baseline of over 14 years of published photometry for V1460 Her, all of these data were combined and used to find an orbital period. We used SuperWASP, CRTS and ASAS-SN observations and computed a Lomb-Scargle periodogram to determine an initial estimate for the period. This was then further refined by fitting a sinusoid plus harmonics to all of the data. Once we had the period, the WHT spectroscopy was folded to this period and a zero point was determined from the radial velocity zero point of the secondary. Our ephemeris for
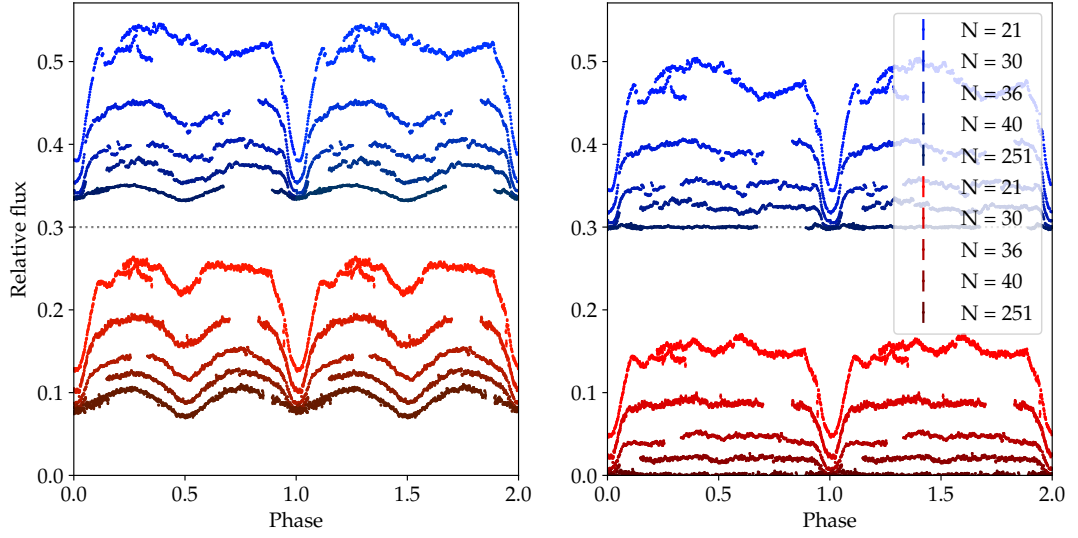
Figure 4.3: The W1m photometry for V1460 Her. The upper panels show the data for the BG40 (blue) filter (offset by 0.3) and the lower plots show the Z-band (red) filter. The relative flux is computed from the same comparison star each night. No offset has been introduced to data on subsequent nights, so the decrease in relative flux is due to the target fading from outburst to quiescence. The value N in the plot legend refers to the approximate number of orbits since the start of the outburst (as calculated from the information given in Maehara (2016), JD 2457541.113). The right hand panel shows the relative flux *after* subtracting the quiescent light curve (N=251) from the originals.
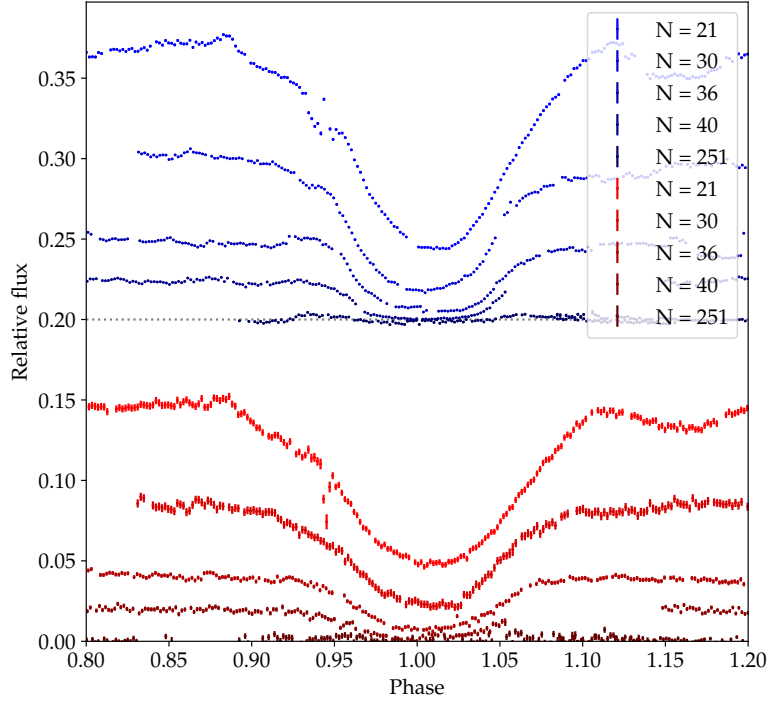
Figure 4.4: Similar to Fig. 4.3, but in this figure we limit the phase to show primary eclipse in more detail. The blue data have been offset by 0.2.

V1460 Her is

$$BJD(TDB) = 2457760.46887(6) + E \times 0.20785223(3), \tag{4.1}$$

and gives the times of primary eclipse, when the donor star is closest to Earth.

4.3.3 Optical spectrum

The combined ISIS red and blue spectra (Fig. 4.5) show a combination of absorption lines from the secondary and double-peaked Balmer emission from the disc. Although we detect weak He I emission at 6678 Å, there is no detection of He II emission.

4.3.4 Spectral type of the secondary

The individual target spectra show many absorption features from the secondary star which move in approximate anti-phase to the emission lines. Using the ephemeris discussed in the previous section, we cross-correlated each individual science spectrum with a hand-picked example with high S/N. A fit to this cross-correlation gave
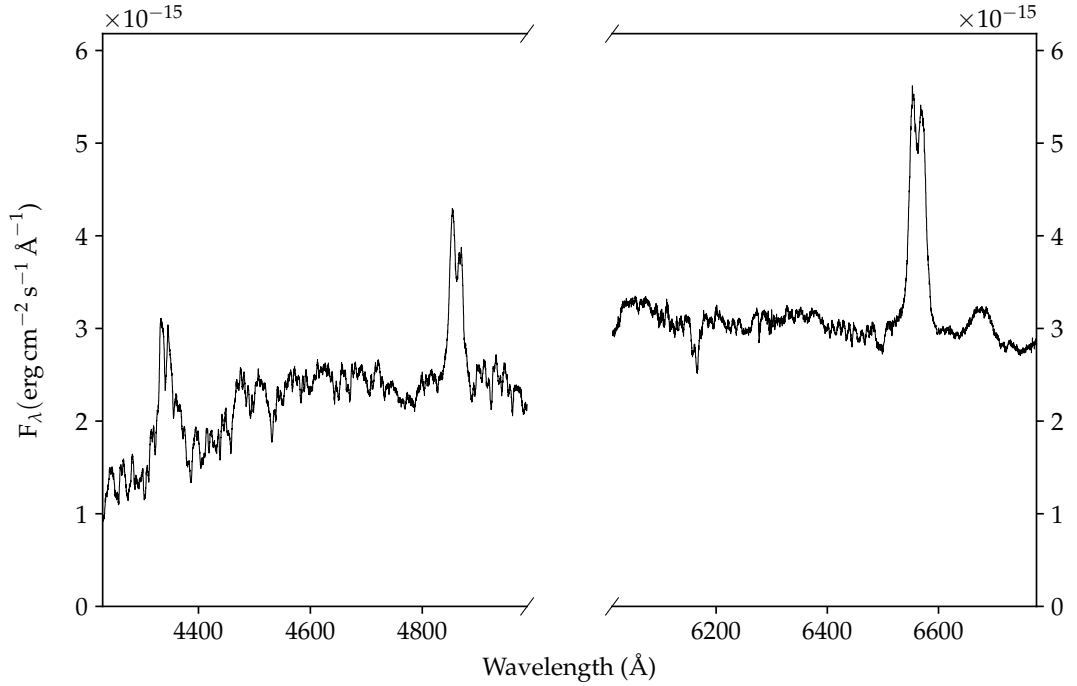
Figure 4.5: The overall average spectrum of the ISIS red and blue arms. The average was computed with respect to a heliocentric rest frame.

an estimate for the secondary's semi-amplitude, K_2. The ephemeris and the K_2 estimate were used to generate an average spectrum as computed in the rest frame of the secondary. This average spectrum was then used to make an estimate of the spectral type of the donor by comparing it to the reference spectra taken on the last night of the observations. The reference spectra are HD 124752 (K0V), HD 122120 (K5V) and HD 234078 (K7V). By artificially introducing rotational broadening to these spectra and then comparing them to our target spectra we were able to find the value of $v \sin i$ that gave us the best match to the donor. This was done by stepping through various values of $v \sin i$ and computing the minimum χ^2 after subtraction from our average target spectrum. The spectrum of HD 122120 (K5V) with a rotational broadening of $v \sin i = 110.5 \pm 0.4 \, \mathrm{km \, s^{-1}}$ gave us our best subtraction. The other two spectral types resulted in subtractions with residual features in the continuum (Fig. 4.6). Although this approach is somewhat qualitative, we can be certain that the spectral type of the secondary is within one or two subtypes of K5. In Fig. 4.7 we show the averaged target spectrum (in the rest frame of the secondary), the rotationally broadened template spectrum and the result of the subtraction of the two.
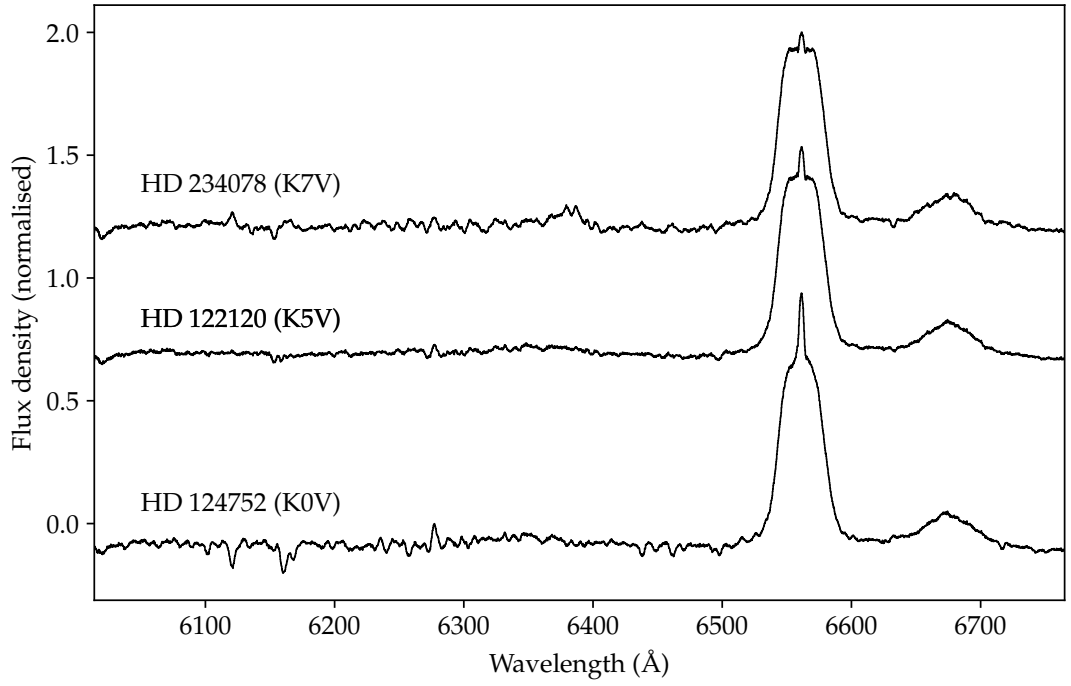
Figure 4.6: Testing the subtraction of different template spectra from our target. The results of subtracting a rotationally broadened version of the three template spectra from the time averaged spectrum in the rest frame of the secondary. Our best results were achieved for a spectral type of K5V. The flux density is normalised and an offset of 0.5 units has been applied to each subsequent spectrum.
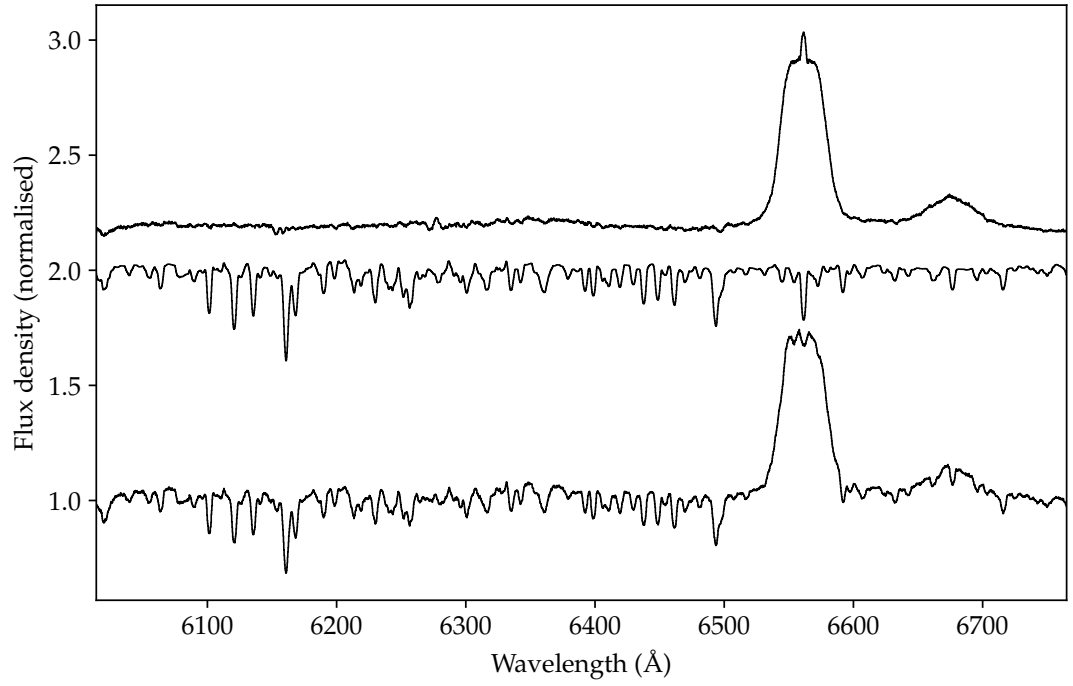
Figure 4.7: Subtracting the spectrum of the secondary. The lower spectrum is the average of the target once shifted into the rest frame of the secondary. The middle spectrum is that of HD 122120 (K5V) after application of rotational broadening with the value $v \sin i = 110.5$ km s^{-1}. The upper spectrum is the result of subtracting the two.

4.3.5 Orbital radial velocities

Now that the spectral type of the secondary had been established, we were able to examine its radial velocity. HD 122120 has a well defined radial velocity which is published in Soubiran et al. (2013). The rotationally broadened version of its spectrum was cross-correlated with the science spectra for our target. We limited the analysis to a region of the spectrum that is dominated by flux from the secondary star and contains no emission lines, 6120 – 6265 Å. The cross correlation process resulted in 615 radial velocities. These were fitted to a sinusoid of the form $v(t) = \gamma + K_2 \sin(2\pi(t - T_0)/P)$, see Fig. 4.8, where v is the orbital speed projected along our line of sight. The derived parameters are listed in Table 4.3.

The strongest emission feature in the optical spectra is the Balmer Hα line. Using a method described in Schneider and Young (1980), involving cross-correlating two Gaussian profiles, we measured the radial velocity of the line wings of this feature. This method gives consistent results for phases outside of the primary eclipse. We found the optimal separation for the Gaussian profiles was $1800\,\mathrm{km\,s^{-1}}$. This can be confirmed by consulting with Fig. 4.10 which indicates that a separation of this amount means that we are confining our radial velocity search to the line wings.

The zero-crossing points in the radial velocity measurements differ by 0.078 in phase which corresponds to 23.5 min. Stover (1981) noticed this effect in several systems, and explained it by an area of enhanced emission associated with the region where the accretion stream impacts the disc.

For each of the 615 science spectra, the rotationally broadened spectrum of HD 122120 was shifted to match the correct radial velocity for the phase in the orbit and then subtracted. Since the secondary's contribution to the overall flux is highly dependent on the phase of the orbit (see Fig. 4.2), each shifted template spectrum was multiplied by a phase dependant constant to reflect its proportional contribution. The resulting trails are shown in Fig. 4.9.

4.3.6 Masses of the components

Assuming co-rotation, the equatorial speed of a Roche-lobe filling star is related to the orbital speed of its centre of mass by a function of the mass ratio q alone. Using Paczyński (1971)'s equation for the radius of the secondary star's Roche lobe leads to

$$\frac{v \sin i}{K_2} = 0.46[(1 + q)^2 q]^{1/3}, \tag{4.2}$$
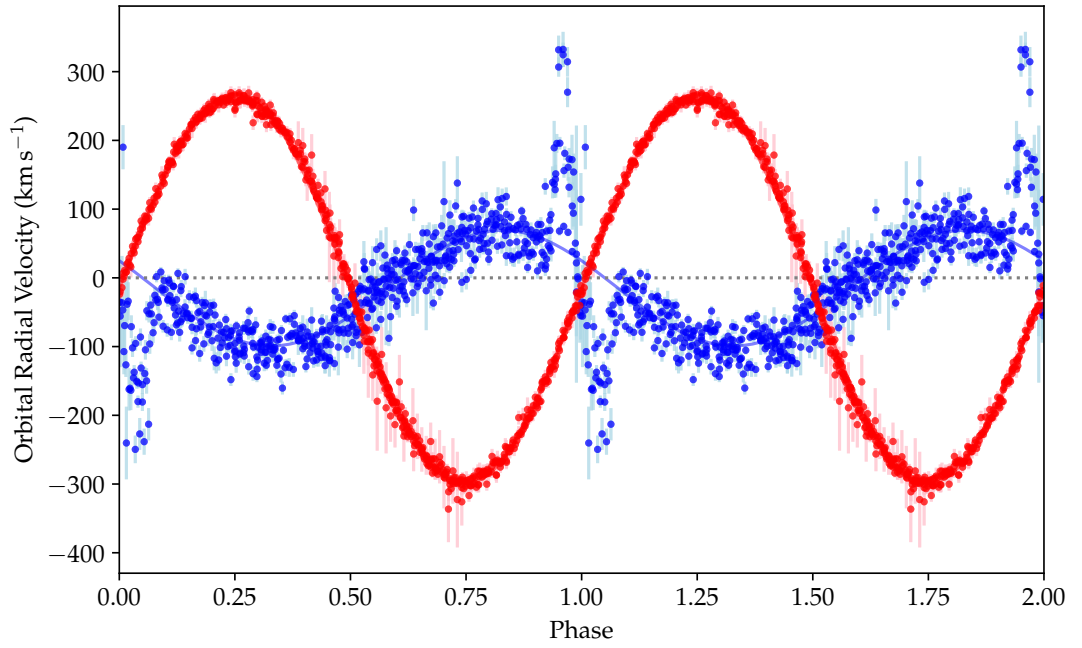
Figure 4.8: Fit to the radial velocities of both components of V1460 Her. The velocities of the secondary were computed by cross correlation with HD 122120. Those for the primary were computed with a Young and Schneider analysis of the Hα emission feature. The emission features are affected by the primary eclipse. For the calculation of the orbital parameters listed in Table 4.3, the points between phases 0.80 and 1.20 were excluded.
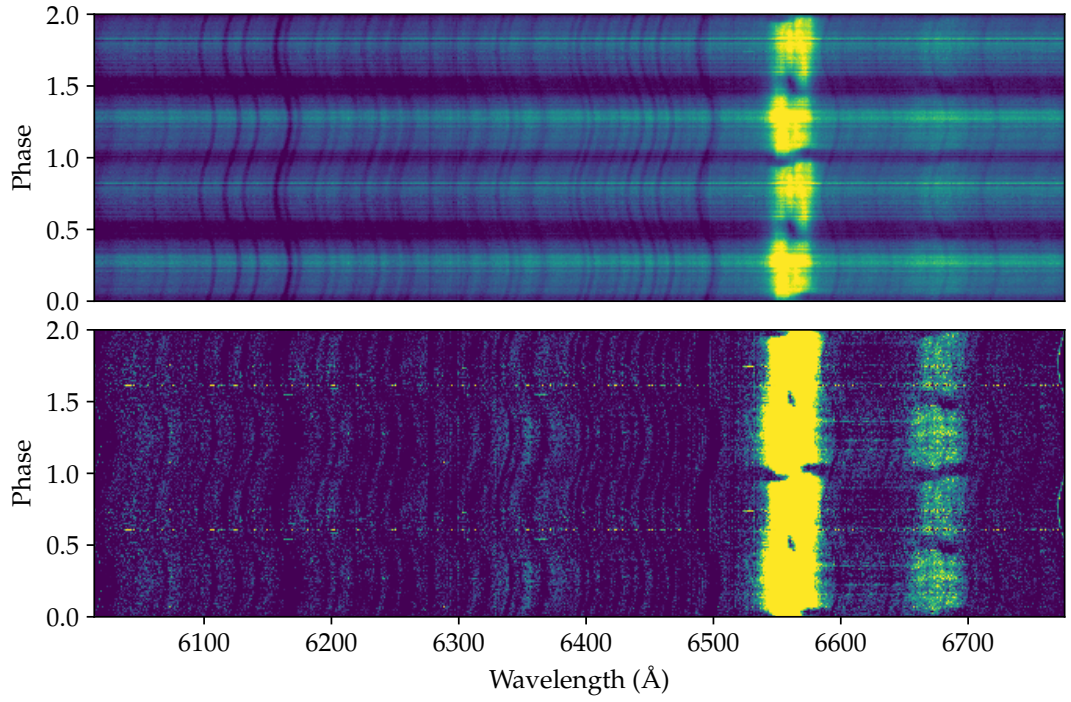
Figure 4.9: Trails of the spectra taken in the red arm of ISIS. The upper trail shows the original data in the heliocentric rest frame. The lower trail shows the result after subtracting a rotationally broadened K5 star template to remove contribution from the secondary. The emission lines on the right are Hα and He I 6678. Our removal of the secondary's absorption features has not been perfect, but the contrast of the emission and the presence of the He I is enhanced.

for $0 < q < 0.8$ (Wade and Horne, 1988a). In this equation v means the equatorial velocity.

Using our values for K_2 and assuming the value of $v \sin i$ derived in the previous section, we calculate $q = 0.339 \pm 0.004$. Examining both the W1m and *HST* photometry of the primary eclipse, it is possible to estimate the duration of the white dwarf's eclipse, $\Delta\phi$, from which, using the geometry of the Roche lobe and an estimate of the mass ratio (Chanan et al., 1976), the inclination of the orbit can be deduced. We derived $\Delta\phi$ by measuring the FWHM of the eclipse profile for each of the 4 nights of photometry taken during outburst on the W1m in both the red and blue filters and also from the ultraviolet photometry taken from the *HST*. Since our *HST* data only included an eclipse *egress* and we missed the *ingress*, we had to assume a symmetrical profile for the shape of the eclipse. These measurements gave a value of $\Delta\phi = 0.094 \pm 0.009$, which leads to an inclination between $84°$ to $90°$, or $\sin i \simeq 0.997$.

The mass function for a compact binary system is given by,

$$\frac{(M_1 \sin i)^3}{(M_1 + M_2)^2} = \frac{P_{\mathrm{orb}} K_2^3}{2\pi G},\tag{4.3}$$

and assuming that $\sin i \simeq 0.997$, we can derive a mass for each component of

$$M_1 = 0.869 \pm 0.006\,\mathrm{M}_\odot,\tag{4.4}$$

$$M_2 = 0.295 \pm 0.004\,\mathrm{M}_\odot.\tag{4.5}$$

Using equation 2 in Eggleton (1983) for a Roche lobe filling secondary, we can derive a radius of $R = 0.430 \pm 0.002\,\mathrm{R}_\odot$ and a separation of the centre of mass of each component of the binary of $a = 1.478 \pm 0.003\,\mathrm{R}_\odot$.

Since, during quiescence, the secondary star dominates the light in the optical region, we can estimate the radius of the donor independently by using data from *Gaia*. The *Gaia* DR2 data for V1460 Her gives a parallax of $3.764 \pm 0.026\,\mathrm{mas}$, corresponding to a distance of $265.7 \pm 1.8\,\mathrm{pc}$. Using our estimate for the spectral type of the donor as a K5 star we chose a temperature of $4350\,\mathrm{K}$, as would be expected from a main sequence star of this type. We did not use the *Gaia* published estimate of $4861\,\mathrm{K}$ for V1460 Her as this combines flux from all components of the binary and is subject to the variability of the target. We assumed a reddening of $E(B - V) = 0.02 \pm 0.02$ and calculated a line of sight extinction in the *Gaia* G-band of $A_{\mathrm{G}} = 0.04 \pm 0.04$. Our reddening estimate was taken from Capitanio et al. (2017). Using

Table 4.3: Orbital and stellar parameters measured in this paper.

M_1	$0.869 \pm 0.006\,M_\odot$
M_2	$0.295 \pm 0.004\,M_\odot$
K_1	$84.1 \pm 1.5\ \mathrm{km\,s^{-1}}$
K_2	$283.3 \pm 0.6\ \mathrm{km\,s^{-1}}$
γ_1	$-15.0 \pm 1.2\ \mathrm{km\,s^{-1}}$
γ_2	$-15.1 \pm 0.4\ \mathrm{km\,s^{-1}}$
q	0.339 ± 0.004
a	$1.478 \pm 0.002\,R_\odot$
R_2	$0.430 \pm 0.002\,R_\odot$
T_0	$2457760.46887(6)$ d
Period	$0.20785223(3)$ d
White dwarf spin period	38.875 ± 0.005 s
Secondary spectral type	K5

equations 8.1, 8.2 and 8.6 of *Gaia* Data Release 2 documentation[1] we calculate $M_G = 7.87 \pm 0.18$ and $R_2 = 0.47 \pm 0.04\,R_\odot$. The potential inaccuracy in determination of the donor's spectral type and hence temperature is also a contributor to the uncertainty in this calculation. If we choose a K4 and a K6 type for comparison, our calculations of the radius become $R_2 = 0.43\,R_\odot$ for a K4 donor and $R_2 = 0.51\,R_\odot$ for a K6 donor. The *Gaia*-based estimate of the donor's radius is in agreement with the estimate of $0.43\,R_\odot$ based on the measurement of $v \sin i$ as described in the previous paragraphs.

4.3.7 Spectral features

Our spectra, which were taken during quiescence, leave no doubt as to the presence of a disc, which is not clearly evident from photometry, except in outburst. The broad, double-peaked emission features are an important indication, and there is in addition, evidence of a "rotational disturbance" (similar in nature the Rossiter-McLaughlin effect) first seen in CVs by Greenstein and Kraft (1959). The rotational disturbance is seen when the emission lines from a disc are eclipsed. If the disc orbits in a prograde direction within the binary, the approaching, blue-shifted side of the disc is first eclipsed, followed by the red-shifted, receding side. This can be seen clearly around the eclipse in the trail of Fig. 4.10 and also in the emission line radial velocities of Fig. 4.8.

V1460 Her shows an additional behaviour of particular interest. At around phase 0.5 there is a feature in its trailed spectrum akin to an inverted rotational disturbance. We identify this with the "mirror eclipse" feature first found by Lit-

---

[1]https://gea.esac.esa.int/archive/documentation/GDR2/
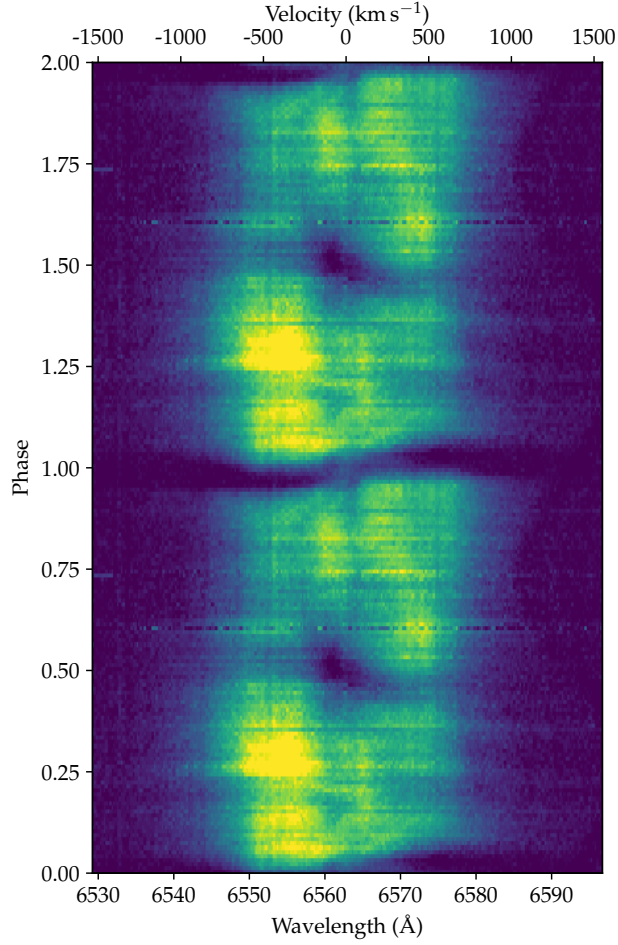
Figure 4.10: The trailed spectrum at Hα for V1460 Her.

tlefair et al. (2001). This feature results from the passage of the disc in front of a bright secondary star as its light passes through the disc, and is partially absorbed by it. Littlefair et al. (2001) discovered this phenomenon in K-band spectra of the dwarf nova IP Peg which has a secondary star that dominates in the near infrared. V1460 Her's bright donor makes this the first system where the mirror eclipse has been recognised at Hα. The key property needed to see a mirror eclipse is that there are lines-of-sight to the secondary that pass through parts of the disc which are optically thin in the continuum. Interestingly, the mirror eclipse in V1460 Her does not seem to extend into the line wings and has no obvious influence upon the emission line velocities measured from the line wings at around orbital phase 0.5. This suggests that the inner disc is optically thick in the continuum, as is expected for accretion discs in cataclysmic variable stars.

Table 4.4: Known CVs with anomalous N V to C IV emission line ratios and donors that are thought to have experienced some amount of CNO burning.

AE Aqr	Jameson et al. (1980)
BY Cam	Bonnet-Bidaud and Mouchet (1987)
TX Col	Mouchet et al. (1991)
V1309 Ori	Szkody and Silber (1996)
MN Hya	Schmidt and Stockman (2001)
EY Cyg, BZ Uma	Winter and Sion (2001); Sion (2002)
GP Com	Lambert and Slovak (1981)
	Marsh et al. (1995b)
RX J2329, CE315	Gänsicke et al. (2003)
U Sco, V1974 Cyg	Sanad (2011)
CSS 120422:J111127+571239	Kennedy et al. (2015)
V1460 Her	This paper

4.3.8 *HST* spectrum

The *HST*+COS spectrum of V1460 Her is shown in Fig. 4.11. No clear features from the white dwarf are visible, but the shape of the continuum suggests that it may result from viewing the white dwarf through significant absorption similar to the "iron curtain" seen in the dwarf nova OY Car (Horne et al., 1994). Most accreting sources display strong C IV 1550 emission which we see no sign of here. In addition, there is strong emission from N V at 1240 Å. This suggests an anomalous nitrogen-to-carbon ratio, which was used by Schenker et al. (2002) in the case of AE Aqr as an indication that significant CNO processing had taken place in the donor. Therefore the donor star in V1460 Her is the descendant of an evolved star, and the white dwarf is accreting material enriched in nitrogen and depleted in carbon due to the CNO cycle. Similar anomalous N/C ratios have been identified in several other CVs, as shown in Table 4.4.

4.3.9 Spin of the white dwarf

As discussed in section 4.2.4, the HST ultraviolet spectroscopy was also used to derive time-resolved ultraviolet photometry. Our data covered approximately 75 per cent of an orbit and included a small section and the egress of a primary eclipse. The photometry is shown in Fig. 4.12. The amount of scatter seen in the data in phases away from eclipse is significantly larger than expected given the uncertainties from photon statistics.

In order to look for pulsations from the white dwarf, we computed a periodogram of the *HST* data. The fractional amplitude spectrum is shown in Fig. 4.13.
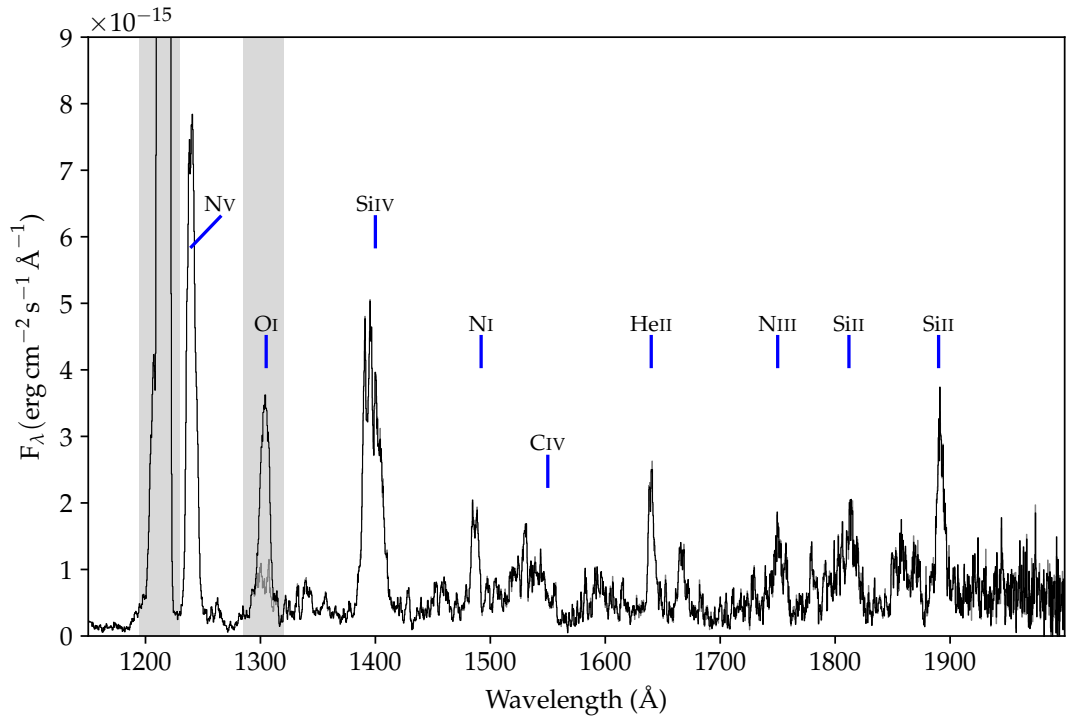
Figure 4.11: The *HST*/COS far-ultraviolet spectrum of V1460 Her. Most notable is the strong N v and the complete lack of C iv. The geocoronal features of Lyα and O i are marked by grey rectangles. The grey spectrum most notable near the O i feature at 1295 – 1314 Å is the average spectrum derived from the exposures taken while *HST* was night-side of the Earth. This shows that the O i emission in the main spectrum is largely due to terrestrial airglow.

There is a strong peak at around 2222 cycles d^{-1} caused by a periodic modulation with a semi-amplitude of 15 per cent and a period of 38.875 ± 0.005 s. A closer inspection (Fig. 4.14) of the light curve shows that the modulation is directly visible, and that it disappears during the eclipse. The source of this modulation, which was observed during quiescence, can only be due to the spin of the underlying white dwarf, or possibly its orbital sideband. The spin period of the white dwarf is then either equal to the observed 38.875 s period, or it is very close to it. It is possible that we are seeing an identical pattern generated by each pole in which case the true spin period is in fact twice 38.875 s. There are no other significant periodic signals, but note that the *HST* data covers less than an orbit of V1460 Her and therefore cannot resolve signals spaced by the orbital frequency or less from each other. The ephemeris of this modulation is

$$\mathrm{BJD(TDB)} = 2457815.43095(8) + E \times 4.4994(4) \times 10^{-4}, \tag{4.6}$$

where the constant term marks the time of maximum flux.

By time-binning individual data from the CORRTAG files written by the COS instrument, we were able to generate time resolved spectra to sample the pulse signal of this 38.9 s modulation. We generated 2132 spectra with 3.9 s time resolution and then averaged them into 10 phase bins. Then, after rebinning the wavelength axis into 100 wavelength bins, we computed the amplitude of the pulsation as a function of wavelength. The pulsation spectrum is shown in Fig. 4.15. It is clear that the pulsations emanate from the flux in the continuum rather than from the emission lines, and the pulsation spectrum appears to be somewhat bluer (hotter) than the mean spectrum. In their study of the rapidly rotating white dwarf primary in AE Aqr, Eracleous et al. (1994) showed that their pulsation spectrum was matched by a model of a solar abundance white dwarf with $\log g = 8$ and conclude that the pulsations are the consequence of the heated pole caps on the surface of the white dwarf. We do not have sufficient data to perform a similar analysis, but we assume that the modulation in V1460 Her is due to a similar process.

4.4   Discussion

The donor star's mass of $0.29\,\mathrm{M}_\odot$ (Table 4.3) is far less than the expected mass of a K5 star on the main sequence ($0.67\,\mathrm{M}_\odot$), and is closer instead to the typical mass of an M3.5 donor star, (Knigge, 2006). Moreover, the radius of a $0.29\,\mathrm{M}_\odot$ main sequence star is expected to be around $0.30\,\mathrm{R}_\odot$, so the donor here is ≈ 50 per cent larger than expected. It is clear then that the donor is overly large and hot compared
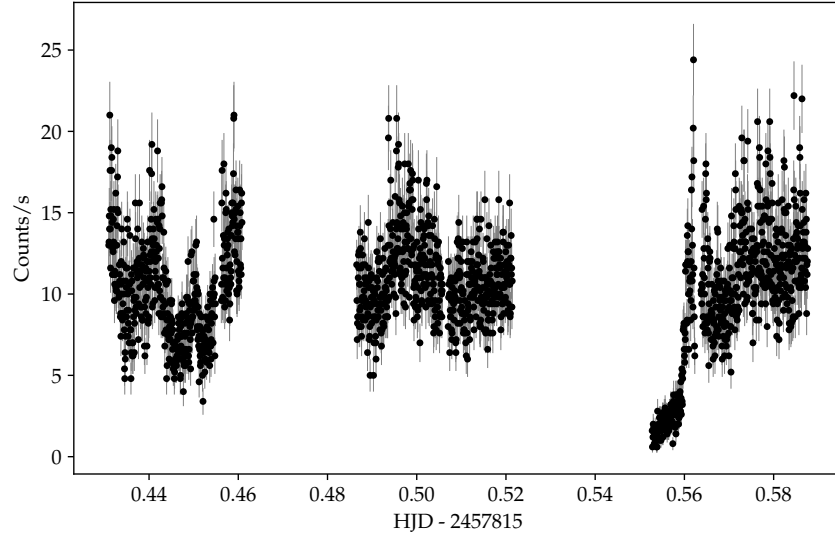
Figure 4.12: Photometry derived from the HST spectroscopy as described in the text. The large scatter in the data is partially due to a true variability in the UV flux over a 38.9 s period.
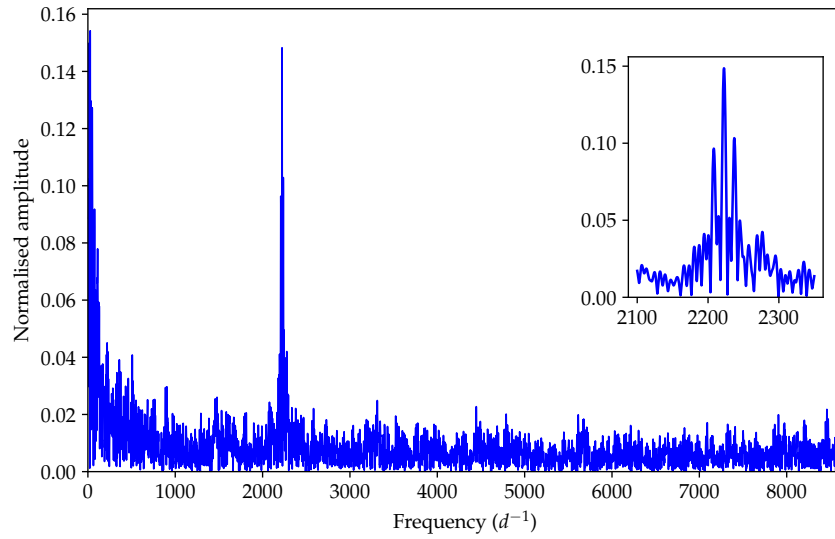
Figure 4.13: The fractional amplitude spectrum up to the Nyquist frequency for our adopted 5 s sampling rate. Data taken during the eclipse do not show the 38.9 s modulation and have been excluded from this analysis.
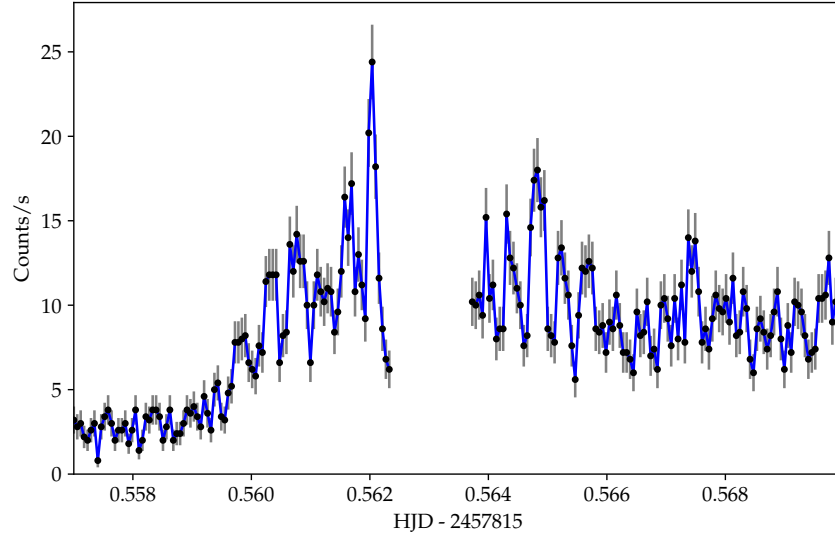
Figure 4.14: Closer view of some of the HST derived UV photometry. This shows the eclipse egress and the 38.9 s modulation which turns on during the egress.
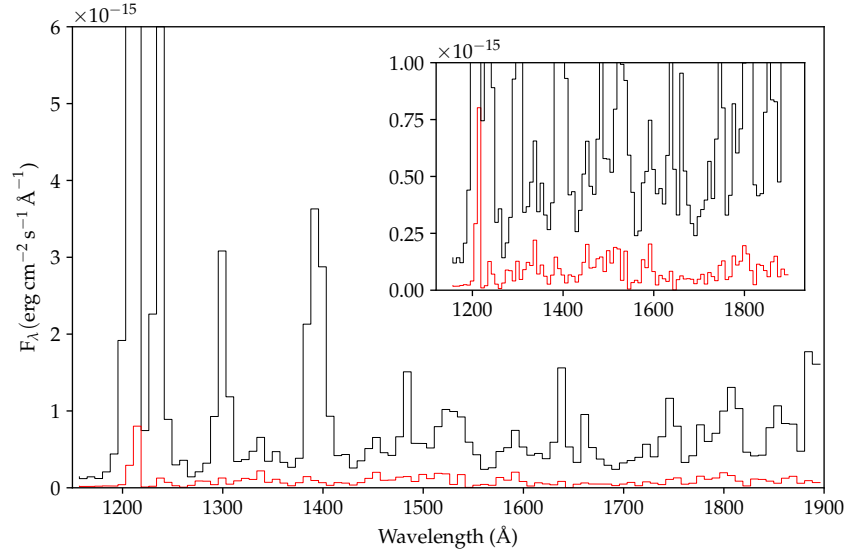
Figure 4.15: The pulsation spectrum (shown in red) along with the overall average flux. The pulsation amplitude comes from the continuum region of the spectrum and not from the emission features.

to main sequence stars of similar mass, a consequence presumably of past mass loss that has happened on a timescale shorter than its Kelvin-Helmholtz (thermal) timescale of $\tau_{\mathrm{KH}} \sim 7 \times 10^7$ yr. The *HST* spectra reveal anomalous abundance ratios between N v, Si iv and C iv; in fact we find no evidence for any C in our spectra. This leads us to conclude that V1460 Her is accreting from an evolved donor that has undergone CNO processing. One possible explanation for the short time scale of mass transfer and also the evidence for CNO burning is that V1460 Her may have started accretion from a donor that was more massive than the white dwarf leading to a high rate of mass transfer and significant stellar evolution (Sanad, 2011; Schenker et al., 2002). Podsiadlowski et al. (2003) use binary population synthesis (BPS) techniques to show that, according to their models, CVs with a period > 5 hrs are likely to be dominated by such evolved donors.

Many dwarf novae with periods similar to V1460 Her, undergo outbursts several times per year, eg RX And $\simeq 15$ d, EX Dra $\simeq 25$ d CZ Ori $\simeq 40$ d and AT Cnc $\simeq 30$ d. It is thought that this outburst frequency is driven by the donor stars experiencing strong magnetic stellar wind braking driving the evolution towards shorter orbital periods, resulting in moderately high mass flow rates through the discs in these systems. Looking at the archival photometric data (section 4.2.2) however, V1460 Her only seems to outburst about once every ten years, assuming that we have not missed any outbursts when the target was seasonally inaccessible. This suggests that the mass transfer rate is lower than predicted by standard CV evolution models. This may be a consequence of the unusual state of the donor star which should be shrinking towards a more main-sequence-like structure, driving it towards detachment from its Roche lobe. Alternatively, or perhaps additionally, the low outburst frequency may be the result of disruption of the inner disc by the magnetic white dwarf, as suggested by Angelini and Verbunt (1989). Hameury and Lasota (2017) show that dwarf nova outbursts from intermediate polars are expected to be less frequent and of shorter duration than those from non-magnetic CVs. It appears then that V1460 Her could be a marginal candidate for this group, with outbursts every 10 years, lasting about 15 days. However, two other CVs with evolved donors, HS0218+3229 (Rodríguez-Gil et al., 2009, $P_{\mathrm{orb}} = 7$ h) and KIC5608384 (Yu et al., 2019, $P_{\mathrm{orb}} = 9$ h) also outburst infrequently and are not obviously magnetic, perhaps suggesting that it is the state of the donor star that is of most importance.

The unusual state of the donor star points to a relatively recent emergence from a high rate of mass transfer. Schenker et al. (2002) developed a model in which AE Aqr emerged from a supersoft X-ray phase during which the accretion

rate was high enough ($\sim 10^{-7} \, \mathrm{M}_\odot \, \mathrm{yr}^{-1}$) to drive steady fusion on the surface of the white dwarf. At the same time, one would expect the white dwarf to spin up during this phase. Once the high rate of mass transfer ceases, there would be tendency for the white dwarf to spin down, and Schenker et al. (2002) suggest that exactly this explains why we now see AE Aqr in a state of rapid spin-down of the white dwarf, which is losing more rotational energy than seen from the system as a whole. V1460 Her seems in every way to be a second example of this process. Not only does it have a clearly evolved donor star, but it contains a rapidly spinning white dwarf, which is only a little slower than the white dwarf in AE Aqr itself. It will be fascinating to see whether, like AE Aqr and the possibly-related system AR Sco (Marsh et al., 2016; Stiller et al., 2018), the white dwarf in V1460 Her is in a state of rapid spin-down; this will require alias-free measurement of the pulsation phase over a number of years, not possible from the data we have in hand at present. V1460 Her differs from AE Aqr in having a normal-looking accretion disc, which is visible in quiescence through line emission, and capable of driving outbursts, albeit rarely. AE Aqr on the other hand is known as the only propeller-type system amongst accreting white dwarfs, flinging matter transferred from the donor out of the system altogether as proposed by Wynn et al. (1997). AR Sco is more extreme still and seems to have entirely ceased to accrete (Marsh et al., 2016), possibly as a result of the injection of spin angular momentum into the orbit. In this picture, V1460 Her is a good candidate for the less extreme end, with a magnetic field too weak to disrupt its accretion disc let alone lead to propeller ejection and the complete cessation of accretion.

Isolated white dwarfs are thought to be extremely slow rotators with rotational velocities below $10 \, \mathrm{km \, s}^{-1}$ (Berger et al., 2005), although Hermes et al. (2017) show that for apparently isolated white dwarf pulsators, spin periods range from a few to about 100 hrs with the peak in period distribution at about 40 hrs. Isolated magnetic white dwarfs have measured spin periods of several hours to a year or so (Brinkworth et al., 2013). As mentioned in the previous paragraph, our suspicion is that the rapid spin of the primary in V1460 Her is due to a recent episode of accretion and may have been aided by the suppression of nova events.

It is interesting that with V1460 Her, another system in addition to AE Aqr has been found with a rapidly-spinning white dwarf that seems to have resulted from a recent phase of high accretion. If there is a puzzle associated with white dwarf spin evolution under accretion, it is perhaps why more of them are not found to be rapidly spinning, because only a little mass needs to be accreted to bring a white dwarf close to its break-up spin, much faster than many accreting white dwarfs

are found to rotate. Livio and Pringle (1998) suggested that angular momentum loss during classical nova eruptions might be the reason for slow spin rates. This fits remarkably well with the recent supersoft phase idea, because a key feature of the supersoft phase is that the accreted hydrogen steadily fuses on the white dwarf surface so that there are no classical nova eruptions in these systems. This might suggest that rapidly spinning white dwarfs are more likely to be located in systems with evolved donor stars, a testable hypothesis.

4.5 Conclusion

We find that V1460 Her belongs to a select group of cataclysmic variable stars in which the donor star is significantly over-luminous and over-sized (by 50 per cent) for its mass. This indicates that it is probably the remnant of a phase of high rate mass transfer. It is moreover eclipsing and shows phenomena in its spectra associated with both the eclipse of its disc by the donor star and the eclipse of the donor star by the disc. Most remarkably of all, V1460 Her shows strong pulsations on a period of 39 sec in *HST* ultraviolet data. This is a clear sign of a rapidly spinning white dwarf, the second fastest known amongst cataclysmic variables after the system AE Aqr. AE Aqr also hosts an evolved donor star, and these two systems may share a history of white dwarf spin-up through high rate accretion. We speculate that this may only occur if accretion at a rate high enough to suppress classical nova eruptions has taken place.

Chapter 5

V808 Aur

5.1 Introduction

In 2008, December 31st, the Catalina Real-Time Transient Survey reported the transient event, CSS081231, when CRTS J071126+440405 brightened from $V \simeq 18$ to $V \simeq 14.5$. On the next day the vsnet-alert #10867 reported that this CRTS source had a blue counterpart in the USNO B1.0 catalogue. The first time-resolved photometric observations were obtained by Denisenko and Korotkiy and sent to the Cataclysmic Variable Network (CVnet) discussion #1208 where they reported the detection of deep (primary) eclipses with a period of 1.96 hours. In 2009, optical spectra were taken at the WHT and although the target had, by then, returned to a low state, the emission lines and the detection of cyclotron humps in the near infra-red confirmed that the target was a polar. Subsequently, this object was named in the General Catalogue of Variable Stars as V808 Aur ($07\,h\,11\,m\,26.0\,s$ $+44°04'05''$ J2000).

Schwope et al. (2015) reported in detail on the photometric properties of V808 Aur noting that it appears to display three separate accretion states, low, intermediate and high. They also determined an estimate for the orbital inclination of the system using the geometry of the Roche lobe. X-ray observations by Worpel and Schwope (2015) suggest evidence of a second accretion pole, which is not evident in the optical light-curves.

In this chapter I report on spectroscopic observations taken in both a high and low state and present analysis of the eclipses of V808 Aur.
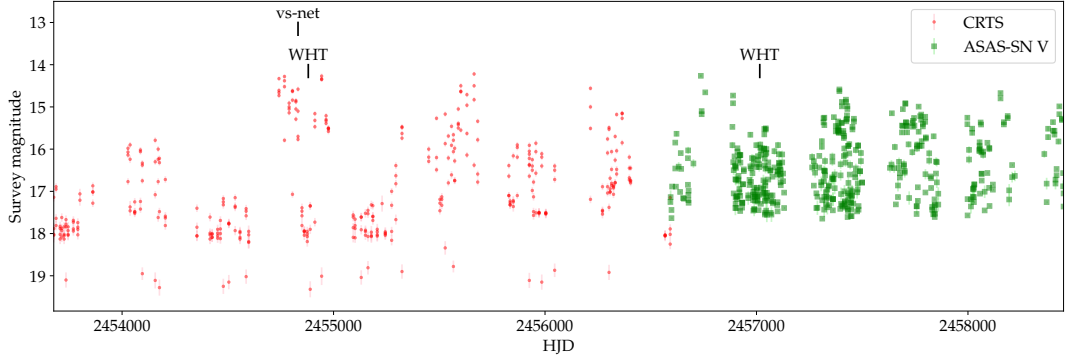
Figure 5.1: Long term light curve of the CRTS and ASAS-SN photometry for V808 Aur. The total time span is $\simeq 13$ yrs. Marked on the figure are the times of the original vs-net alert 10867 and the two periods when our spectroscopy was taken at the WHT.

5.2 Observations

5.2.1 Published survey photometry

V808 Aur has several years of observations in the CRTS catalogue going back to November 2005 and continuing until April 2013. The ASAS-SN survey (Shappee et al., 2014; Kochanek et al., 2017) begins coverage of our target in 2013 October and continues to cover it at the time of writing. The most recent data point is from November 2018. Combined, these two sources provide a total time span of 13 years. The 13 year light curve is shown in Fig. 5.1 with the phase folded version in Fig. 5.2. V808 Aur has typical behaviour for a polar in that it can be seen to switch between a high state and a low state and also exhibits intermediate states (Schwope et al., 2015). Evidence from the long-term photometry suggests that it spends more than 50 per cent of the time in a low state.

5.2.2 *Gaia* DR2

The *Gaia* DR2 (Gaia Collaboration et al., 2018) catalogue quotes a parallax of 4.6 ± 0.1 mas which results in a distance estimate of 216 ± 5 pc.

5.2.3 Broad band photometry

Since its CRTS discovery in 2009, V808 Aur has been a popular target for the AAVSO and there are 44,164 observations available in their public archive. Arto Oksanen of the Hankasalmi observatory is a contributor to this archive, but has also sent his observations as a private communication for publication in this thesis. The
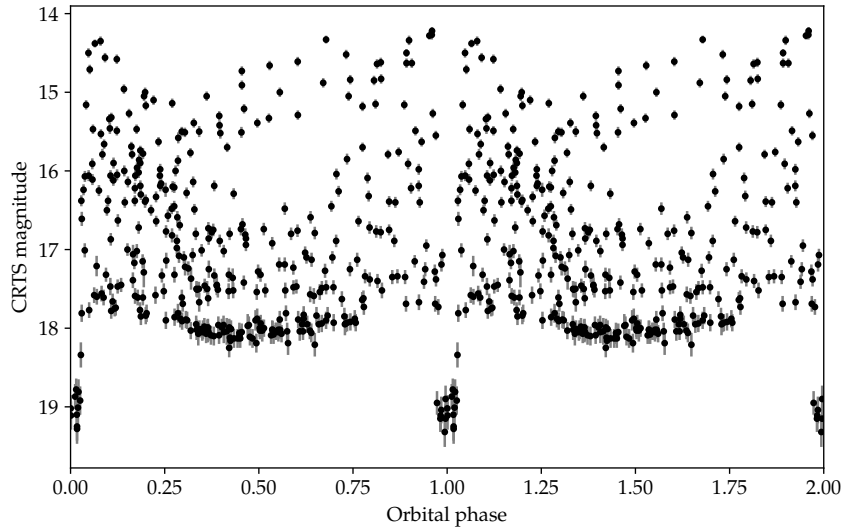
Figure 5.2: Phase folded CRTS photometry using the ephemeris in equation 5.3. Apart from the eclipse at phase 1.0, there is clear evidence of a least two distinct flux states, low and high. The low state shows a solid curve in the phases away from the eclipse implying no flickering and hence very little (or zero) accretion flow.

observatory uses a broad 'white light' filter and a CCD camera that has quantum efficiency that exceeds 50 per cent from 4800–7000 Å. These observations, in Figs. 5.3 and 5.4, are the most recent that we have available and cover the period from December 2018 to February 2020. During this period it appears that V808 Aur has maintained its low state and, in fact, moved to an extreme low state from December 2019 with its current brightest phase (near to the primary eclipse) at V=17. It is likely that this low state has been observed before and evidence is provided by the CRTS photometry in Fig. 5.1 at around JD 2454500 or about 12 years before the current observations.

5.2.4 High speed photometry

Eight nights of photometry were obtained using ULTRASPEC (Dhillon et al., 2014), mounted on the 2.5m Thai National Telescope from 2014 to 2017. Exposure times varied from 1.6 to 3.6 seconds depending on the conditions of the night. For the first three observations the Sloan g filter was used and for the last three observations the KG5 filter was used. The KG5 filter has a broad optical passband stretching from $\simeq 3500$ to $\simeq 7000$ Å and was chosen to allow the maximum light throughput while avoiding contamination from the M-dwarf companion. The KG5 filter is described in Dhillon et al. (2014) and the appendix of Hardy et al. (2017). All of the data were reduced using the ULTRACAM reduction pipeline. As a reference, we used a
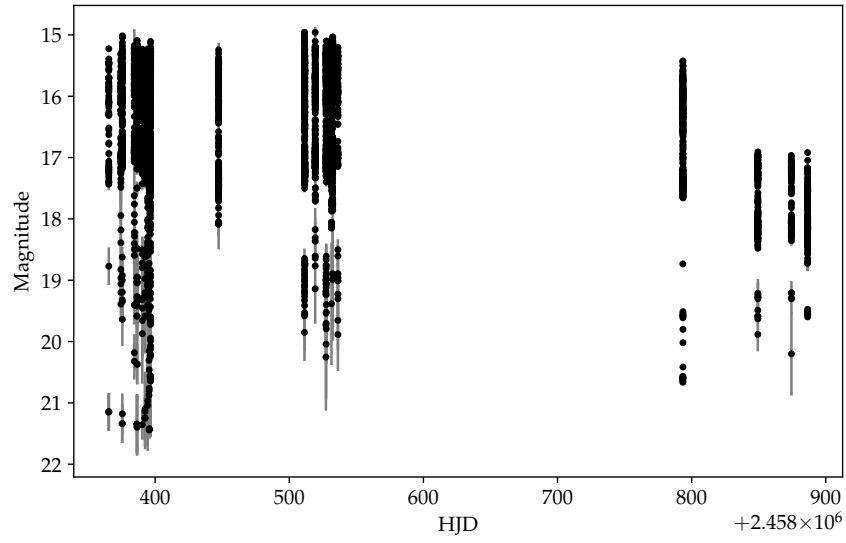
Figure 5.3: Recent photometric data of V808 Aur taken at the Hankasalmi observatory for V808 Aur. Data starts in September 2018 with the most recent observations taken in December 2019 and February 2020. No high states have been seen in the data during this period and the target now appears to be in an extremely low state with its maximum at magnitude 17. Observations were taken with a 'white light' filter.
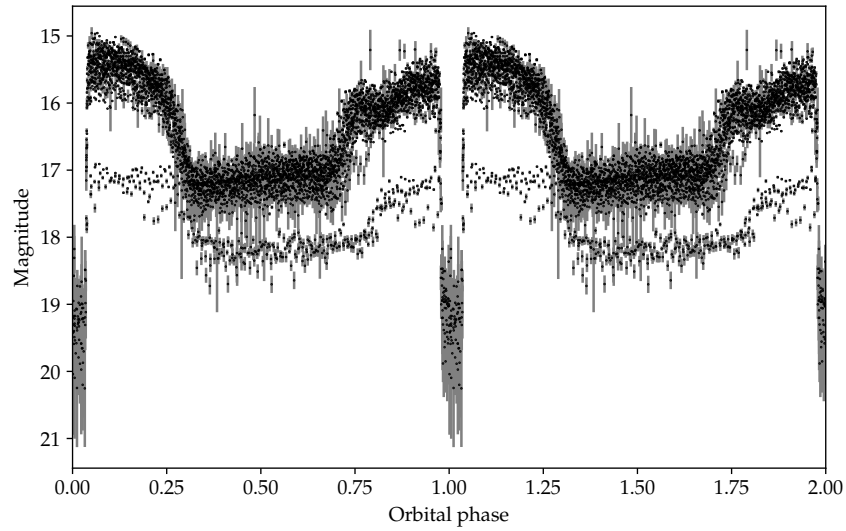
Figure 5.4: The phase folded depiction of the data shown in Fig. 5.3. The last two observations are those that appear lower on the plot. These data have not been offset and show that the target is now in an extremely low state.

Table 5.1: Photometry used in this study. The instrument used was ULTRASPEC, mounted on the 2.5m Thai National Telescope at the Thai National Observatory.

Date	BJD	Filter	$T_{\exp}(s)$	Total time (min)
2014/02/06	2456695	Sloan g	1.6	147.8
2014/02/07	2456696	Sloan g	1.7	166.2
2014/02/08	2456697	Sloan g	2.8	73.6
2014/12/12	2457004	KG5	3.6	95.1
2015/01/01	2457024	KG5	2.0	118.2
2015/01/03	2457026	KG5	2.0	131.1
2016/03/11	2457459	KG5	5.4	89.5
2017/02/03	2457808	KG5	2.2	111.8

comparison star located about 35 arcsec to the west and located at right ascension $07\,\mathrm{h}\,11\,\mathrm{m}\,23\,\mathrm{s}$, declination $+44°04'13''$(J2000). The details for these nights are shown in Table 5.1.

5.2.5 Phase resolved spectroscopy

V808 Aur was observed on two separate nights. In 2009 February when it was in a low state and then again in December 2014 during a high state. On both nights the target was observed using the ISIS dual-beam spectrograph on the William Herschel Telescope in La Palma. On 2009 February 2, 17 spectra were taken in the optical region, spanning a wavelength range of $4200 - 8800\,\text{Å}$. The ISIS blue arm was fitted with R1200B grating and set at a central wavelength of $4600\,\text{Å}$ with a resolution of $0.45\,\text{Å}\,\mathrm{pixel}^{-1}$. The ISIS red arm was fitted with R316R grating set at a central wavelength of $7100\,\text{Å}$ and a resolution of $1.85\,\text{Å}\,\mathrm{pixel}^{-1}$. On 2014 December 23, six spectra were obtained covering a wavelength range of $3200 - 9200\,\text{Å}$. The ISIS blue arm was fitted with the R300B grating, set to a central wavelength of $4300\,\text{Å}$ with a resolution of $1.73\,\text{Å}\,\mathrm{pixel}^{-1}$. The ISIS red arm was fitted with R158R grating set at a central wavelength of $7290\,\text{Å}$ and a resolution of $3.64\,\text{Å}\,\mathrm{pixel}^{-1}$. In all cases pixels were binned by a factor of two in the spatial direction.

5.2.6 X-ray fluxes

V808 Aur is not a ROSAT source, but it appears in the Swift X-Ray Telescope Point Source Catalogue (Evans et al., 2014). It was detected at $3.36^{+0.83}_{-0.72} \times 10^{-3}\,\mathrm{cts\,s^{-1}}$ in the full 0.3-10 keV band. The hardness ratio for medium to soft is given as -0.080 and for hard to medium as 0.174. Swift classifies hard X-rays in the 2–10 keV range, medium are 1–2 keV and soft 0.3–1 keV. The XMM-Newton observations of Worpel

and Schwope (2015) conclude that there is a second accretion spot on the far-side of the white dwarf. They also suggest that the phase of bright X-rays shifts when V808 Aur moves from a high state to a lower state.

5.3 Analysis

5.3.1 Photometric behaviour

As noted in previous observations our new light curves display strong flickering variability and a steep-sided eclipse (Fig. 5.5). Schwope et al. (2015) finds pre-eclipse dips at phase 0.86 when V808 Aur is in the high state, and later, at phase 0.89 in the intermediate state. Our photometric data was taken during a low state and we did not expect to see any pre-eclipse dips. Indeed, we find no evidence of this phenomenon in any of our eight light curves. In the high state, Schwope et al. (2015) notes that the eclipse profile shows a gradual descent to minimum after an initial drop (see their Fig. 7). This is explained by a model where the accretion spot is eclipsed, but, since the target is in a high state, the accretion stream is still visible over the eclipsing limb of the secondary and is only gradually eclipsed as represented in their Fig. 11. Once again, since our photometry was taken in a low state, we do not see this phenomenon and all of our eclipse profiles have flat bottoms, see Fig. 5.6.

5.3.2 Eclipse timings

The primary eclipse was observed nine times on eight different nights. We converted all eclipse times to barycentric dynamical time (TDB) in Julian days as measured at the solar system's barycentre.

We determined the eclipse times with a least-squares fit of a function to the eclipse profile. The function was composed of a sigmoid and a straight line of the form,

$$f = \frac{a_1}{1 + e^{-a_2(t-a_3)}} + a_4 + a_5(t - a_3) \tag{5.1}$$

where f and t are the flux measurements and timing of our observations respectively and a_1 to a_5 are the fit parameters with a_3 being the time at which ingress or egress occurs.

In order to measure the centre of the eclipse, we fitted this function to both the ingress and the egress for each eclipse and then used the mid-point between these two values as our eclipse time. Using this method we measure the eclipse ingress
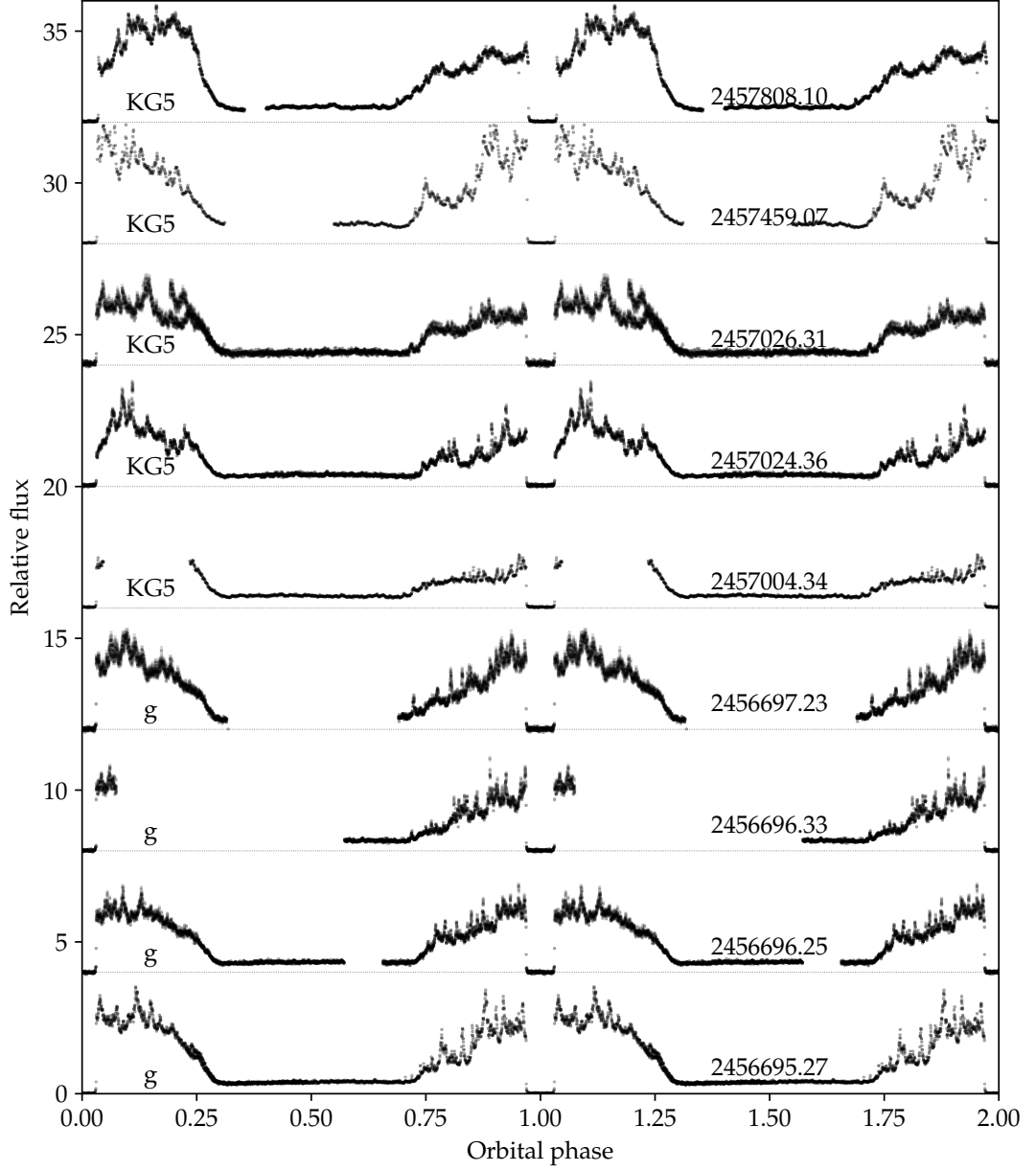
Figure 5.5: The TNT light curves of V808 Aur. Exposure lengths vary from 1.6 to 3.6 seconds. The brightness of the target is measured as the fractional counts relative to the comparison star (described in the text). The observations were taken with either the Sloan g filter or the KG5 filter as indicated on the figure. Each orbit is offset vertically by four units.
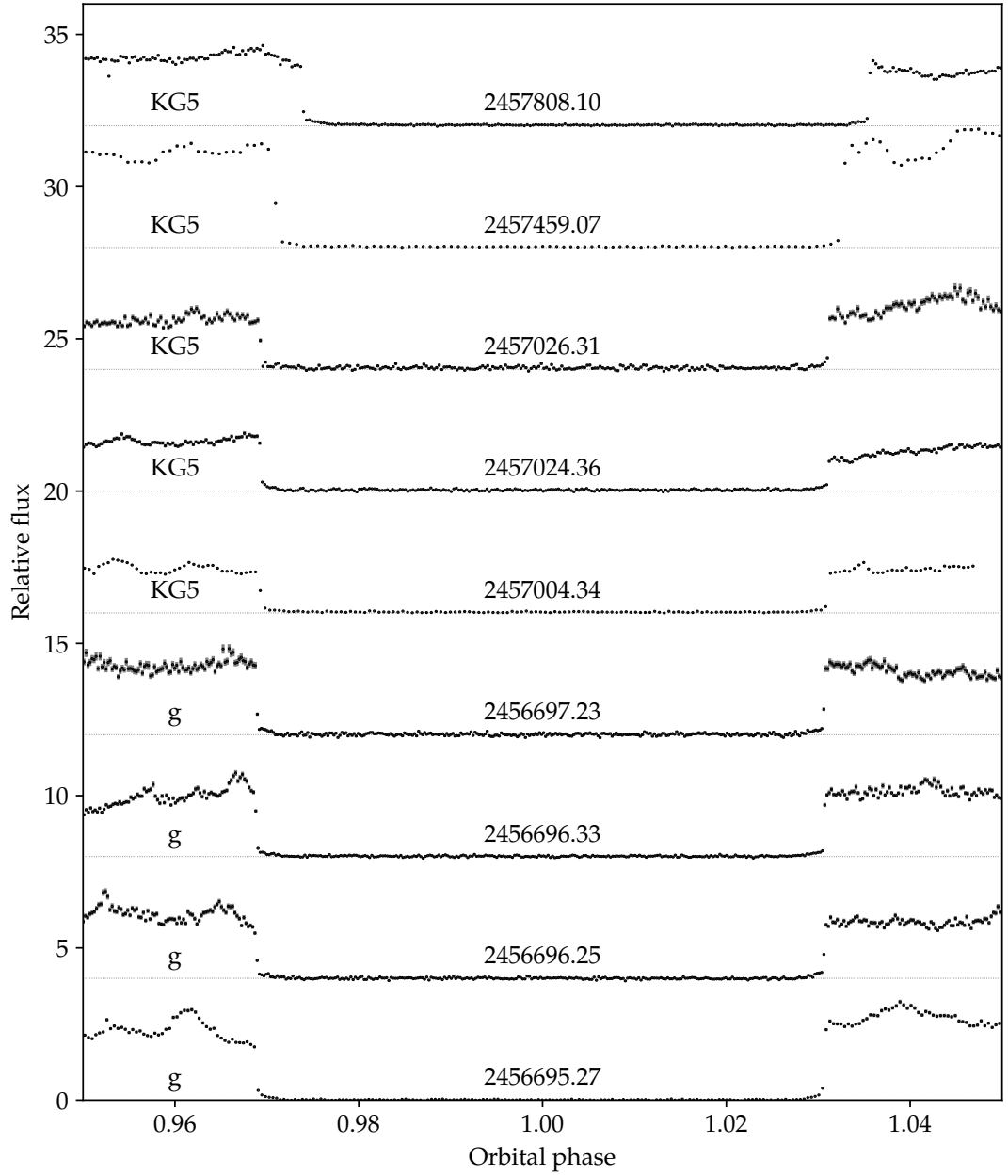
Figure 5.6: The eclipse profiles of all nine of the eclipses recorded at the TNT. The flux ratio is the counts for the target star compared to counts for our comparison (as described in the text). Each eclipse is shown with the BJD corresponding to the centre of the eclipse. Two eclipses were observed on the night of 2014 February 7 (BJD 2456696). Each light-curve is offset vertically by four units.

Table 5.2: Details of the 7 primary eclipses. Ingress, egress and centre of eclipse times are shown as time since start of BJD.

BJD	Ingress		Egress		Centre	Duration
(d)	(d)	(phase)	(d)	(phase)	(d)	(s)
2456695	0.269480	0.96889	0.274504	0.03063	0.2719921	434.1(0.3)
2456696	0.245999	0.96886	0.251026	0.03063	0.2485129	434.4(0.2)
2456696	0.327374	0.96884	0.332403	0.03064	0.3298889	434.5(0.1)
2456697	0.222525	0.96891	0.227548	0.03064	0.2250372	434.0(0.2)
2457004	0.338635	0.96929	0.343661	0.03105	0.3411487	434.3(0.2)
2457024	0.357335	0.96935	0.362353	0.03101	0.3598445	433.6(0.3)
2457026	0.310374	0.96929	0.315401	0.03107	0.3128882	434.3(0.3)
2457459	0.072377	0.97088	0.077396	0.03256	0.0748873	433.6(0.5)
2457808	0.097755	0.97385	0.102769	0.03547	0.1002622	433.1(0.3)

and egress times to a precision of 0.3 seconds. All eclipse timings are reported in Table 5.2.

Small and medium-sized telescopes have taken photometry of the system dating back to late 2008. These observations were compiled and reported by Schwope et al. (2015). Schwope revised the original ephemeris that was published by Thorne et al. (2010). The ephemeris given by Schwope is

$$\text{BJD(TDB)} = 2454833.207868(14) + E \times 0.0813768094(6) \tag{5.2}$$

but since our observations have been taken with instruments operating at a much higher time resolution than the sources used by Schwope, we have re-computed the ephemeris by combining our own eclipse times with those documented in the Schwope paper. Our recomputed ephemeris is

$$\text{BJD(TDB)} = 2454833.207854(12) + E \times 0.0813768096(5) \tag{5.3}$$

An O-C plot is shown in Fig. 5.7 with the new eclipse times indicated by green markers. Our newer observations reveal a departure from a linear ephemeris and we have fitted a quadratic term of 8.698×10^{-8} s cycle^{-2} or 1.24×10^{-11} s/s. The light curves for all of our high time resolution photometry are shown in Figs. 5.5 and 5.6.

Departure from a linear ephemeris has been noted in other polars. Bours et al. (2014) examined a similar phenomenon in HU Aqr. The Applegate mechanism (Applegate, 1992) has been proposed as a possible explanation for changes in the orbital period. This mechanism entails changes in mass distribution within the secondary caused by magnetic cycles. The result is a modification of the quadrupole
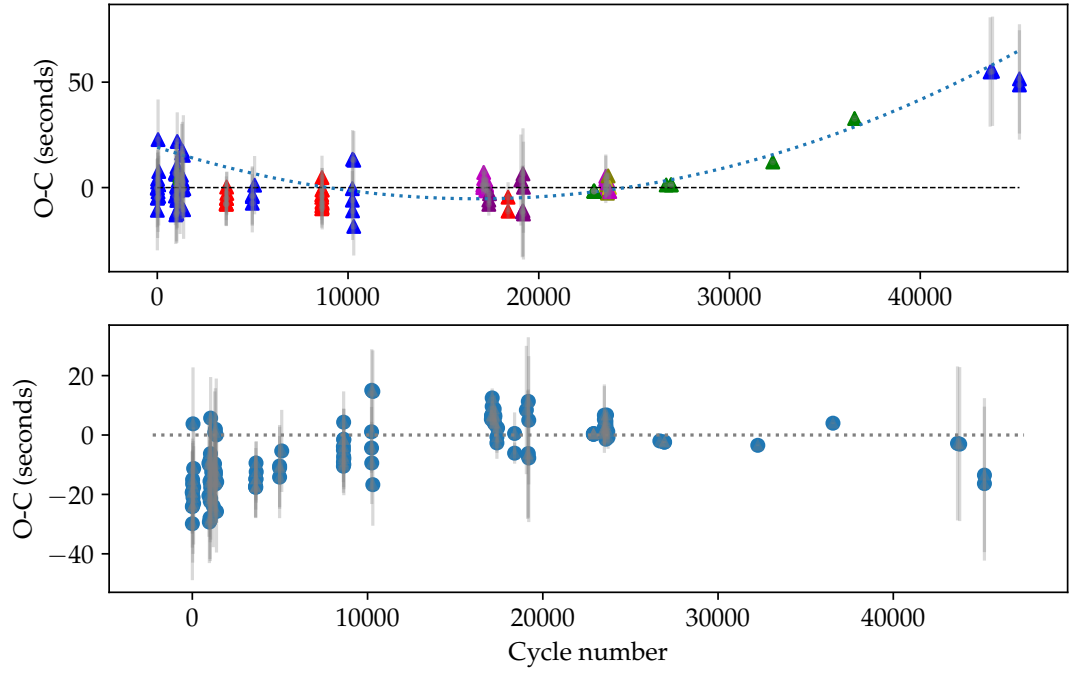
Figure 5.7: The observed minus calculated times for all of the eclipse data as reported by Schwope et al. (2015) with our TNT observations indicated by the green markers and additional data from the Hankasalmi observatory in blue. The lower panel shows the residuals relative to the fit.

moment and its moment of inertia. Since the secondary is tidally coupled to the overall binary system, this alters the binary period. For HU Aqr, the energy required to redistribute mass within the secondary is an order of magnitude larger than the luminosity of the star during the time span over which the period changes (Schwarz et al., 2009) suggesting that the Applegate mechanism is unlikely to be the cause of the period change. Lanza (2006) generalised Applegate's model to binary systems with late-type secondaries and again demonstrated the energy deficit. Further eclipse timing of HU Aqr show that the O-C trend is continuing and a satisfactory explanation is still being sought, see Schwope and Thinius (2018) and references therein.

The changes we see for V808 Aur are of similar amplitude and the donor star is of a similar spectral type. Other possible explanations include the presence of one or several other circumbinary objects and this has already been put forward by Schwope et al. (2015) even before any departures from a linear ephemeris were detected. Since the orbital period of this object is likely to be longer than tens of years, an extension of our timebase is required to confirm or rule out this possibility. It should be noted that, although there are many compact binaries exhibiting this kind of behaviour (Parsons et al., 2010), only one, NN Ser, has had eclipse times correctly predicted by a model of circumbinary planets (Marsh et al., 2014; Beuermann et al., 2013; Horner et al., 2012) and it needed two planets to fit the data. Other possible explanations for period changes are still being considered for NN Ser (Marsh et al., 2014). Unlike HU Aqr, the measured period change for V808 Aur is a positive one, meaning that the period is getting longer which is puzzling. Nevertheless, if the orbital separation *is* increasing, it would agree with the apparent accretion rate slowing as the system appears to be in an extended state of low activity. Our detection of this change in period is still tentative, so follow up observations are required.

5.3.3 Estimating the magnitude of the white dwarf

Close examination of the eclipses reveals a short and shallow but noticeable slope just after ingress and just before egress. If we assume that this slope is caused by the gradual eclipse of the white dwarf's photosphere, and that the steep, sharp incline is due to the accretion spot, then we can try to estimate the contribution of the white dwarf by measuring the small contribution in these phases. In Figs. 5.9 and 5.10 we show eclipse data from the night of JD 2456697.23. For this night, we were able to use a second, brighter comparison star in our field of view. This brighter comparison was found in the APASS catalogue (Henden et al., 2015) with a measured g band

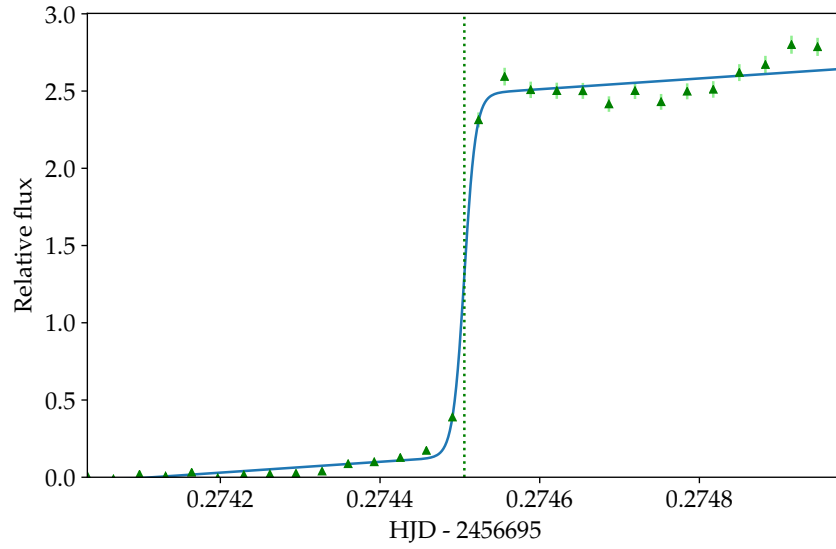Figure 5.8: An example of the sigmoid fitting method applied to an egress of the primary eclipse. The vertical dashed line shows the fitted value of the egress time. A complete list of these times for all of the eclipses observed at the TNT is listed in Table 5.2.
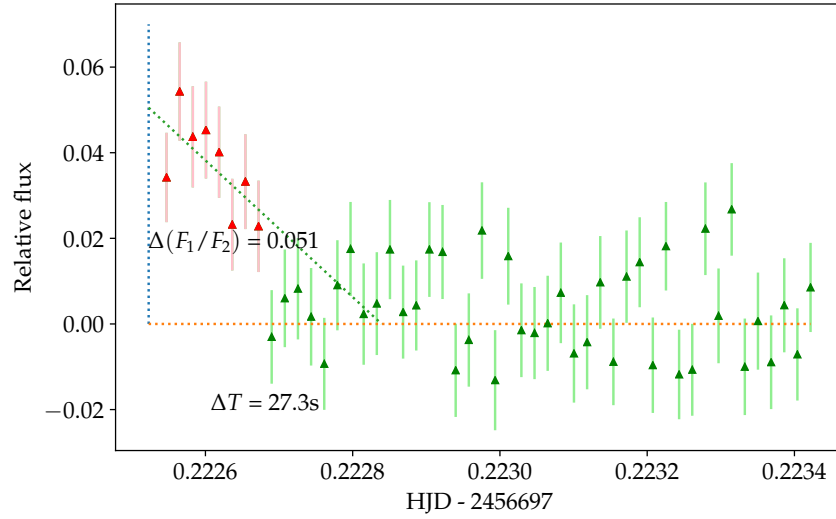

Figure 5.9: Measuring the contribution of the white dwarf's photosphere to the overall flux by examining the data immediately after ingress.
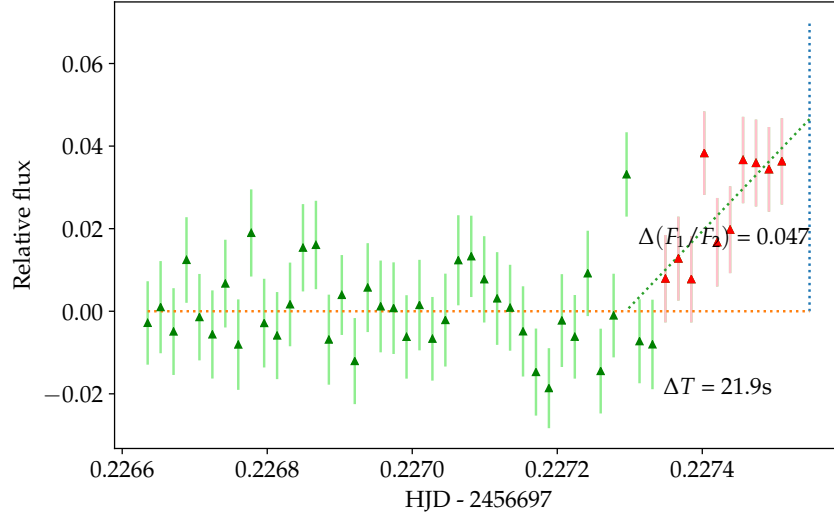
Figure 5.10: Measuring the contribution of the white dwarf's photosphere to the overall flux by examining the data immediately before egress.

magnitude of $g = 15.47$. In order to determine the flux contribution from the white dwarf we fit a straight line to the sloped section and measured where this line intersects the time of the fitted ingress/egress (as measured in the previous steps) and also where it intersects the x-axis. These two intersections give us an estimate of the contribution to the overall flux by the white dwarf photosphere and the time it takes to eclipse this portion of the face of the disk. If we assume that the accretion spot is directly facing the secondary then this time corresponds to eclipsing 50 per cent of the face of the white dwarf. The mean measured values for ingress and egress on the light curve of JD 2456697.23 are $\Delta(F_1/F_2) = 0.049$ and $\Delta T = 24.6$ s. The total contribution from a full disc will be double the measured value, or $\Delta(F_1/F_2) = 0.098$. Therefore the incremental magnitude of the white dwarf over our comparison star's flux is $m_1 - m_2 = -2.5 \log(0.402)$ or $m_1 - m_2 = 0.989$. Using the APASS magnitude for our comparison star $g = 15.47$ and this gives us a $m_\mathrm{g} = 17.99$ for the white dwarf. In order to get the absolute magnitude, one can use $M_\mathrm{g} = m_\mathrm{g} + 5 - 5 \log(d)$, with the distance of $d = 216$ pc and hence $M_\mathrm{g} = 11.31$. By consulting the white dwarf cooling models from Bergeron[1], which are based on models from Fontaine et al. (2001) we can use this magnitude and an estimate of the mass (as calculated in section 5.3.6) to look up an effective temperature of $T_\mathrm{eff} = 20,000$ K for a pure H atmosphere white dwarf. Araujo-Betancor et al. (2005) presented far-ultraviolet spectra of eleven polars and showed the temperature of the white dwarf to range from 10800 to 14300 K. It is possible that our measurement of

---

[1] http://www.astro.umontreal.ca/~bergeron/CoolingModels

the contribution of the photosphere is an overestimate, since we cannot be certain that the accretion stream is not also contributing to the flux during this time.

We can also use the measured value of the time taken for this white dwarf eclipse to occur as twice the value of the measured time (for a full disc eclipse) or $\Delta T = 49.2\,\text{s}$. In section 5.3.6 we measured projected orbital velocity of the secondary as $K_2 = 425\,\text{km}\,\text{s}^{-1}$. This results in a maximum diameter for the white dwarf of 20,910 km or $R_{\text{WD}} = 0.015\,\text{R}_\odot$. This calculation does not take into account the overall relative velocity of both bodies since it (incorrectly) assumes that the white dwarf is stationary with respect to the centre of mass of the system. Since the inclination of the system is not 90°, this represents an upper limit to the white dwarf radius.

5.3.4   Average spectra

Our two nights of optical spectra were taken 5 years apart, 2009 February in a low state and 2014 December in a high (or intermediate) state, see Fig. 5.11. In the 2009 spectra, we see much weaker Hα emission and only barely detectable Hβ while the data taken in 2014 show strong Balmer emission from Hα to H10 and He I (4471, 5875 Å), He II (4686 Å) and Ca II (3933, 3968 Å). Also, there is much reduced blue continuum in the 2009 data.

5.3.5   Donor star spectral type

In order to determine the spectral type of the M-dwarf, a spectrum taken during primary eclipse was matched to templates of M-dwarfs M0 to M9 taken from the Sloan Digital Sky Survey (SDSS) catalogue (Bochanski et al., 2007). A careful choice of the exposure timing ensured that we had a 300 s exposure taken entirely within the 433 s primary eclipse. The spectrum taken centred on phase 0.99 and ran from phase 0.97 to 1.01 and we can conclude that it is a spectrum of the M-dwarf only. We fitted this spectrum to the template spectra by normalising the flux to match that of our target spectrum in the range of 6950 – 8000 Å and then scaling the template by a constant that would minimise the χ^2 between the two. Our best fit spectrum is that of an M4-type main sequence star and this fit is shown in Fig. 5.12. Knigge (2006)'s theoretical sequence of secondary donors give a spectral type of M4.4 for a 2 hr orbital period CV.

Wade and Horne (1988b) describe a method of determining the spectral type of the M-dwarf companion using the relative strength of the TiO features. The idea is that, although equivalent widths of TiO features cannot be used directly since
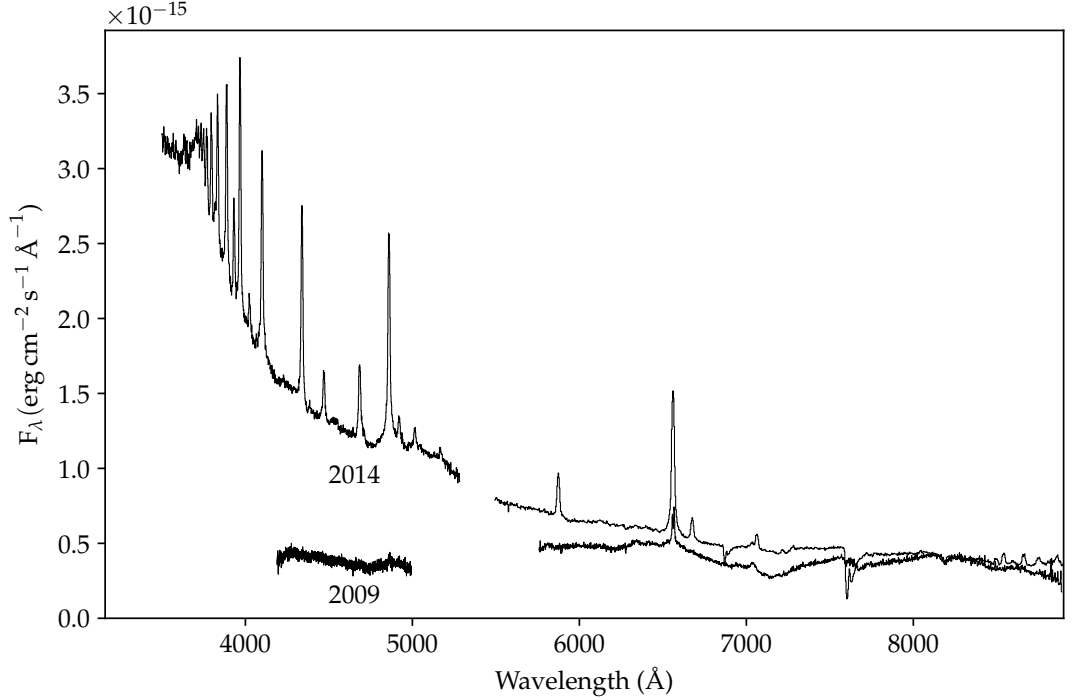
Figure 5.11: The average spectra taken in 2009 and 2014 with ISIS at the WHT. No offsets have been applied to the data.

they are affected by the white dwarf and disc features (in our case, the dominant contaminant is the flux from the cyclotron radiation), however the flux deficit ratio relative to a reference continuum are not affected. This method uses the following flux density measurements,

$$d_\nu(\lambda 7165) = \frac{\int_{7140}^{7190}[c_\nu(\lambda) - f_\nu(\lambda)]d\lambda/\lambda}{\int_{7140}^{7190} d\lambda/\lambda} \tag{5.4}$$

$$d_\nu(\lambda 7665) = \frac{\int_{7640}^{7690}[c_\nu(\lambda) - f_\nu(\lambda)]d\lambda/\lambda}{\int_{7640}^{7690} d\lambda/\lambda} \tag{5.5}$$

where $c_\nu(\lambda)$ is derived by fitting a least-squares straight line to the observed flux $f_\nu(\lambda)$ in the continuum bands at $7450 - 7550\,\text{Å}$, $8130 - 8170\,\text{Å}$ and $8222 - 8262\,\text{Å}$.

The dimensionless parameters $\frac{d_\nu(\lambda 7665)}{c_\nu(\lambda 7665)}$ and $\frac{d_\nu(\lambda 7665)}{d_\nu(\lambda 7165)}$ were calculated for the spectrum taken at phase 0.99 (during the primary eclipse) as 0.4 and 0.9 respectively, placing the spectral type of the M-dwarf as M4 according to Table 3 in Wade and Horne (1988b). This is in agreement with our match to the SDSS template spectra.

109
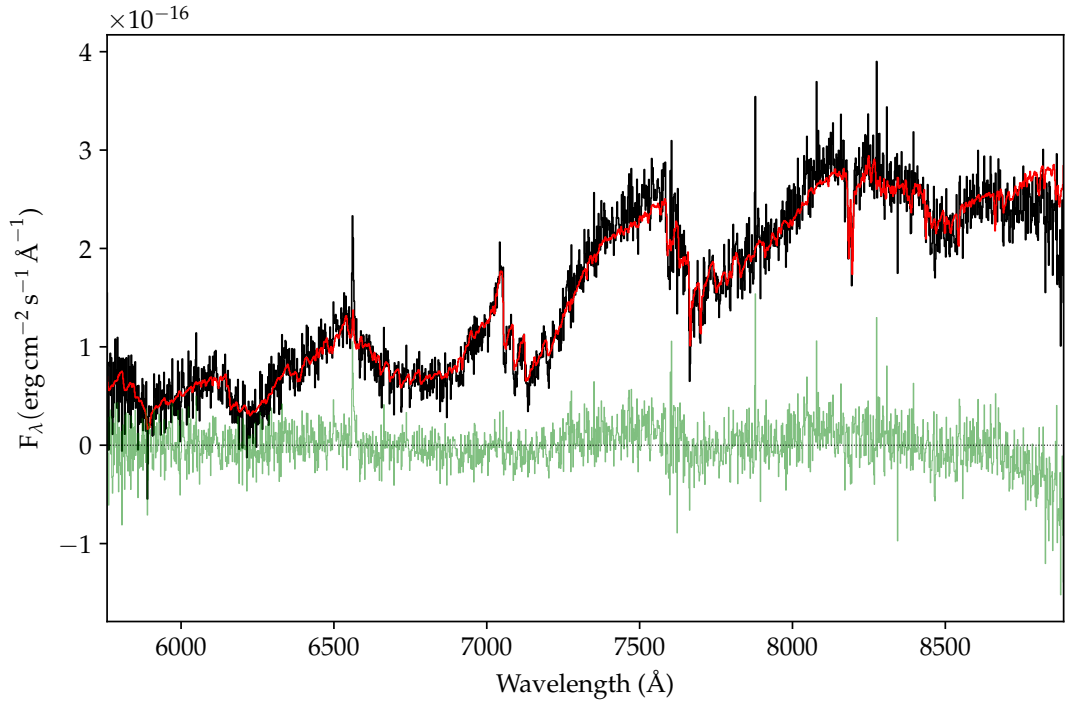
Figure 5.12: The spectrum taken at phase 0.9975 (during primary eclipse) shows the secondary without contamination from the white dwarf or the accretion stream. The spectrum was fitted to a list of SDSS template spectra and the best match was an M4 main sequence star. Our observed spectrum is in black with the best fit overlaid in red and our residuals in green.
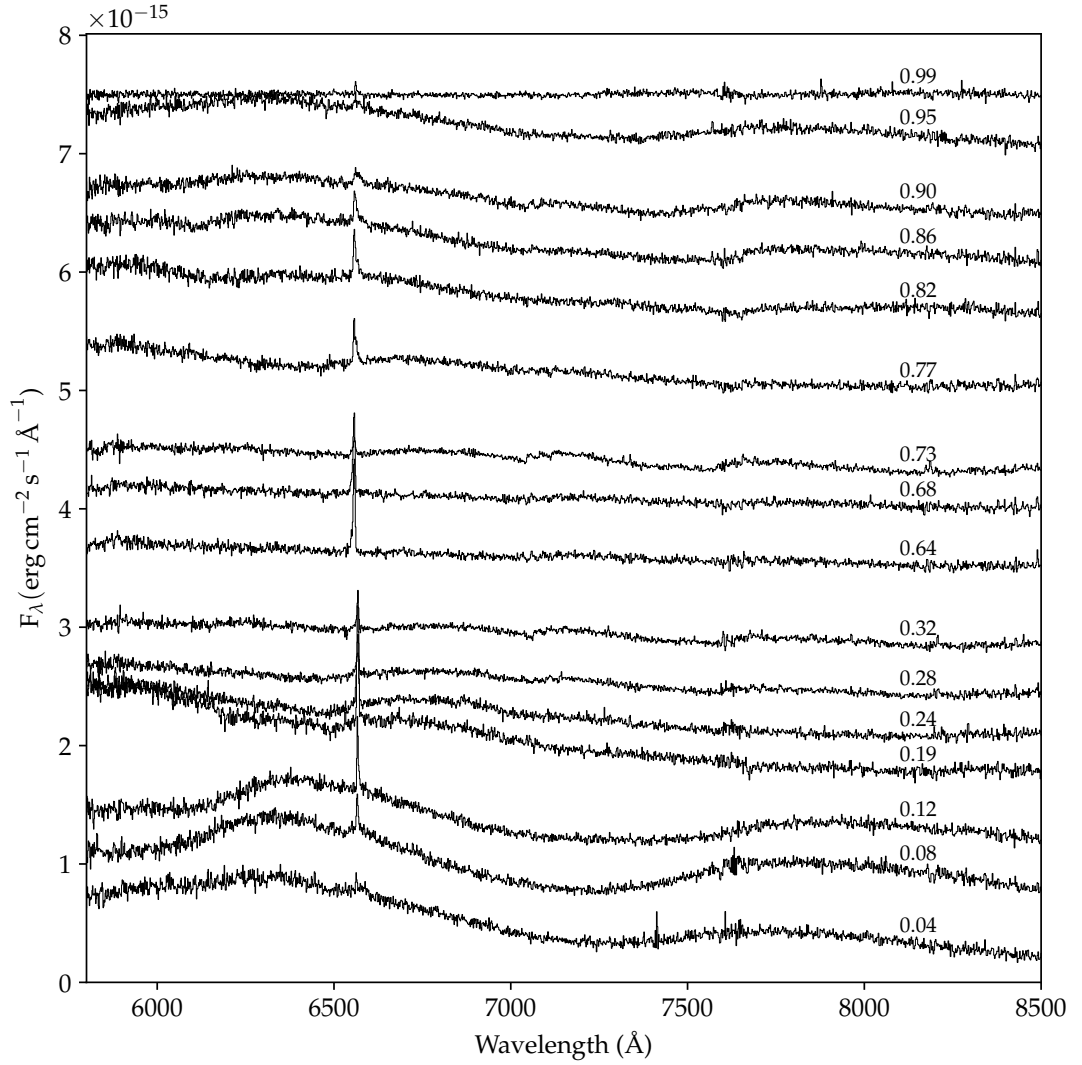
Figure 5.13: The ISIS red arm spectra taken during the low state after subtraction of a template M4 spectrum. The labels show the orbital phase. The top most spectrum was taken during the primary eclipse and is therefore the residual after subtraction as shown in Fig. 5.12.
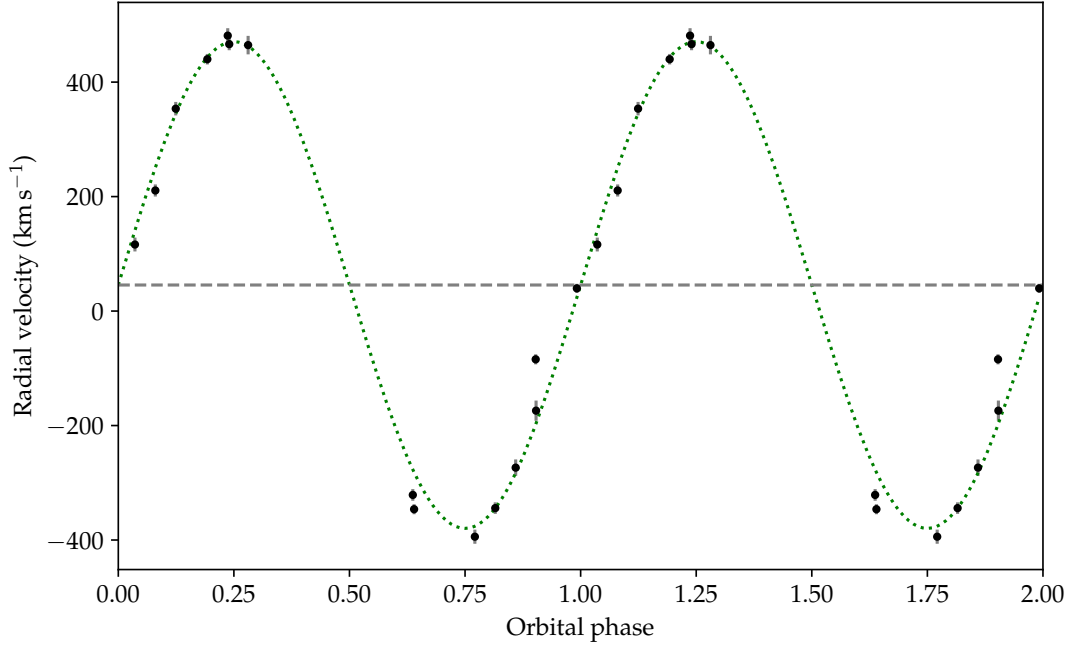
Figure 5.14: The projected radial velocity of the secondary, as a function of orbital phase. The velocity was measured by fitting a double-Gaussian function to the Na I doublet at 8190 Å.

5.3.6   Radial velocity of the secondary

Many of the time resolved spectra taken during quiescence show a clear Na I doublet at 8183 and 8194 Å. This feature is assumed to be associated with the photosphere of the M-dwarf companion. For those spectra (18 of 22) where we had a clear detection of this doublet, we fitted a double Gaussian using a least squares approach. The fitting function took the form of,

$$f_\lambda = a_0 + a_1 e^{-\frac{1}{2}(\frac{\lambda - a_2}{a_3})^2} + a_4 e^{-\frac{1}{2}(\frac{\lambda - (a_2 - \delta)}{a_3})^2} \tag{5.6}$$

where f_λ is the measured flux at the wavelength, λ. During the least squares convergence we kept the separation δ fixed at 11 Å; the depth of the lines a_1 and a_4 free to vary but kept equal to each other and the width of the lines a_3 fixed to 3.4 Å. The fitted wavelengths were converted to radial velocities and we fitted a sinusoid to the result. The period was fixed to the known orbital period as determined from photometry and quoted in equation 5.3. The fitted radial velocities are shown in Fig. 5.14 and have a semi-amplitude of $425 \pm 17\,\mathrm{km\,s^{-1}}$ and a γ velocity of $45 \pm 12\,\mathrm{km\,s^{-1}}$.

The mass function for a compact binary system is given by,

$$\frac{(M_1 \sin i)^3}{(M_1 + M_2)^2} = \frac{P_{\text{orb}} K_2^3}{2\pi G}, \tag{5.7}$$

If we assume a mass of $0.155\,\text{M}_\odot$ for the companion star of type M4 (from the Knigge et al. (2011) donor star sequence), with $P_{\text{orb}} = 1.95\,\text{hr}$ and using the mass function with an inclination $i = 81.5 \pm 2.2°$ from Schwope et al. (2015), this would at imply a mass for the primary component of $M_1 = 0.90 \pm 0.09\text{M}_\odot$ which seems inconsistent with the large radius we derived for the white dwarf in section 5.3.3. The error shown is propagated from our measurement errors of $\sin i$ and K_2, but the largest uncertainty will be in the mass of the secondary component, M_2, which is taken from the theoretical sequence given in Knigge et al. (2011). The mass ratio here is $q = 0.172$. Using the same method as described in chapter 4 to derive a q value from the Roche geometry and the phase length of the primary eclipse, $\Delta\phi = 0.0616$ and the inclination (again from Schwope) of $i = 81.5°$, we can estimate a q value of 0.205. While these values are not entirely in agreement, we may have underestimate the mass of the secondary. A higher mass of, say $M_2 = 0.19\,\text{M}_\odot$ substituted back into equation 5.7 would result in $M_1 = 0.94\,\text{M}_\odot$ and $q = 0.202$.

5.3.7 Magnetic field strength

For the phases near to the eclipse, when the accretion spot is in view, there is clear evidence of cyclotron humps (see Fig. 5.13). In order to estimate the magnetic field strength we measured the positions of consecutive maxima of these humps and calculated the corresponding field strength using the formula,

$$B = \frac{2\pi m_e c}{e} \left(\frac{1}{\lambda_1} - \frac{1}{\lambda_2} \right), \tag{5.8}$$

where λ_1 and λ_2 are the wavelengths of consecutive maxima.

Although we examined all spectra taken in both runs (2009 and 2014), only six of those taken in 2009 during quiescence that showed easily measurable cyclotron humps. Using the equation above to give an initial estimate for the field strength as $B \simeq 34\,\text{MG}$. Once we had this estimate we could revert to a simplified version of the equation for cyclotron frequency,

$$B = \frac{2\pi m_e c}{e} \frac{1}{n\lambda}, \tag{5.9}$$

where n is the harmonic number of the cyclotron hump. Using this formula we
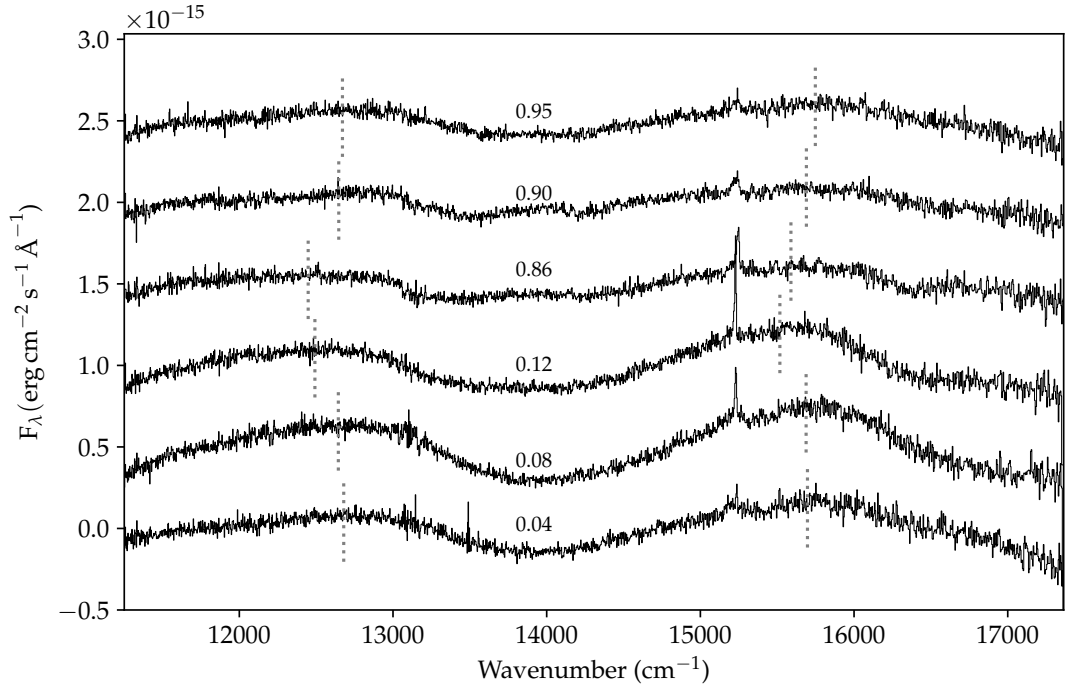
Figure 5.15: Our fits to the cyclotron humps seen in the red arm of ISIS for those six spectra that clearly demonstrated this phenomenon. All spectra have had the underlying spectrum of the fitted M-dwarf and also a simple straight line subtracted to level the continuum. The vertical dotted lines show our peak frequency as determined by fitting a quadratic to each of the humps. The left hump is the fourth harmonic of the fundamental cyclotron frequency and the right is the fifth. Each spectrum is labelled with the orbital phase.

discovered that the two humps are the fourth and fifth harmonics of the cyclotron frequency. We converted the wavelength scale into a frequency scale by using the reciprocal wavelength or wavenumber (in cm^{-1}) and subtracted a fitted straight line to level the continuum before fitting a quadratic to each of the two humps in each spectrum, see Fig. 5.15. The peak of this quadratic was taken as the cyclotron frequency and used to compute the field strength. These values are listed in Table 5.3. As is predicted by models of this radiation, we can see our measured field strength declining as we leave phase zero. As our viewing angle θ increases, the observed frequency declines since it depends on the reciprocal of $\sin \theta$ and $\sin^2 \theta$, see equation 4 of Cropper et al. (1989). The opposite effect is seen when approaching phase zero from the other side of the orbit.

Kolbin et al. (2019) also used optical spectra to measure the field strengths and combined observations with theoretical models to determine a magnetic field strength of the two accreting poles to be $B_1 = 38.2 \pm 0.8 \, \text{MG}$ and $B_2 = 51 \, \text{MG}$.

Table 5.3: Field strengths calculated by measuring the peak wavelengths of subsequent cyclotron humps as defined in equation 5.9 for the phases where our spectra showed clear evidence of these phenomena.

Phase	λ_4 (Å)	λ_5 (Å)	B_4 (MG)	B_5 (MG)
0.04	7887	6371	33.95	33.62
0.08	7909	6374	33.85	33.60
0.12	8005	6444	33.45	33.24
0.86	8033	6415	33.33	33.39
0.90	7907	6374	33.86	33.61
0.95	7892	6350	33.93	33.73

They obtained a temperature estimate for the accretion spot inner facing accretion spot to be $kT = 18 - 27\,\text{keV}$.

5.4 Conclusion

While V808 Aur has been the subject of several studies in the time since the discovery during a high state in 2009, most of these have been focused on the photometry (Schwope et al., 2015) and X-ray observations (Worpel and Schwope, 2015). Although Kolbin et al. (2019) used optical spectra to measure the magnetic field strength of the accretion poles, they did not use these data to determine orbital parameters of the system. By examining features of the secondary and determining its projected radial velocity, we have been able to make an estimate of the masses of both components in V808 Aur as $M_1 = 0.90\,\text{M}_\odot$ and $M_2 = 0.155\,\text{M}_\odot$. By fitting a spectrum taken during primary eclipse to a template library, we have established the spectral type of the donor as M4.

Through deviations in the measured O-C times of the eclipses, Schwope et al. (2015) suggest that there is a chance of a sub-stellar third body orbiting the system with a putative mass of $M_{\text{pl}} \simeq 2\,\text{M}_{\text{Jup}}$. Our high speed observations, in combination with even more recent observations from smaller telescope, seem to confirm that there is a clear departure from a linear ephemeris. While one possible explanation is a third body in orbit with the system, other explanations such as the Applegate mechanism have been put forward. It is essential that we obtain more high speed observations of the eclipse over an extended period of time to confirm the evolution of ephemeris. Recent observations at the Hankasalmi observatory also show that V808 Aur is in an extended low state which, when combined with the CRTS and ASAS-SN archival data, leads us to conclude that has likely been the case for several

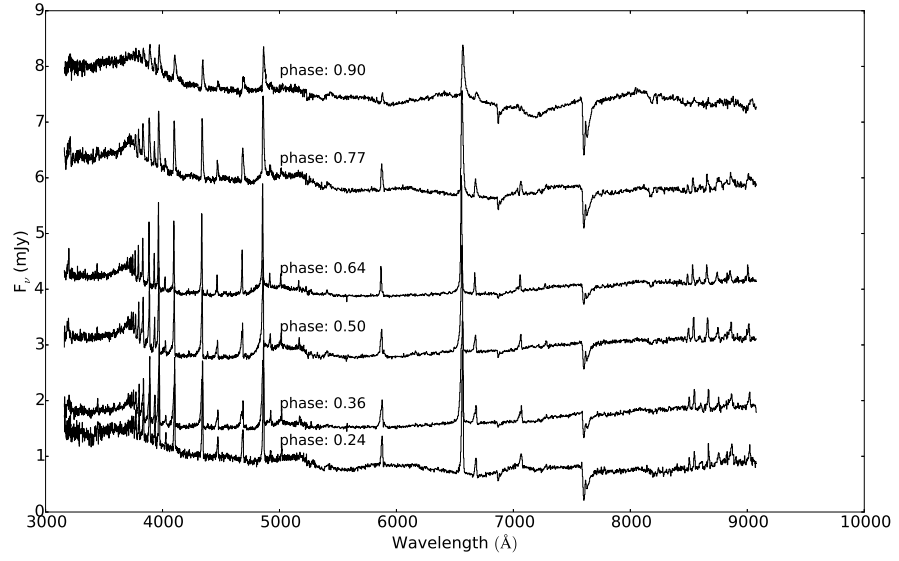Figure 5.16: ISIS blue arm spectra of V808 Aur taken at six stages of the orbital cycle during outburst in December 2014. Cyclotron humps are seen in the early and late stages of the orbit when the accretion spot is in view. During the mid-phases the accretion spot is eclipsed by the white dwarf.

years. If the orbit is truly widening, then this might be an explanation of the lower accretion rate.

Chapter 6

CRTS J215256.1+191658

6.1 Introduction

The CRTS survey, introduced in chapter 2, has detected $\sim 60,000$ periodic variables over its $\simeq 14$ year operation period (Drake et al., 2014b). This list includes CRTS J215256.1+191658 (hereafter, CRTS2152), position $21h\,52m\,56.1s +19°\,16'\,58''$(J2000). Drake et al. (2014a) also report the discovery of 855 CV candidates in their data archive, of which 137 have been spectroscopically confirmed. However, CRTS2152 did not appear in this particular list of CVs. In the larger catalogue its period is listed as 0.162975 days, with a CRTS mean magnitude of 17, amplitude of 1.36 magnitude and a classification as a PCEB. Examination of its light curve for an undergraduate project organised by Tom Marsh, noted it as a potentially interesting object. The phase folded CRTS light curve (Fig. 6.2) revealed a modulation that had a large scatter and evidence of an eclipse. It also suggested that CRTS2152 was probably subject to more than one luminosity state. CRTS2152 was added as a backup target to an observation run of ULTRASPEC on the NTT in June 2017. During the observation, it was immediately obvious that CRTS2152 was an eclipsing polar, with a deep flat-bottomed eclipse and a sudden egress followed by substantial flickering (Fig. 6.3 and Fig. 6.4). Following this discovery, additional follow up photometric and spectroscopic observations were carried out. This chapter presents a first look at this new polar.

6.2 Observations

6.2.1 Published survey photometry

CRTS2152 has several years of observations in the CRTS catalogue going back to 2005 April. The ASAS-SN survey (Shappee et al., 2014; Kochanek et al., 2017) begins coverage of CRTS2152 in 2012 November. Combined, these two sources provide a total time span of 13.6 years. We used these data in section 6.3.2 to compute an orbital period for the system. Inspection of the CRTS data suggests that CRTS2152's low state near magnitude 18 is rare and has only occurred once in the last 13 years, at approximately HD 2455500. However the cadence of the photometry does not rule out other episodes of this low state that may have gone undetected. It is interesting to compare this to the similar long term light-curve representation for V808 Aur in Fig. 5.1 which is seen to alternate between high, low and intermediate states and is now (apparently) in a prolonged low state. V808 Aur has a period of 1.9 hr and is below the period gap, while CRTS2152 has a period of 3.9 hr. Although it has been shown that some polars, like HU Aqr, see Harrop-Allin et al. (2001), can alter states from high to low within a cycle or two, there is no clear explanation of what the causes of prolonged high or low states are. Unlike the long term study of dwarf novae where, for some objects, such as U Gem and SS Cyg, we have light-curves extending for many tens of years (Warner, 1995), there is no comprehensive review of the behaviour of alternating states in polars, although monitoring projects have begun recently (Poyner, 2013).

6.2.2 *Gaia* DR2

The *Gaia* DR2 (Gaia Collaboration et al., 2018), catalogue quotes a parallax of 1.6 ± 0.12 mas which results in a distance estimate of 621 ± 44 pc.

6.2.3 High speed photometry

Two nights of photometry were obtained at the New Technology Telescope (NTT) in La Silla, Chile, using ULTRACAM mounted at the Nasmyth focus. Also, CRTS2152 was used as a test target during the commissioning HiPERCAM instrument at the 4.2m William Herschel Telescope (WHT). At the time, the u-band channel of HiPERCAM was not operational. For all of the reductions, the same nearby comparison star was used. This was 2MASS J2130165+1915033, which is located about 2.35 arcmin to the south-south-east of the target and has a g magnitude list in the SDSS catalogue of $g = 14.29$. The details for these nights are given in Table 6.1.
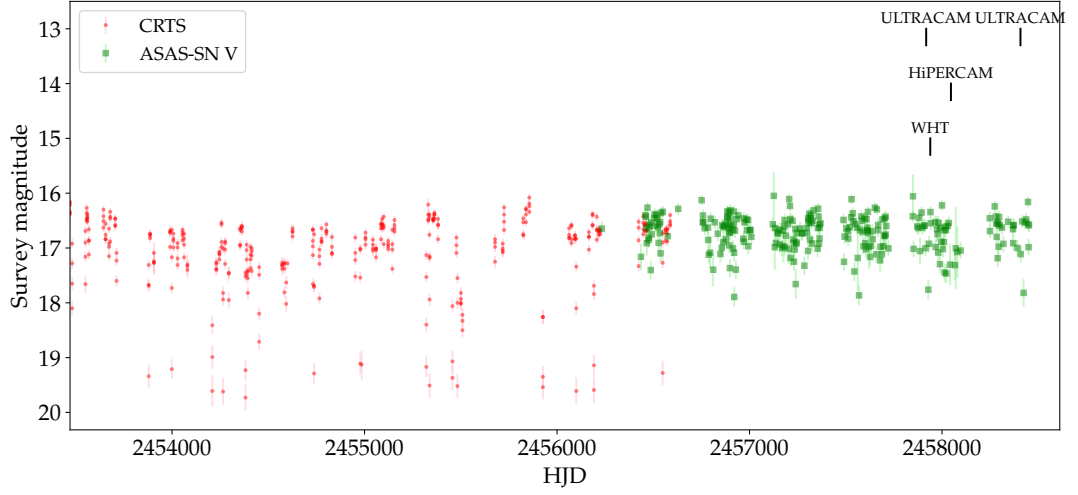
Figure 6.1: Long term light curve of the CRTS and ASAS-SN photometry for CRTS2152. The total time span is $\simeq 13.6$ yrs. Marked on the figure are the times of the high speed photometry shown in Fig. 6.3 and 6.4. The spectroscopy was taken at a time indicated by the WHT marker.
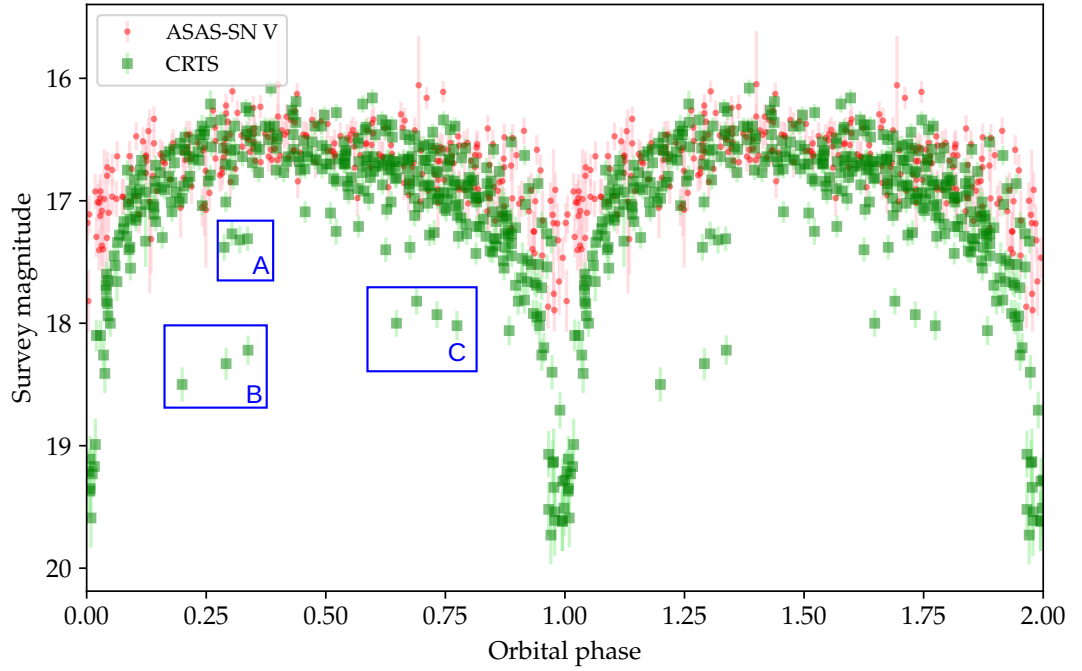
Figure 6.2: Phase folded CRTS and ASAS-SN photometry using the ephemeris in equation 6.3. Apart from the eclipse at phase 1.0, there is clear evidence of a least two distinct flux states, low and high. Each of the boxes A, B and C show a group of points that belong to the same orbital cycle as each other.

Table 6.1: Photometry used in this study.

Date	BJD	Filters	Camera	$T_{\exp}$ (s)	Total time (min)
2017/06/12	2457917	Sloan u, g, i	ULTRACAM	5.8	154
2017/10/19	2458046	Sloan g, r, i, z	HiPERCAM	2.5	66
2018/10/15	2458407	Sloan u, g, r	ULTRACAM	1.4	226

Table 6.2: Spectroscopy used in this study. N represents the number of spectra obtained on each night.

Date	BJD	Gratings	N	$T_{\exp}$ (s)	Total time (min)
2017/07/03	2457938	R1200B, R1200R	24	240, 300	105
2017/07/04	2457939	R1200B, R1200R	40	300	211
2017/08/12	2457978	R1200B, R1200R	40	300	226

6.2.4 Spectroscopy

In 2017 July and August we obtained spectra for CRTS2152 using the ISIS dual-beam spectrograph mounted on the WHT. The ISIS blue arm was fitted with the R1200B grating and set at a central wavelength of $4600\,\text{Å}$ with a resolution of $0.45\,\text{Å}\,\text{pixel}^{-1}$. The ISIS red arm was fitted with the R1200R grating set at a central wavelength of $8400\,\text{Å}$ and a resolution of $0.24\,\text{Å}\,\text{pixel}^{-1}$. Exposure times were usually $300\,\text{s}$ with the aim of resolving changes in spectral features as a function of orbital phase. In all cases pixels were binned by a factor of 2 in the spatial direction. The reduction of the ISIS spectra followed the same procedure as described in the previous two chapters.

6.2.5 X-ray fluxes

With the accretion-heated shock close to the surface of the white dwarf, it can be expected that CRTS2152 should be a source of X-rays, both soft, due to the thermal radiation from the accretion spot and hard X-rays from the bremsstrahlung radiation. However, the Swift X-Ray Telescope Point Source Catalogue (Evans et al., 2014) does not have a source at that location nor does the ROSAT All-Sky Survey Point Source Catalogue (Boller et al., 2016).
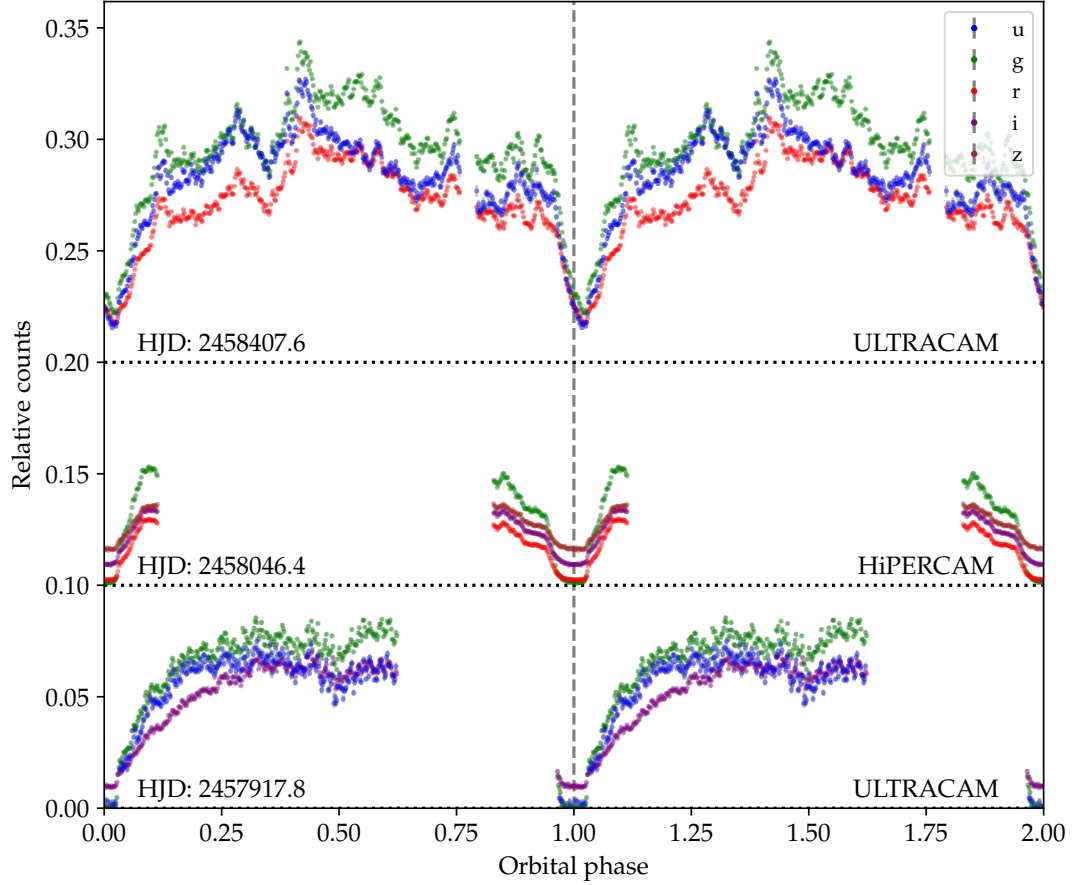
Figure 6.3: The ULTRACAM and HiPERCAM observations of CRTS2152 taken at the NTT and WHT respectively. The flux measured is that relative to our comparison star as described in the text. Data points have been phase-binned into a total of 500 bins per orbit. The two lower panels indicate the target is in a low(er) state with the u and g-band fluxes going down to zero once the accretion spot is in eclipse, however flux from the secondary in the i, r, and z band is still significant. The upper panel shows CRTS2152 in a high state, with the accretion stream still visible over the limb of the secondary. The data from each night has been vertically offset by 0.1.

6.3 Analysis

6.3.1 Photometric behaviour

Our photometric data is presented in Figs. 6.3 and 6.4. It is clear that these light-curves show the star in different states. The first two nights appear to be in a lower state than the final night. Although we don't have a full orbital cycle for the low state, we can deduce that the peak of the relative flux in the g-band is $\simeq 0.075$ which, by using the known g magnitude of the comparison star, places CRTS2152 at $g = 17.0$. At its lowest state in the CRTS data (at JD $\simeq 2455500$) CRTS2152 seems to have an average magnitude of $\simeq 18$. Noting, of course, that CRTS uses a broader passband than the Sloan g filter. The high state data were taken on the last night (JD 2457917) with CRTS2152 approximately 0.5 magnitude brighter with respect to the same comparison star than on the first night (JD 2458407). In this high state, the eclipse is not 'flat-bottomed', but rather V-like in shape. Also, flux in the u and g filters does not drop down to zero. Our interpretation of this behaviour is that the accretion stream is still visible and only partially eclipsed even at phase zero. Changes in eclipse profile similar to this have been noted in polars before, such as those seen in EP Dra (Bridge et al., 2003) and HU Aqr (Bours et al., 2014; Bridge et al., 2002) with the common explanation being that the altitude of the accretion stream above the orbital plane is altered when the accretion rate changes. Higher accretion rates lead to an accretion curtain with a higher co-latitude which is therefore visible over the limb of the donor during the ingress phase of the eclipse. For CRTS2152 it seems that this effect is even more pronounced than in either EP Dra or HU Aqr as the accretion stream is never fully eclipsed during the high state. In all light curves, there is a clear egress of the accretion spot at phase $\phi = 0.029$. The light curve taken on JD 2458046 gives us the clearest indication of the nature of the secondary as we see the colour during the primary eclipse shift to dominate in the z band while there is no detectable flux in the g band.

6.3.2 Ephemeris

The long time span photometric coverage taken from the CRTS and ASAS-SN surveys was used to determine the orbital period for the system. First, a periodogram was computed to give an initial estimate of the period and this was then followed up by a least squares fit of the form

$$V = c + a \cos\left[\frac{2\pi(t - T_0)}{P_{\mathrm{orb}}}\right], \tag{6.1}$$
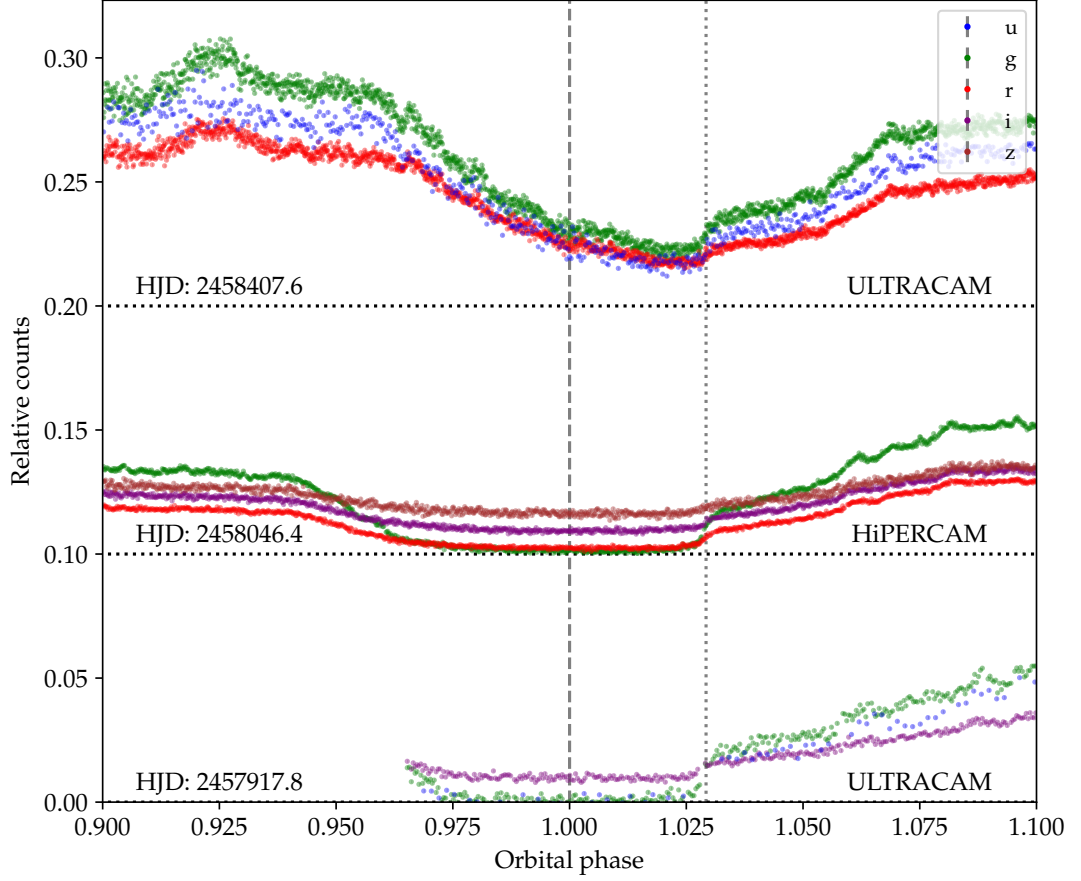
Figure 6.4: Similar to Fig. 6.3 and zooming in on the eclipse at phase 1.0. Unlike in the previous figure, the data has *not* been binned. The vertical line indicates phase zero as measured from the centre of the eclipse observed on the first night (lower panel). The time of minimum light in the upper panel, with CRTS2152 in a high state, does not coincide with phase zero, which is likely to be due to the geometry of the high-state accretion stream. It can be seen that the phase of the egress of the accretion spot ($\phi \simeq 1.029$, indicated by the dotted line) maintains its position in all panels. Each night has been offset by 0.1.

where V is the measured magnitude of the target in the survey, c and a are fitted constants and P_{orb} is the fitted period of our system. The value of T_0 was then offset by half a period to correspond with a minimum in the light-curve and hence the centre of the primary eclipse. Our computed ephemeris was then,

$$\mathrm{BJD(TDB)} = 2453469.891(3) + E \times 0.162975(2). \qquad (6.2)$$

Since the survey photometry does not have sufficently high cadence to resolve the ingress and egress of the eclipse, the uncertainty of our fit to T_0 can be refined by using high speed photometry. In the ULTRACAM and HiPERCAM observations, the first and second light curves (HJD 2457917 and 2458046) show the system in a low state and therefore the ingress and egress phases are clearly defined. By fitting a sigmoid function (as described in section 5.3.2) to both the ingress and egress and then using these measurements to calculate the mid-point of the eclipse, we can re-compute our ephemeris with T_0 defined as the epoch of mid-point of the primary eclipse to be,

$$\mathrm{BJD(TDB)} = 2457917.80117(5) + E \times 0.162975(2). \qquad (6.3)$$

The ingress and egress points are probably not specifically the ingress and egress of the white dwarf. It appears that the sharp feature in egress is caused by the emergence of the accretion spot.

By examinating the profile of the eclipses of the nights of HJD 2457917 and HD 2458046, we can deduce that the ingress appears to reach minimum for the g-band at a phase of approximately 0.97. The sharp egress of the accretion spot reappearing. If we assume that the white dwarf is emerging simultaneously, then a rough approximation of the duration of the white dwarf eclipse is $\Delta\phi \simeq 0.06$. Using the same approach to estimating the inclination of the system as used in section 4.3.6 and also assuming a q of 0.3 (see section 6.3.5), our estimate for the inclination of the system is 78°. It is likely that this is an under-estimate of $\Delta\phi$ and hence the inclination since we cannot be sure that we are truly seeing both the ingress and the egress of the white dwarf. More photometry of the eclipse in a low state is needed to establish the causes of the various features of the eclipse profile.

6.3.3   Average spectrum

We computed the overall average spectrum from the 104 spectra obtained with ISIS in the Heliocentric rest frame (Fig. 6.5). The blue arm spectrum is dominated by He II emission at 4686 Å and Balmer (Hβ and Hγ) emission at 4861 and 4340 Å
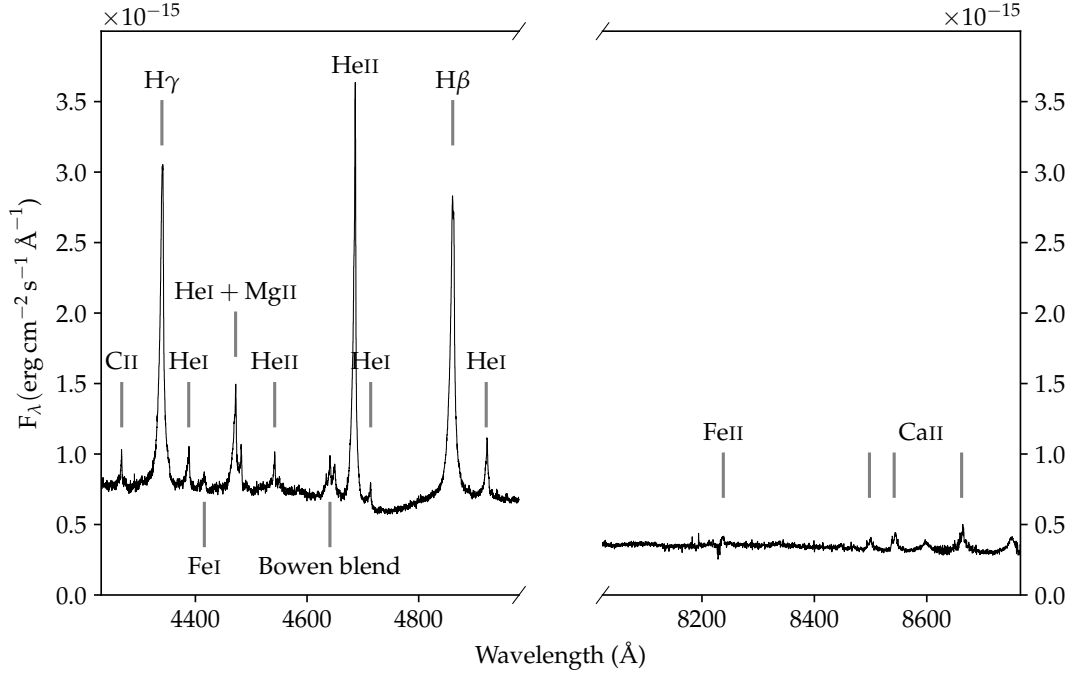
Figure 6.5: The average spectrum computed from the three nights of data listed in Table 6.2. All spectra were combined in the Heliocentric rest frame.

respectively. The Bowen blend, which consists of several emission lines (mainly N III, O II and C III) can be discerned just blue-ward of strong He II emission. The Bowen blend is a flourescent line series that is triggered by the excitation of O III by He II Lyα photons and the subsequent excitation of N III which decays through transitions at wavelengths of 4634, 4641 and 4642 Å. See Fig. 1 of Schachter et al. (1989) for a Grotrian diagram of the most important transitions that lead to the Bowen blend. Casares et al. (2006) show that, in low mass X-ray binary systems, where the strength of this feature is comparable to the helium emission, the origin of this radiation is localised to the irradiated surface of the secondary. In our case, the weakness of this feature and the low signal to noise of the lines meant that we were not able to measure radial velocities or compute tomograms with the available data.

6.3.4 Radial velocity of the secondary

In spectra taken away from the eclipse in the red arm of ISIS, the Ca II triplet at 8498, 8542 and 8662 Å is clearly present in emission. We attempted to measure the radial velocity of this triplet following a process similar to that described in section 3.3. Once again, the key parameter to be determined was the wavelength of the

feature with respect to the known laboratory wavelength. We fit a double Gaussian profile to the two blue-ward peaks of the triplet and, while keeping the separation constant at $44.07\,\text{Å}$ we allowed the height and wavelength of the fit to vary. Since this triplet is not discernable during some phases of the orbit it was only possible find a satisfactory fit for 54 of the total 104 spectra taken in the ISIS red arm. We then fit a sine wave to the radial velocities measured using the period determined from the photometric data. We find the semi-amplitude of the Ca II emission is $K_{\text{em}} = 129 \pm 3\,\text{km}\,\text{s}^{-1}$ and the systemic, or γ velocity is $-14 \pm 2\,\text{km}\,\text{s}^{-1}$ as is shown in Fig. 6.7. The calcium emission is expected to be emanating mainly from the illuminated face of the donor star and this is confirmed by our Doppler map of the Ca II line at $8542\,\text{Å}$ in Fig. 6.10.

Since the primary eclipse lasts for approximately $808\,\text{s}$ and our chosen exposure time was usually $300\,\text{s}$ it was possible to obtain spectra that were entirely exposed within the duration of the primary eclipse, with no contribution from the accretion spot or the white dwarf. However, since we were uncertain about the exact state (high or low) of the target at the time of the spectroscopic observations, we cannot be entirely sure that there was absolutely zero contribution from the accretion stream during these exposures, although examination of both the blue and the red arms show no obvious signs of emission. Unlike with V808 Aur (in chapter 5), an overall M-dwarf spectrum was not obvious from these data. This is not surprising given the increased distance of CRTS2152 over that of V808 Aur (216 versus 621 pc) and the choice of a higher resolution grating. A longer and more sensitive integration will be needed to identify the donor star. After averaging the eight spectra that were taken during eclipse, it was possible to detect the profile of the Na I doublet at $8190\,\text{Å}$ as is shown in Fig. 6.6. This bodes well for future observations as tracking this feature through the orbital period would allow a better estimation for the true radial velocity of the donor, as was achieved for V808 Aur.

6.3.5 Doppler maps

Using the maximum entropy techniques described in Marsh and Horne (1988); Marsh and Schwope (2016), we computed Doppler maps of several of the emission features in CRTS2152. The most prominent emission feature is that of He II at $4686\,\text{Å}$ (as seen in Fig. 6.5) and we show the corresponding Doppler map in Fig. 6.8. In order to plot the predicted Roche lobe velocities and the ballistic accretion stream we required an estimate for the mass ratio q of the system. For the mass of the donor, we used Table 3 in Knigge (2006) to derive a mass $M_2 = 0.25\,\text{M}_\odot$ for an accreting binary with a period of 3.91 h. For the mass of the primary, we assumed a mass of
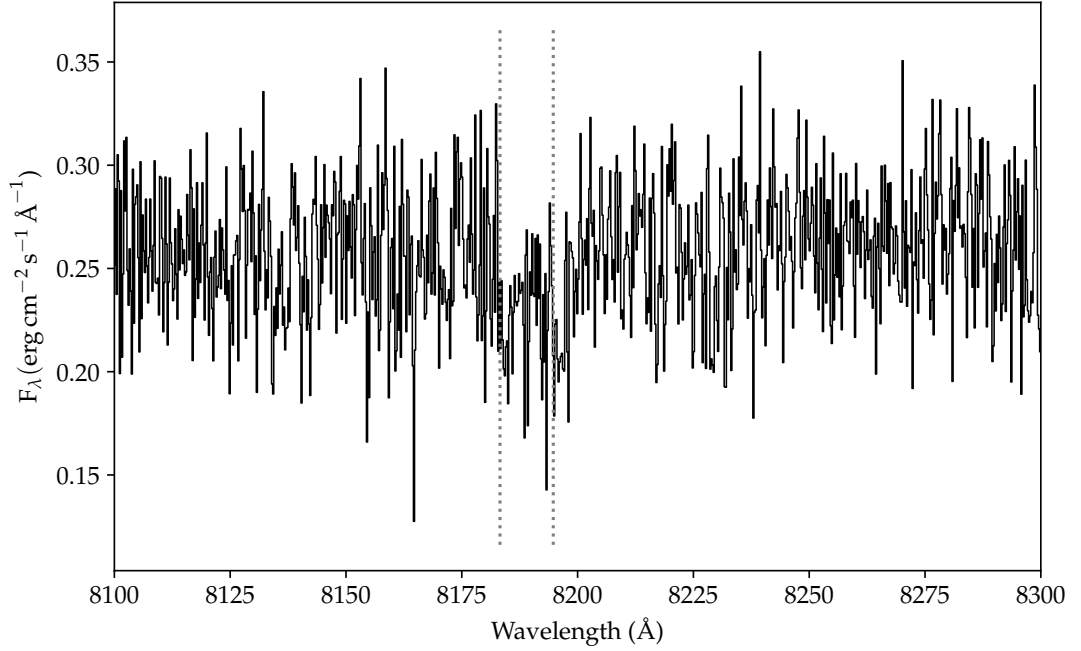
Figure 6.6: The average spectrum computed from those eight spectra that were taken during the primary eclipse. The position of the Na I absorption doublet is shown with vertical dotted lines.

$M_1 = 0.8 \, \mathrm{M_\odot}$. This is a rather speculative choice for primary mass and was chosen by comparison of the rendered accretion stream with that of predicted for various values of q on the Doppler map as seen in Fig. 6.9. The chosen value, is in line with the mode of the distribution of white dwarf masses in CVs derived from the SDSS survey presented by Zorotovic et al. (2011a).

6.4 Discussion

CRTS2152 shares several observational aspects with other known polars. Its period of 0.163 d places it firmly within the observed period distribution as shown in Fig. 1.8. Its method of discovery though is somewhat unusual. Whereas most polars where initially detected by virtue of of their X-ray luminosity with their nature being determined by followup optical studies and, now, more recently through wide area survey that note their transition between high and low states, CRTS2152 was noted for its low state light curve that mimics the double-hump shape usually seen in W UMa variables (Fig. 6.2). This suggests that, like V1460 Her in chapter 4, the elliptical modulation of the donor is an important factor in the shape of the light curve. This would suggest an early spectral type for the donor. Our spectra taken
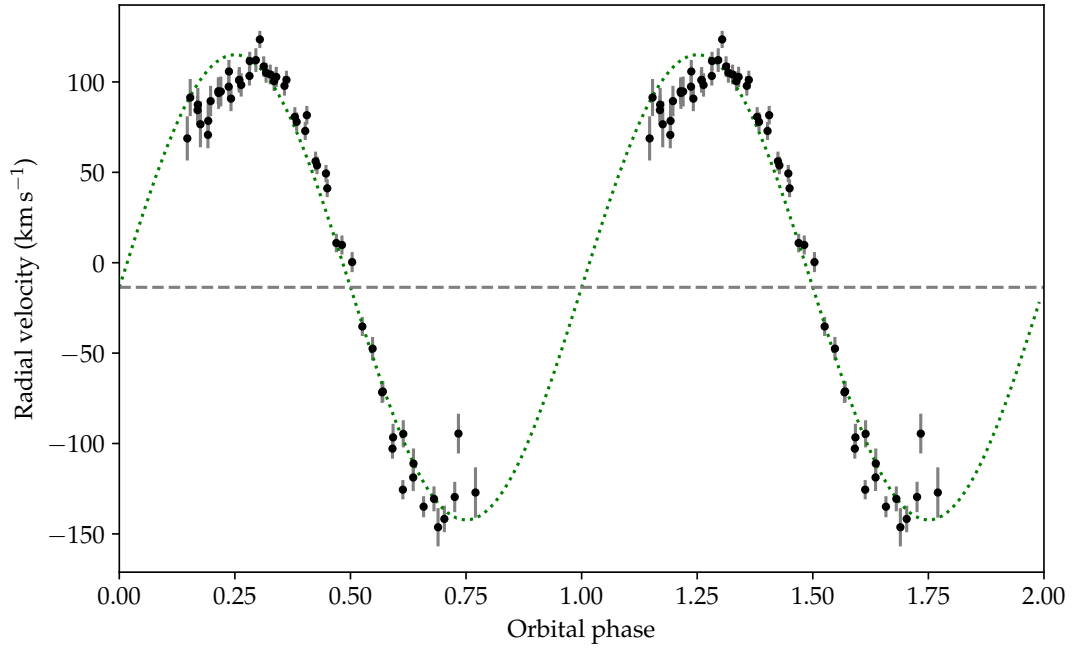
Figure 6.7: The projected radial velocity of the secondary as a function of orbital phase. The velocity was measured by fitting a double-Gaussian function to the two blue-ward emission peaks of the Ca II triplet at 8498, 8542 Å originating in chromospheric emission from the inward irradiated face of the donor. We find the semi-amplitude of this emission feature to be $K_{em} = 129 \pm 3 \, \text{km s}^{-1}$.
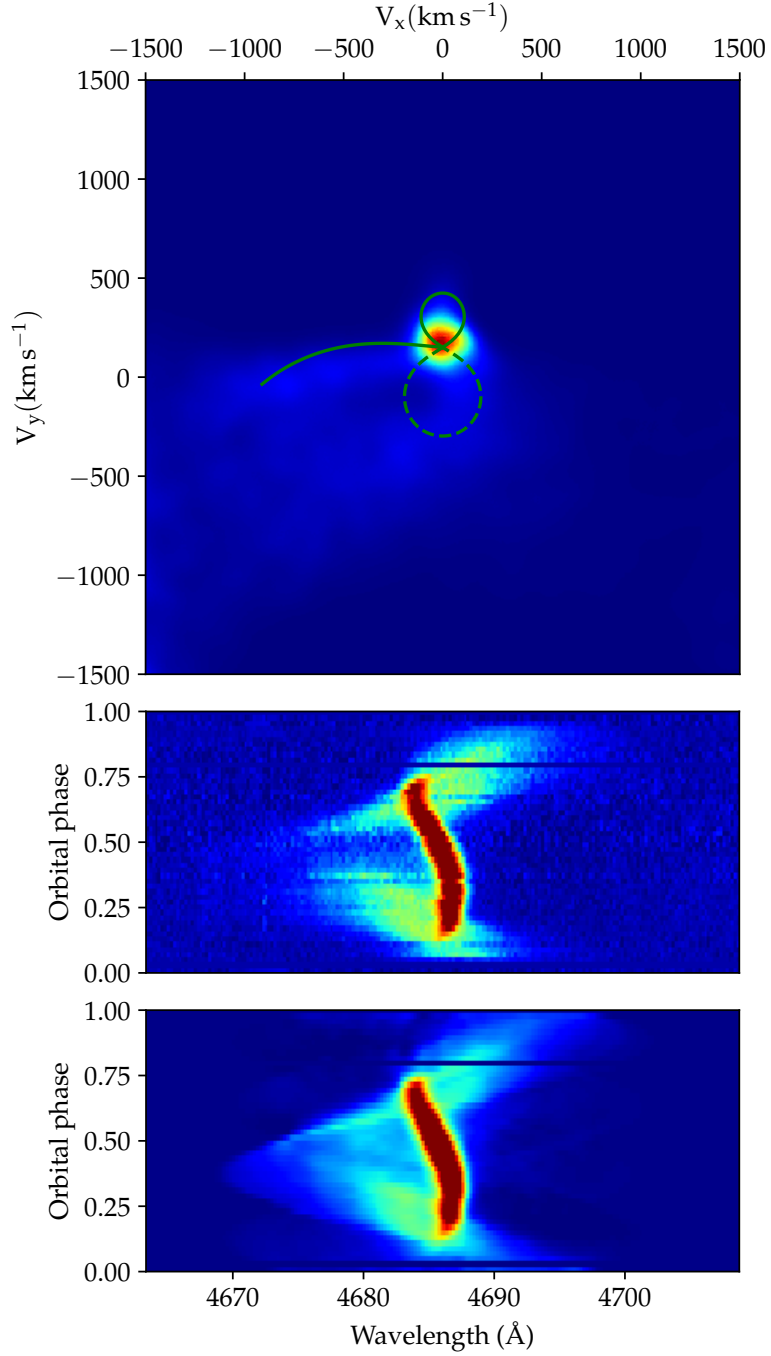
Figure 6.8: The Doppler map of the He II feature at 4686 Å. On the Doppler map the predicted velocity of the secondary Roche lobe is shown with solid line, the Roche lobe of the primary with a dashed line. Colour indices represent the relative intensity of the He II emission at the particular position in velocity space. We also show the predicted position of the ballistic accretion stream. Below the map we show the phase binned spectra. The upper of the two is the observed data and the lower is the modelled flux.
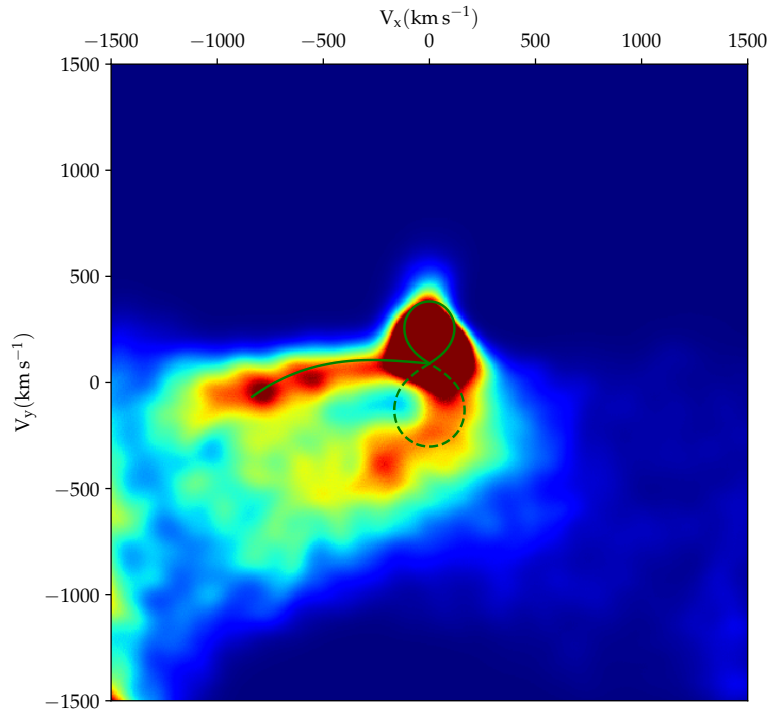
Figure 6.9: The same Doppler map as shown in Fig. 6.8 but with the colour look up table altered to increase the contrast and bring out more detail in the rendering of the accretion stream. It follows the ballistic trajectory calculated for a $q = 0.5$ mass ratio and then, after coupling on to the magnetic field lines accelerates to high velocities down to the accretion spot on the white dwarf.
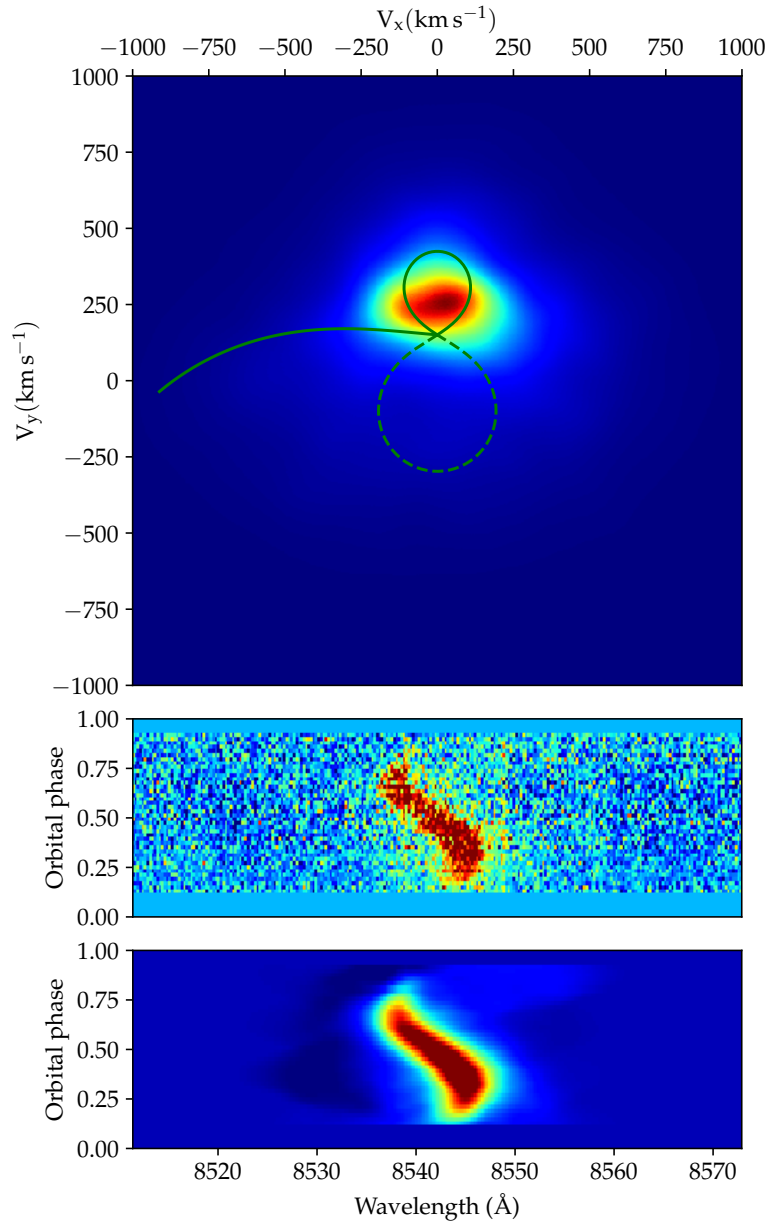
Figure 6.10: The Doppler map of the Ca II triplet line at 8542 Å.
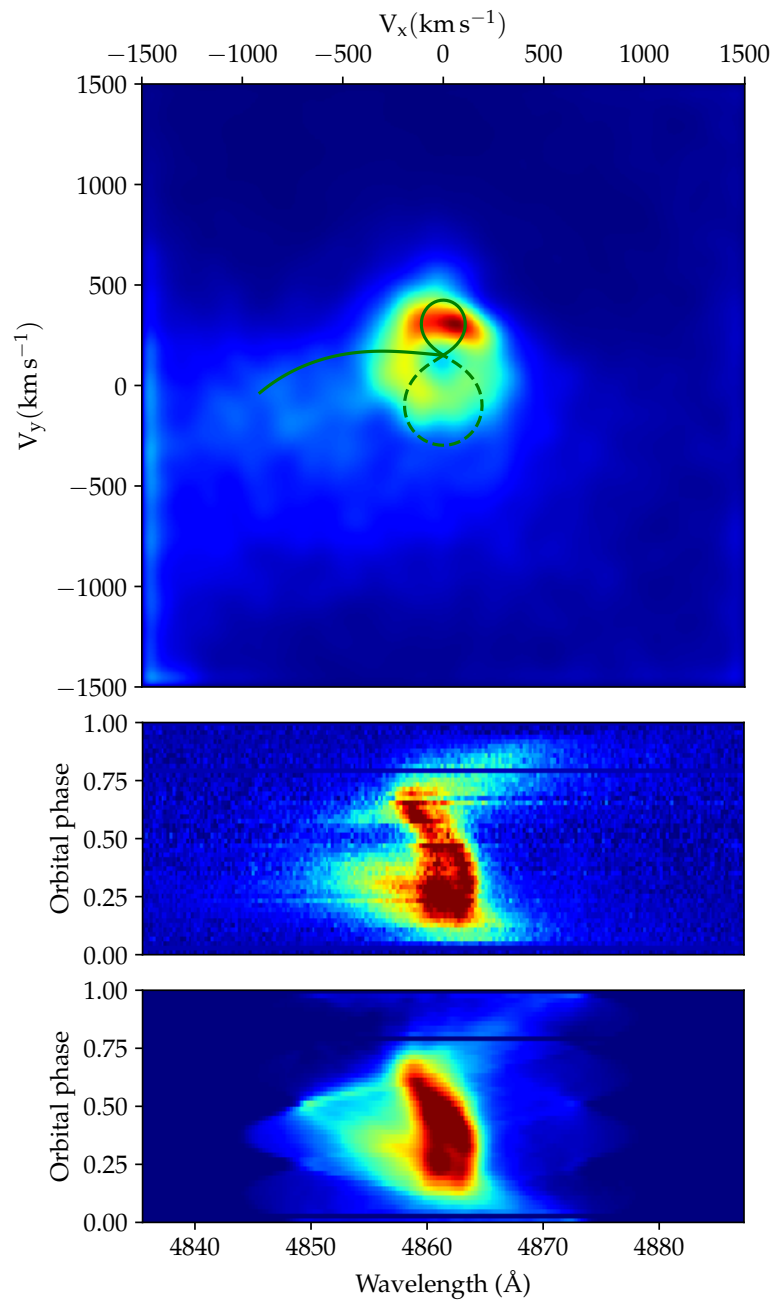
Figure 6.11: The Doppler map of the Hβ line at 4861 Å.
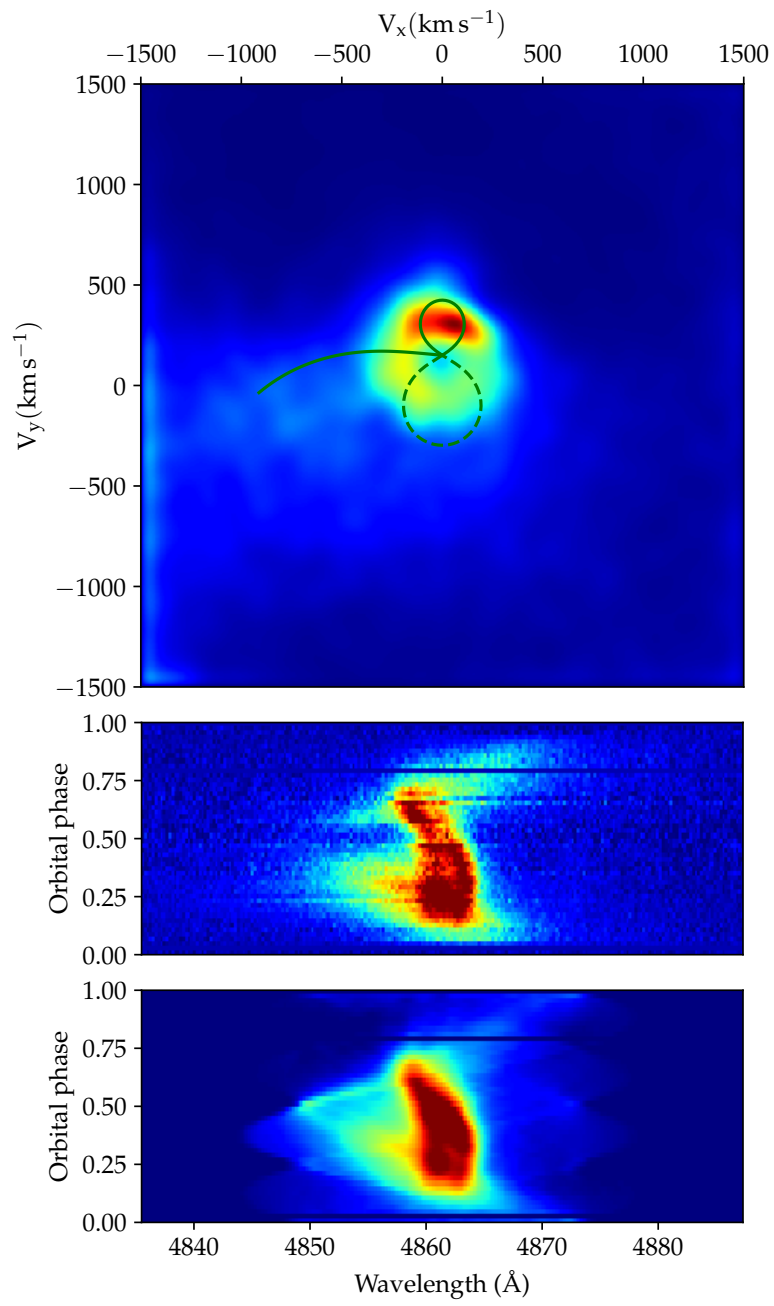
Figure 6.12: The Doppler map of the Hγ line at 4340 Å.

during the primary eclipse shows evidence of weak Na I absorption (Fig. 6.6), but no evidence of the TiO absorption bands seen in the M4-type donor of V808 Aur (5.13). Na I is visible, although weaker, in earlier spectral types and this hints that the donor in this case could be a K-type. Donors are rarely easily studied in polars as, very often, the optical flux is dominated by the accretion stream, so this target presents a unique opportunity to learn more about polar donors in general, but quite possibly, donors that have followed an unusual evolutionary path akin to that noted for V1460 Her in chapter 4.

Examination of the long baseline survey photometry of CRTS and Super-WASP do not give a clear indication of the time spent in high versus low states. Only few data points from CRTS highlighted as A, B, C in Fig. 6.1 appear to demonstrate the target in a low state which seems to suggest that these low states are rare. If this is indeed the case, then our ULTRACAM photometry on the first two occasions would have been extremely fortuitous to have both caught the system in a low state, separated as they are by almost 130 days. Further monitoring of the survey photometry and follow-up high speed photometry should enable us to determine the cadence of these states, which will shed light on the possible relationship between orbital period, donor spectral type and the various states of polars.

Examination of the Doppler maps for He II (Figs. 6.8, 6.9, 6.10, 6.11 and 6.12) show a clearly defined ballistic stream leaving the L_1 point and reaching a velocity of $\simeq 1000\,\mathrm{km\,s^{-1}}$ before coupling onto the field lines and becoming the magnetic stream. Ca II emission is confirmed to be produced on the irradiated face of the secondary. Comparison of the observed Doppler maps with theoretical models produced for HU Aqr compare favourably despite the fact that CRTS2152 has a period nearly twice as long. The V-shaped eclipse seen in the photometry during the high state suggests that the accretion stream geometry is strongly altered during high accretion rate episodes, if time resolved spectroscopy can be taken during high state and a new Doppler map computed, then a direct comparison of these two geometries could be traced and analysed.

6.5   Conclusion

We have presented the first spectroscopic and photometric observations of a new polar with an orbital period of 3.91 hr. By measuring the radial velocity of the irradiated inner face of the secondary, we can place a lower limit of the orbital velocity of the secondary to be $K_2 > 129 \pm 3\,\mathrm{km\,s^{-1}}$. Our estimates for the masses ($M_1 \simeq 0.8\,\mathrm{M_\odot}$, $M_2 \simeq 0.25\,\mathrm{M_\odot}$) and the inclination ($i \gtrsim 78\,^\circ$) are, at the moment,

early estimates and more photometric and spectroscopic data are required to refine these values. E

Chapter 7

Conclusion and future research paths

In this thesis I have presented analysis of the predicted results of the common envelope phase's role in creating compact binaries. I have also examined three systems that were formed via this evolutionary path that have gone on to initiate accretion.

7.1 PCEBs

I have shown that the evolution of one component in a binary system transforms an initial unimodal period distribution into a bimodal one. The common envelope brings the two components closer together and may cause the stars to merge. Those that survive become post common envelope binaries. If, however, the common envelope phase is avoided due to a wider separation of the initial pair, then the orbit widens further. This leads to a region in orbital period space that is devoid of any PCEBs. It is clear that instrument sensitivity and the number of candidates studied in this research mean that the conclusions are not beyond doubt and further investigation is required to increase confidence that no intermediate period PCEBs exist. As pointed out in chapter 3, increased wavelength resolution would allow the detection of the smaller radial velocities expected in systems with periods longer than $P_{\rm orb} \gtrsim 30$ days. This would require higher resolution gratings and larger aperture telescopes.

New multi-object spectroscopy projects like WEAVE[1] and DESI[2] might pro-

---

[1] https://ingconfluence.ing.iac.es:8444/confluence//display/WEAV/Science
[2] https://www.desi.lbl.gov/science/

vide data that aid detection and analysis of PCEBs but, at the moment, there is no specific programme proposed that would provide the right target list and cadence to enable a survey like this.

7.2 Early-type donor CVs

V1460 Her is a new member of a class of, currently rare, CVs where the donor is a relatively early-type star for its period. The donor in this class is over-sized for its mass and displays signs of having had some amount of CNO burning. It is likely that the donor had a much higher initial mass and the onset of accretion may have occurred in an unstable fashion with $M_2 > M_1$. This mass could have accreted onto the white dwarf increasing its spin rate possibly leading to steady state fusion on its surface. The fact that V1460 Her has a white dwarf with a spin of 39 s is an exciting prospect for follow-up observations. Only AE Aqr, at 33 s, is known to spin more rapidly. It has been shown that AE Aqr is in a state of rapid spin down with $\dot{P}_{\rm spin} = 5.64 \times 10^{-14}\,{\rm s\,s^{-1}}$ or a spin down time of 2×10^7 years (Wynn et al., 1997), and we can expect that the same might be happening with V1460 Her. The fact that AE Aqr is a propeller system that is flinging the accreting matter out of the binary altogether, and that V1460 Her clearly has an accretion disc, means that these two objects are by no means identical. High speed photometry, both in the optical and in the ultra-violet would enable us to measure, not only the potential change in the spin period, but also to determine the pulsation spectrum and confirm the origin of the signal as the photosphere of the white dwarf. Asymmetries in the modulation of the signal might give us clues to the nature of the magnetic field of the white dwarf and allow us to determine if we are seeing one or two poles as the object spins.

Another eclipsing CV, DQ Her shows a phase shift in the white dwarf spin oscillation as it passes through primary eclipse (Warner et al., 1972). Patterson et al. (1978) and Zhang et al. (1995) explain this with a model that has an opaque disc illuminated by the beamed radiation from the pole of the white dwarf. From the viewpoint of Earth, during the eclipse, we preferentially see the far-side of the disc. As this disc is partially eclipsed, the phase of oscillation increases and then jumps by 120° at mid-eclipse, eventually ending up with a full 360° shift in phase after egress. This might be an effect that is observable in V1460 Her. Although we had no clear detection of X-rays in our search through archival data catalogues, we would expect to see some hard X-ray flux from this object and this should be modulated with the spin period.

7.3 Polars

Our study of the two polars, V808 Aur and CRTS2152, have indicated that the transition from high to low (and, indeed, to intermediate) states is not a well studied area at present. Although there is at least one project underway to try to catalogue these transitions in a methodical way, this is still at an early stage. However, as we have shown in chapters 4, 5 and 6, there is a large (and growing) set of publicly available data that, when combined, covers timescales greater than ten years and includes many polars. One possible follow up study could be a project to combine a canonical list of known polars with archival data from the likes of SuperWASP, ASAS-SN, CRTS, AAVSO and ZTF. Another potential source of data are recent exoplanet hunting missions, such as *Kepler*, which have already provided serendipitous photometry for dwarf novae (Ramsay et al., 2012). Of course, we are still anticipating the commissioning of the Vera C. Rubin Observatory (aka LSST), but there is enough data already available to allow us the perform an analysis on the nature, cadence and frequency of high state to low state transitions in polars and to relate this with other observable parameters, such as orbital periods, component masses and magnetic field strengths.

Our Doppler maps of the stream flows in CRTS2152 reveal details about where the coupling of the magnetic field takes place. A comparison with similar maps produced for HU Aqr shows that while there are similarities, we can learn more from comparing the observed streams with those produced by models. With a steady rise in the number of known polars, more time resolved spectroscopy would be useful to delve deeper into this topic.

7.4 Open questions for current research

Since the post common envelope binaries in general, and CVs in particular, are progenitors of supernovae type Ia (SN Ia), understanding their evolution is vital to an overall understanding of the structure of the universe. These supernovae act as standard candles for the distance scale of the universe and it was observations of SN Ia that was the first indicator of the accelerating expansion of the universe (Perlmutter and Schmidt, 2003), leading to the conjecture of the existence of 'dark energy'. SN Ias' validity as standard candles is highly dependent on knowing the origins and constituent parts of the explosion. There are two models for the progenitors of SN Ia, namely the double-degenerate and the single degenerate models. In the double degenerate scenario two white dwarfs merge and, if their overall mass exceeds the

Chandrasekhar limit, the resulting explosion is a SN Ia. In the single degenerate model the accretion of material from a main sequence donor and the consequent accumulation of this material on the white dwarf slowly edges it towards the Chandrasekhar limit. This increased mass eventually causes the detonation of the SN Ia. It is this latter pathway that could be the ultimate fate of the objects covered in this thesis.

As we discussed in the chapter 1, most stars form in binaries, but the stars themselves are sufficiently separated such that they do not interact in any significant way. It is only through the evolution of one of the components into the giant phase and the potential common envelope that can bring them close enough together to interact. Understanding this phase is important to both the double degenerate and the single degenerate pathways to SN Ia. Single degenerate progenitors will have been through one common envelope phase, while the double degenerate progenitors through two of these phases. Chapter 3 demonstrated that one can successfully model the binary evolution of these pairs through BPS studies, and explain how the orbital period distribution is altered from a uni-modal to a bi-modal pattern by the common envelope and also demonstrated that this prediction is borne out through observations. However, there are still open questions regarding the exact period cut-off and therefore the subsequent evolution of these populations. Ultimately, since we do not have a well defined sample of the overall population it is hard to calculate the space density of these objects which, in turn, has implications on how many SN Ia we might expect to see from this evolutionary path, notwithstanding the fact that our own Galactic neighbourhood is a biased sample. Defining this number is important in aligning properties of the observed SN Ia with their progenitors and therefore their intrinsic brightness as standard candles. Improvements in the modelling of these systems, most notably the common envelope phase and the ejection of the envelope would help us to pin down how this stage effects the evolution. Our observational studies likely suffer from selection biases and further steps towards studying a completely unbiased sample of PCEBs will also help. We have already begun this task by launching a new survey of volume limited white dwarfs, selected from the *Gaia* survey within 40 parsecs of the Earth.

The single degenerate model requires that accreted material onto the white dwarf steadily accumulates up to $1.4 \, M_\odot$ triggering the supernova. CVs however, undergo runaway nuclear fusion of the accreted material on their surface, so called 'nova', that carry away this material. There is an open question regarding whether these nova events lead to an overall increase or decrease in mass of the white dwarf. Recent models of the nova eruptions that are driven by hydrogen ignition, see Darn-

ley (2019) and references therein, tend to agree that the overall trend of a nova explosion is to *increase* the mass of the white dwarf. However, the helium that is deposited on the white dwarf will eventually accumulate and undergo its own ignition, driving away the outer layers and a portion of mixed material, which results in a net *loss* of mass from the white dwarf. This is an ongoing area of research and more recent models (Hillman et al., 2016) are tentatively suggesting that it is possible to grow the white dwarf mass through combination of both hydrogen ignitions (or flashes) followed by helium flashes.

It appears that V1460 Her is a CV that has followed what was considered, until recently, an unusual evolutionary path. The early spectral-type of its donor and its bloated state, combined with the rapid spin of the white dwarf, all suggest that this system underwent a stage of rapid non-thermal timescale mass transfer and this might have been dynamically unstable, $M_2 > M_1$. This increased accretion rate would have lead to a steady nuclear burning on the surface of the white dwarf. In this scenario, material is not violently ejected and mass build-up is straight-forward. Nova eruptions are suppressed in this channel and this could mean an easier route to mass increase on the white dwarf. Finding more of these CVs and studying their evolutionary history (in particular to determine if they have a significantly higher M_1 than 'normal' CVs) and their subsequent pathway could potentially lead to a new progenitor scenario for SN Ia.

We noted significant period variations through the timing of the eclipses of V808 Aur. Studies of timing variations in polars suggest that most, if not all, polars exhibit significant deviations from a simple linear ephemeris. Both explanations usually offered for this effect, tertiary orbiting bodies (usually super-Jupiters) and the Applegate mechanism seem to be unsatisfactory. In all cited studies of these objects, the energy required by the Applegate mechanism is in excess of the total luminosity of the secondary star (Potter et al., 2011, for example). Planetary explanations seem somewhat contrived, but are, at the moment at least, the only appropriate explanations for the dramatic O-C timing variations seen in polars and measured here for V808 Aur. A comprehensive study of timing variations in polars, similar to that being undertaken in PCEBs (Parsons et al., 2010), is overdue and could be a fruitful area of exploration. With well defined eclipses and a relatively short orbital period, V808 Aur is an ideal target to gather more data on this topic.

Bibliography

Abbott B.P. et al., 2016. *Physics Review Letters*, 116(24):241103.

Alam S. et al., 2015. *Astrophysical Journal, Supplement*, 219:12.

Angelini L. and Verbunt F., 1989. *Monthly Notices of the Royal Astronomical Society*, 238:697–708.

Applegate J.H., 1992. *Astrophysical Journal*, 385:621.

Araujo-Betancor S. et al., 2005. *Astrophysical Journal*, 622(1):589–601.

Arnould M., Goriely S., and Jorissen A., 1999. *Astronomy and Astrophysics*, 347:572–582.

Ashley R.P., 2015. *Automated reduction of the ULTRACAM data archive*. Master's thesis, University of Warwick.

Ashley R.P. et al., 2019. *Monthly Notices of the Royal Astronomical Society*, 484(4):5362–5376.

Bate M.R., Bonnell I.A., and Bromm V., 2003. *Monthly Notices of the Royal Astronomical Society*, 339(3):577–599.

Belczynski K. et al., 2006. *Astrophysical Journal*, 648:1110–1116.

Belloni D. and Schreiber M.R., 2020. *Monthly Notices of the Royal Astronomical Society*, 492(1):1523–1529.

Belloni D. et al., 2020. *Monthly Notices of the Royal Astronomical Society*, 491(4):5717–5731.

Berger L. et al., 2005. *Astronomy and Astrophysics*, 444(2):565–571.

Beuermann K., Dreizler S., and Hessman F.V., 2013. *Astronomy and Astrophysics*, 555:A133.

Bochanski J.J. et al., 2007. *Astronomical Journal*, 133:531–544.

Boller T. et al., 2016. *Astronomy and Astrophysics*, 588:A103.

Bonnell I.A. and Bate M.R., 1994. *Monthly Notices of the Royal Astronomical Society*, 271:999–1004.

Bonnet-Bidaud J.M. and Mouchet M., 1987. *Astronomy and Astrophysics*, 188:89–94.

Bonnet-Bidaud J.M. et al., 2019. *arXiv e-prints*, arXiv:1906.06985.

Bours M., 2015. *Detailed studies of white dwarf binaries and their orbital periods*. Ph.D. thesis, University of Warwick.

Bours M.C.P. et al., 2014. *Monthly Notices of the Royal Astronomical Society*, 445(2):1924–1931.

Bridge C.M. et al., 2002. *Monthly Notices of the Royal Astronomical Society*, 336(4):1129–1138.

Bridge C.M. et al., 2003. *Monthly Notices of the Royal Astronomical Society*, 341(3):863–869.

Brinkworth C.S. et al., 2013. *Astrophysical Journal*, 773(1):47.

Butters O.W. et al., 2010. *Astronomy and Astrophysics*, 520:L10.

Camacho J. et al., 2014. *Astronomy and Astrophysics*, 566:A86.

Cannizzo J.K., Ghosh P., and Wheeler J.C., 1982. *Astrophysical Journal Letters*, 260:L83–L86.

Capitanio L. et al., 2017. *Astronomy and Astrophysics*, 606:A65.

Casares J. et al., 2006. *Monthly Notices of the Royal Astronomical Society*, 373(3):1235–1244.

Chanan G.A., Middleditch J., and Nelson J.E., 1976. *Astrophysical Journal*, 208:512–517.

Chandrasekhar S., 1939. *An introduction to the study of stellar structure*. Dover.

Chote P. et al., 2014. *Monthly Notices of the Royal Astronomical Society*, 440(2):1490–1497.

Cropper M., 1990. *Space Science Reviews*, 54(3-4):195–295.

Cropper M. et al., 1989. *Monthly Notices of the Royal Astronomical Society*, 236:29P–38.

Cumming A., 2002. *Monthly Notices of the Royal Astronomical Society*, 333(3):589–602.

Cumming A., Marcy G.W., and Butler R.P., 1999. *Astrophysical Journal*, 526:890–915.

Darnley M.J., 2019. *arXiv e-prints*, arXiv:1912.13209.

Davis P.J., Kolb U., and Willems B., 2010. *Monthly Notices of the Royal Astronomical Society*, 403:179–195.

Dhillon V. et al., 2018. In *Proceedings of the Society of Photo-Optical Instrumentation Engineers*, volume 10702 of *Society of Photo-Optical Instrumentation Engineers (SPIE) Conference Series*, 107020L.

Dhillon V.S. et al., 2007. *Monthly Notices of the Royal Astronomical Society*, 378(3):825–840.

Dhillon V.S. et al., 2014. *Monthly Notices of the Royal Astronomical Society*, 444:3504.

Dhillon V.S. et al., 2016. *Proceedings of the SPIE*, 9908:99080Y.

Di Stefano R., 2010. *Astrophysical Journal*, 712(1):728–733.

Drake A.J., 2016. *The Astronomer's Telegram*, 9112:1.

Drake A.J. et al., 2014a. *Monthly Notices of the Royal Astronomical Society*, 441(2):1186–1200.

Drake A.J. et al., 2014b. *Astrophysical Journal, Supplement*, 213:9.

Dufour P. et al., 2017. In P.E. Tremblay, B. Gaensicke, and T. Marsh, editors, *20th European White Dwarf Workshop*, volume 509 of *Astronomical Society of the Pacific Conference Series*, 3.

Duquennoy A. and Mayor M., 1991. *Astronomy and Astrophysics*, 500:337–376.

Eggleton P.P., 1983. *Astrophysical Journal*, 268:368–369.

Eggleton P.P. and Tokovinin A.A., 2008. *Monthly Notices of the Royal Astronomical Society*, 389:869–879.

Einstein A., 1916. *Sitzungsberichte der Königlich Preußischen Akademie der Wissenschaften (Berlin*, 688–696.

Eracleous M. et al., 1994. *Astrophysical Journal*, 433:313.

Evans P.A. et al., 2014. *Astrophysical Journal, Supplement*, 210:8.

Farihi J., Hoard D.W., and Wachter S., 2006. *Astrophysical Journal*, 646:480–492.

Farihi J., Hoard D.W., and Wachter S., 2010. *Astrophysical Journal, Supplement*, 190:275–296.

Faulkner J., 1971. *Astrophysical Journal Letters*, 170:L99.

Faulkner J., Flannery B.P., and Warner B., 1972. *Astrophysical Journal Letters*, 175:L79.

Ferrario L., de Martino D., and Gänsicke B.T., 2015. *Space Science Reviews*, 191(1-4):111–169.

Ferrario L. and Wickramasinghe D.T., 2010. In K. Werner and T. Rauch, editors, *American Institute of Physics Conference Series*, volume 1273 of *American Institute of Physics Conference Series*, 378–383.

Filippenko A.V., 1982. *Publications of the Astronomical Society of the Pacific*, 94:715–721.

Fontaine G., Brassard P., and Bergeron P., 2001. *Publications of the Astronomical Society of the Pacific*, 113(782):409–435.

Fujimoto M.Y., 1982. *Astrophysical Journal*, 257:767.

Gaia Collaboration et al., 2018. *ArXiv e-prints*.

Gänsicke B.T. et al., 2003. *Astrophysical Journal*, 594(1):443–448.

Gänsicke B.T. et al., 2009. *Monthly Notices of the Royal Astronomical Society*, 397(4):2170–2188.

Goodricke J., 1783. *Philosophical Transactions of the Royal Society of London Series I*, 73:474–482.

Green J.C. et al., 2012. *Astrophysical Journal*, 744(1):60.

Green M.J., 2019. *The Evolution of AM CVn Binary Systems*. Ph.D. thesis, University of Warwick.

Greenstein J.L. and Kraft R.P., 1959. *Astrophysical Journal*, 130:99.

Hameury J.M. and Lasota J.P., 2017. *Astronomy and Astrophysics*, 602:A102.

Han Z. and Podsiadlowski P., 2004. *Monthly Notices of the Royal Astronomical Society*, 350:1301–1309.

Hardy L.K. et al., 2017. *Monthly Notices of the Royal Astronomical Society*, 465(4):4968–4984.

Harrison T.E., 2016. *Astrophysical Journal*, 833(1):14.

Harrop-Allin M.K., Potter S.B., and Cropper M., 2001. *Monthly Notices of the Royal Astronomical Society*, 326(2):788–798.

Henden A.A. et al., 2015. In *American Astronomical Society Meeting Abstracts #225*, volume 225 of *American Astronomical Society Meeting Abstracts*, 336.16.

Hermes J.J. et al., 2017. *Astrophysical Journal, Supplement*, 232(2):23.

Hillman Y. et al., 2016. *Astrophysical Journal*, 819(2):168.

Hind J.R., 1856. *Monthly Notices of the Royal Astronomical Society*, 16:56–56.

Horne K., 1986. *Publications of the Astronomical Society of the Pacific*, 98:609–617.

Horne K. et al., 1994. *Astrophysical Journal*, 426:294.

Horner J. et al., 2012. *Monthly Notices of the Royal Astronomical Society*, 425(1):749–756.

Iben I. J., 1982. *Astrophysical Journal*, 259:244–266.

Ivanova N. et al., 2013. *Astronomy and Astrophysics Review*, 21:59.

Jameson R.F., King A.R., and Sherrington M.R., 1980. *Monthly Notices of the Royal Astronomical Society*, 191:559–569.

Jeans J.H., 1902. *Philosophical Transactions of the Royal Society of London Series A*, 199:1–53.

Jetsu L. et al., 2013. *Astrophysical Journal*, 773(1):1.

Kawka A. et al., 2007. *Astrophysical Journal*, 654(1):499–520.

Kazarovets E.V. et al., 2019. *Information Bulletin on Variable Stars*, 6261:1.

Kennedy M. et al., 2015. *Astrophysical Journal*, 815(2):131.

Kepler S.O. et al., 2007. *Monthly Notices of the Royal Astronomical Society*, 375(4):1315–1324.

Kjurkchieva D.P. et al., 2017. *New Astronomy*, 52:8–13.

Kleinman S.J. et al., 2013. *Astrophysical Journal, Supplement*, 204(1):5.

Knigge C., 2006. *Monthly Notices of the Royal Astronomical Society*, 373(2):484–502.

Knigge C., Baraffe I., and Patterson J., 2011. *Astrophysical Journal, Supplement*, 194:28.

Kochanek C.S. et al., 2017. *Publications of the Astronomical Society of the Pacific*, 129(980):104502.

Kolbin A.I. et al., 2019. *Astrophysical Bulletin*, 74(1):80–92.

Kraft R.P., 1962. *Astrophysical Journal*, 135:408.

Kraft R.P., Mathews J., and Greenstein J.L., 1962. *Astrophysical Journal*, 136:312–315.

Lambert D.L. and Slovak M.H., 1981. *Publications of the Astronomical Society of the Pacific*, 93:477–480.

Landsman W., 1993. *Publications of the Astronomical Society of the Pacific*, 105:841–847.

Lanza A.F., 2006. *Monthly Notices of the Royal Astronomical Society*, 369(4):1773–1779.

Law N.M. et al., 2009. *Publications of the Astronomical Society of the Pacific*, 121:1395.

Liebert J., 1988. *Publications of the Astronomical Society of the Pacific*, 100:1302.

Liebert J., Bergeron P., and Holberg J.B., 2005. *Astrophysical Journal, Supplement*, 156:47–68.

Liebert J. et al., 1994. *Astrophysical Journal*, 421:733–737.

Linnell A.P., 1949. *Sky and Telescope*, 8:166.

Linnell A.P., 1950. *Harvard College Observatory Circular*, 455:1–13.

Littlefair S.P. et al., 2001. *Monthly Notices of the Royal Astronomical Society*, 327(2):475–482.

Livio M. and Pringle J.E., 1998. *Astrophysical Journal*, 505(1):339–343.

Lohr M.E. et al., 2013. *Astronomy and Astrophysics*, 549:A86.

Lomb N.R., 1976. *Astrophysics and Space Science*, 39:447–462.

Maehara H., 2016. *The Astronomer's Telegram*, 9113:1.

Marsh T.R., 1989a. *Publications of the Astronomical Society of the Pacific*, 101:1032.

Marsh T.R., 1989b. *Publications of the Astronomical Society of the Pacific*, 101:1032–1037.

Marsh T.R., 1990. *Astrophysical Journal*, 357:621–629.

Marsh T.R., Dhillon V.S., and Duck S.R., 1995a. *Monthly Notices of the Royal Astronomical Society*, 275:828.

Marsh T.R. and Horne K., 1988. *Monthly Notices of the Royal Astronomical Society*, 235:269–286.

Marsh T.R. and Schwope A.D., 2016. *Doppler Tomography*, volume 439 of *Astrophysics and Space Science Library*, 195. Springer.

Marsh T.R. et al., 1995b. *Monthly Notices of the Royal Astronomical Society*, 274(2):452–460.

Marsh T.R. et al., 2014. *Monthly Notices of the Royal Astronomical Society*, 437(1):475–488.

Marsh T.R. et al., 2016. *Nature*, 537(7620):374–377.

Maxted P.F.L. et al., 2006. *Nature*, 442(7102):543–545.

Maxted P.F.L. et al., 2008. *Monthly Notices of the Royal Astronomical Society*, 385:2210–2224.

McCook G.P. and Sion E.M., 1999. *Astrophysical Journal, Supplement*, 121:1–130.

Meyer F. and Meyer-Hofmeister E., 1981. *Astronomy and Astrophysics*, 104:L10–L12.

Moffat A.F.J., 1969. *Astronomy and Astrophysics*, 3:455.

Morales-Rueda L. et al., 2003. *Monthly Notices of the Royal Astronomical Society*, 338:752–764.

Mouchet M. et al., 1991. *Astronomy and Astrophysics*, 250:99.

Nebot Gómez-Morán A. et al., 2011. *Astronomy and Astrophysics*, 536:A43.

Oswalt T.D. and Barstow M.A., 2013. *Planets, Stars and Stellar Systems Vol. 4.* Springer.

Paczyński B., 1971. *Annual Review of Astronomy and Astrophysics*, 9:183.

Paczynski B. and Sienkiewicz R., 1981. *Astrophysical Journal Letters*, 248:L27–L30.

Pala A.F. et al., 2019. *Monthly Notices of the Royal Astronomical Society*, 483(1):1080–1103.

Parsons S.G. et al., 2010. *Monthly Notices of the Royal Astronomical Society*, 407(4):2362–2382.

Parsons S.G. et al., 2017. *Monthly Notices of the Royal Astronomical Society*, 471(1):976–986.

Patterson J., Robinson E.L., and Nather R.E., 1978. *Astrophysical Journal*, 224:570–583.

Perlmutter S. and Schmidt B.P., 2003. *Measuring Cosmology with Supernovae*, volume 598, 195–217.

Podsiadlowski P., Han Z., and Rappaport S., 2003. *Monthly Notices of the Royal Astronomical Society*, 340(4):1214–1228.

Pollacco D.L. et al., 2006. *Publications of the Astronomical Society of the Pacific*, 118(848):1407–1418.

Potter S.B. et al., 2011. *Monthly Notices of the Royal Astronomical Society*, 416(3):2202–2211.

Poyner G., 2013. *Journal of the British Astronomical Association*, 123:108–114.

Raghavan D. et al., 2010. *Astrophysical Journal, Supplement*, 190(1):1–42.

Ramsay G. et al., 2012. *Monthly Notices of the Royal Astronomical Society*, 425(2):1479–1485.

Rappaport S., Verbunt F., and Joss P.C., 1983. *Astrophysical Journal*, 275:713–731.

Rebassa-Mansergas A. et al., 2012. *Monthly Notices of the Royal Astronomical Society*, 423:320–327.

Rebolo R., Zapatero Osorio M.R., and Martín E.L., 1995. *Nature*, 377(6545):129–131.

Richichi A. et al., 2016. *Astronomical Journal*, 151(1):10.

Ritter H. and Kolb U., 2003. *Astronomy and Astrophysics*, 404:301–303.

Rodríguez-Gil P. et al., 2009. *Astronomy and Astrophysics*, 496(3):805–812.

Salpeter E.E., 1955. *Astrophysical Journal*, 121:161.

Sanad M.R., 2011. *New Astronomy*, 16(1):19–26.

Scargle J.D., 1982. *Astrophysical Journal*, 263:835–853.

Schachter J., Filippenko A.V., and Kahn S.M., 1989. *Astrophysical Journal*, 340:1049.

Schenker K. et al., 2002. *Monthly Notices of the Royal Astronomical Society*, 337(3):1105–1112.

Schmidt G.D. and Stockman H.S., 2001. *Astrophysical Journal*, 548(1):410–424.

Schneider D.P. and Young P., 1980. *Astrophysical Journal*, 238:946–954.

Scholz F.W. and Stephens M.A., 1987. *Journal of the American Statistical Association*, 82(399):918–924.

Schreiber M.R. et al., 2008. *Astronomy and Astrophysics*, 484:441–450.

Schreiber M.R. et al., 2010. *Astronomy and Astrophysics*, 513:L7.

Schultz G., Zuckerman B., and Becklin E.E., 1996. *Astrophysical Journal*, 460:402.

Schwarz R. et al., 2009. *Astronomy and Astrophysics*, 496(3):833–840.

Schwope A.D. and Thinius B.D., 2018. *Astronomische Nachrichten*, 339(540):540–544.

Schwope A.D. et al., 2015. *Astronomische Nachrichten*, 336:115.

Shappee B.J. et al., 2014. *Astrophysical Journal*, 788(1):48.

Sion E.M., 2002. In M. Hernanz and J. José, editors, *Classical Nova Explosions*, volume 637 of *American Institute of Physics Conference Series*, 21–27.

Smak J., 1971. *Acta Astronomica*, 21:15.

Soubiran C. et al., 2013. *Astronomy and Astrophysics*, 552:A64.

Stephens M.A., 1974. *Journal of the American Statistical Association*, 69(347):730–737. ISSN 01621459.

Stephenson F.R. and Clark D.H., 1976. *Scientific American*, 234:100–107.

Stiller R.A. et al., 2018. *Astronomical Journal*, 156(4):150.

Stover R.J., 1981. *Astrophysical Journal*, 249:673–679.

Szkody P. and Silber A., 1996. *Astronomical Journal*, 112:289.

Thorne K., Garnavich P., and Mohrig K., 2010. *Information Bulletin on Variable Stars*, 5923:1.

Thorstensen J., 2016. *The Astronomer's Telegram*, 9141:1.

Thorstensen J.R., 2015. *Publications of the Astronomical Society of the Pacific*, 127(950):351.

Thorstensen J.R. et al., 2002a. *Astrophysical Journal Letters*, 567(1):L49–L52.

Thorstensen J.R. et al., 2002b. *Publications of the Astronomical Society of the Pacific*, 114(800):1117–1123.

Thorstensen J.R. et al., 2015. *Astronomical Journal*, 149(4):128.

Tout C.A. et al., 2008. *Monthly Notices of the Royal Astronomical Society*, 387(2):897–901.

Tremblay P.E. and Bergeron P., 2007. *Astrophysical Journal*, 657:1013–1025.

Tremblay P.E. et al., 2016. *Monthly Notices of the Royal Astronomical Society*, 461(2):2100–2114.

van den Heuvel E.P.J. et al., 1992. *Astronomy and Astrophysics*, 262:97–105.

Wachter S. et al., 2003. *Astrophysical Journal*, 586:1356–1363.

Wade R.A. and Horne K., 1988a. *Astrophysical Journal*, 324:411.

Wade R.A. and Horne K., 1988b. *Astrophysical Journal*, 324:411–430.

Walker M.F. and Herbig G.H., 1954. *Astrophysical Journal*, 120:278.

Warner B., 1986. *Monthly Notes of the Astronomical Society of South Africa*, 45:117.

Warner B., 1995. *Cambridge Astrophysics Series*, 28.

Warner B. and Nather R.E., 1971. *Monthly Notices of the Royal Astronomical Society*, 152:219.

Warner B. et al., 1972. *Monthly Notices of the Royal Astronomical Society*, 159:321.

Willems B. and Kolb U., 2004. *Astronomy and Astrophysics*, 419:1057–1076.

Winter L.M. and Sion E.M., 2001. In *American Astronomical Society Meeting Abstracts*, volume 199 of *American Astronomical Society Meeting Abstracts*, 62.01.

Wolf W.M. et al., 2013. *Astrophysical Journal*, 777(2):136.

Worpel H. and Schwope A.D., 2015. *Astronomy and Astrophysics*, 583:A130.

Wynn G.A., King A.R., and Horne K., 1997. *Monthly Notices of the Royal Astronomical Society*, 286(2):436–446.

Yu Z. et al., 2019. *Monthly Notices of the Royal Astronomical Society*, 489(1):1023–1036.

Zhang E. et al., 1995. *Astrophysical Journal*, 454:447.

Zola S. et al., 2017. *Astronomical Journal*, 154(6):276.

Zorotovic M., Schreiber M.R., and Gänsicke B.T., 2011a. *Astronomy and Astrophysics*, 536:A42.

Zorotovic M. et al., 2010. *Astronomy and Astrophysics*, 520:A86.

Zorotovic M. et al., 2011b. *Astronomy and Astrophysics*, 536:L3.

Zorotovic M. et al., 2014. *Astronomy and Astrophysics*, 568:A68.

Zuckerman B. et al., 2003. *Astrophysical Journal*, 596:477–495.